Forces in Cellular Growth and Division

Dissertation
for the award of the degree
"Doctor rerum naturalium"
of the Georg-August-Universität Göttingen

within the doctoral program
International Max Planck Research School
"Physics of Biological and Complex Systems"
(IMPRS PBCS)
in the Göttingen Graduate School for Neurosciences,
Biophysics and Molecular Biosciences
(GGNB)
of the Georg-August University School of Science
(GAUSS)

submitted by

Jörn Hartung

from Braunschweig (Germany)

Göttingen, 2015

Thesis Committee:

Prof. Dr. Oskar Hallatschek
Department of Physics
University of California, Berkeley

Prof. Dr. Jörg Enderlein
Third Institute of Physics - Biophysics / Complex Systems
Georg August University Göttingen

Prof. Dr. Stephan Herminghaus
Dynamics of Complex Fluids,
Max-Planck Institute for Dynamics and Self-Organization

Members of the Examination Board:

Referee: Prof. Dr. Stephan Herminghaus
Dynamics of Complex Fluids,
Max-Planck Institute for Dynamics and Self-Organization

2nd referee: Prof. Dr. Reiner Kree
Institute for Theoretical Physics,
Georg August University Göttingen

Further Members of the Examination Board:

Prof. Dr. Jörg Enderlein
Third Institute of Physics - Biophysics / Complex Systems
Georg-August-Universität Göttingen

Prof. Dr. Andreas Janshoff
Institute for Physical Chemistry
Georg August University Göttingen

Prof. Dr. Christoph Schmidt
Third Institute of Physics - Oscillation Physics
Georg August University Göttingen

Prof. Dr. Oskar Hallatschek
Department of Physics
University of California, Berkeley

Date of Oral Examination:
December 10th, 2015

I confirm that I have written this thesis independently and with no other sources and aids than quoted.

Göttingen, 2015

Contents

Chapter 1

Introduction

Mechanical forces are omnipresent when cells grow and divide as part of a population. A cell surrounded by other microorganisms has to push away neighbors during cellular growth in order to create space for new cell material.

During tissue development mechanical forces play an integral part, for instance in embryogenesis, scar tissue formation and bone growth [1]. Tissue cells are embedded in the extracellular matrix, which is a substrate on which cells can adhere and differentiate. Additionally, the extracellular matrix is a scaffold for tissues providing mechanical support [2]. Tissue cells can remodel this stress bearing scaffold as a response to changes in mechanical load by adjusting their protein synthesis levels to alter the composition of the extracellular matrix [3].

Mechanical forces are furthermore important in tumor growth. Tumors confined by other tissues exert forces onto their environment during growth. Conversely, the tumors experience the same mechanical forces due to the restoring response of the surrounding tissue. The stress that results from cellular growth is termed growth-induced stress [4]. In this doctoral thesis we measure the isotropic part of the stress tensor. Consequentially, we introduce the term growth-induced pressure as the pressure a population of cells exerts during growth and division. External stresses acting on tumors can decrease proliferation [4, 5] and increase apoptosis (programmed cell death) [4, 6]. At the same time these external stresses can promote invasion by cancer cells, thus helping the tumors to progress [6].

Populations of microbial cells under confinement were also found to exert substantial growth-induced pressures of about 0.3 MPa [7]. Microbes (e.g. bacteria and yeast) often grow as multicellular communities, called biofilms, embedded in a matrix consisting of extracellular polymeric substance [8]. Biofilms are found in the soil and in rocks [9, 10], where they can be partially confined. The growth of biofilms on or in stone monuments was found to promote deterioration of the host material [11]. Most of the causes for this biodeterioration are attributed to biochemical factors related to microorganisms [12, 13]. In a few studies it has been argued that mechanical forces attributed to the presence of biofilms in stones can facilitate biodeterioration. Shrinking and swelling cycles of the extracellular polymeric substance of biofilms can induce mechanical stress to the mineral structures of stones and thus change the pore size distribution [11]. Furthermore, the growth-induced pressure exerted by fungal biofilms was found to propagate cracks in marble [14]. When microbes grow in confinement and exert mechanical forces in order to grow, they are also subjected to and influenced by these forces. Microbes adapt their morphology when growing in confinements smaller than their typical size [15–17].

Despite the ubiquitous nature of mechanical forces during growth of cells only few microbial studies address these forces and to the best of our knowledge no reliable method has been established so far that allows for the measurement of growth forces on the population level. In this study we show that growing populations of the yeast *Saccharomyces cerevisiae* can form and propagate cracks in agar gels, and we present a microfluidic chemostat that allows for the measurement of growth-induced pressures *S. cerevisiae* populations exert, while fully controlling the nutrient conditions. Furthermore, our microfluidic chemostat enables us to control the growth-induced pressures the cells exert and experience by employing various leaky cell flow outlets that confine the cell populations to different degrees.

1.1 Structure of this thesis

Several key characteristics of the yeast *S. cerevisiae* are presented in chapter 2. Furthermore, this chapter features examples on how mechanical forces influence cells and which techniques have already been employed to measure mechanical forces exerted by populations of cells in the literature. In chapter 3 the materials and methods necessary to conduct the experiments described in this thesis are presented. Chapter 4 describes the analysis steps that are required for the image processing, data analysis and finite element simulations. The development of the microfluidic device and of the growth-induced pressure measurement technique are discussed in chapter 5. The results of this doctoral thesis are presented in chapter 6 and the corresponding discussion can be found in chapter 6 and 7. Chapter 8 features the summary and conclusion of this doctoral thesis and gives an outlook on possible experiments that can be conducted with the developed microfluidic device. In appendix A several additional results and details about the analysis are presented.

Chapter 2

State of the art

2.1 The cell cycle of *S. cerevisiae*

Most aspects detailed in this section are adapted from [18, 19]. The cell cycle is an asexual reproduction process that generates two genetically identical cells. The cell division of *S. cerevisiae* is asymmetrical. A mother cell produces a smaller daughter, which initially grows as a bud on its mother's cell wall. Hence, *S. cerevisiae* is also known as budding yeast.

In order to commit to cell division a (potential) mother cell has to pass a checkpoint termed Start. At this cell cycle checkpoint the cell checks for nutrient availability, cellular volume and intactness of DNA. If the cell passes this checkpoint, it commits irreversibly to cell division.

The cell cycle of budding yeast can be separated into four main phases shown in figure 2.1.

- In early G1 phase cytokinesis (the process of dividing the cytoplasm) and cell separation of the last cell cycle occur. This is in contrast to mammalian cells, in which cytokinesis and cell separation occur late in the M phase. Furthermore, the cell grows in volume until the cell commits to a new division if the cell passes Start. Upon initiation of Start and before bud formation the mother cell implements a chitin ring into its cell wall at the site of the future bud. The Young's modulus of the cell wall at the site of the chitin ring is higher than the remaining cell wall [20]. This stabilizes the connection between mother cell and bud, while the bud increases in size.

- In the S phase DNA is duplicated in the nucleus and the bud starts to increase in volume.

- In the G2 phase the nucleus migrates towards the bud and the bud keeps on growing. New cell wall material is incorporated in the wall of the bud.

- Mitosis (nuclear division) takes place during the M phase.

Notably, after a cell has committed to cell division (after initiation of Start) the mother cell hardly increases in volume. It mostly grows during the G1 phase. Cells can only delay in their cell cycle during the G1 phase before or at Start for instance under nutrient starvation [21]. The growth delayed phase is termed stationary phase. Stationary phase cells are not metabolically active but they can initiate cell division when nutrients become available [22].
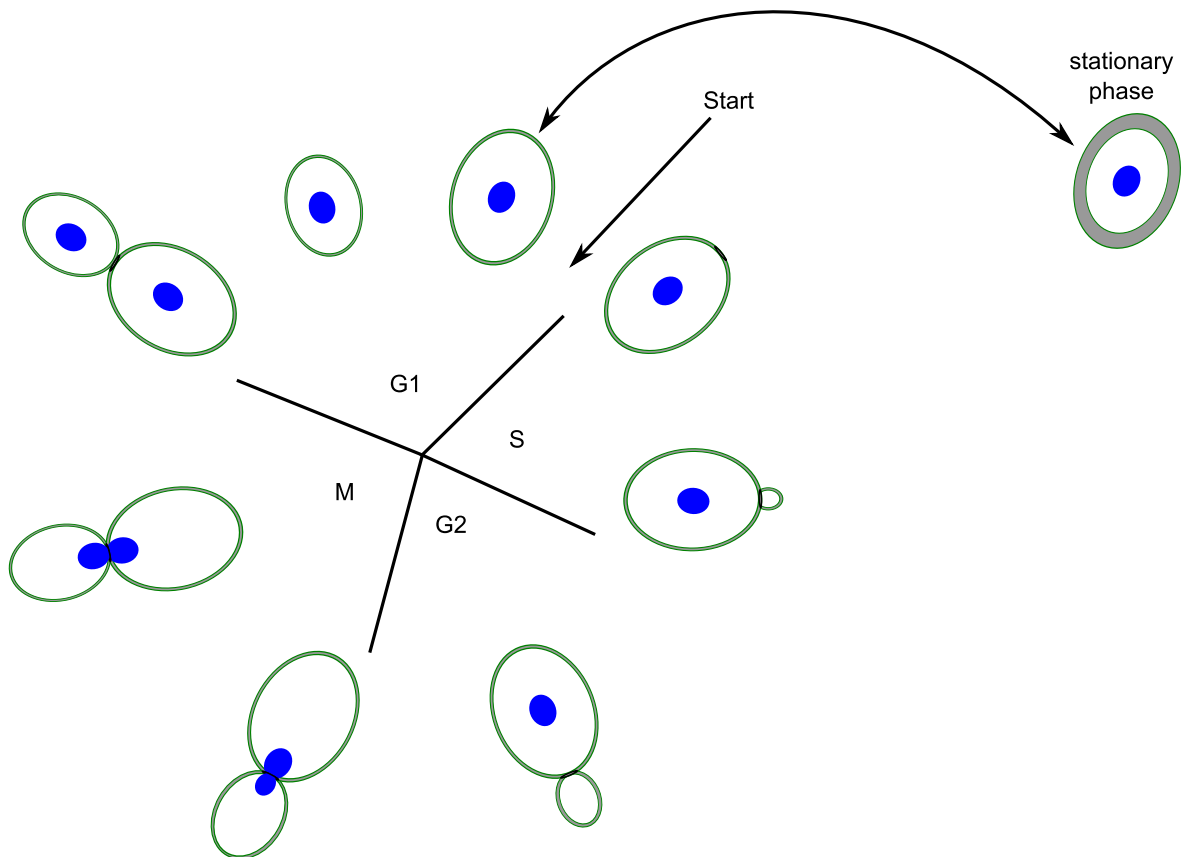
Figure 2.1: A sketch of the *S. cerevisiae* cell cycle is shown. The cell cycle is divided into four phases: The G1 phase, in which cytokinesis (separation of the cytoplasm) occurs and the single cell grows. The S phase, in which the DNA is duplicated (not shown). Then the G2 phase follows, in which the bud grows. Afterwards, the M phase follows, in which the nucleus divides and Start is a checkpoint that can only be passed if certain criteria are fulfilled. E.g. a cell starved for essential nutrients does not commit to cell division, but rather delays in the cell cycle in the stationary phase. The sketch was adapted from [18, 19].

2.2 Turgor pressure

The turgor pressure of a cell is defined as the hydrostatic pressure that results from the difference between internal (Π_i) and external (Π_e) osmotic pressure at equilibrium [23]

$$P_{\text{turgor}} = \Pi_i - \Pi_e. \tag{2.1}$$

For a positive turgor pressure ($P_{\text{turgor}} > 0$) water flows into the cell due to the osmotic pressure difference. As a result a hydrostatic pressure acts onto the cell wall. Figure 2.2 illustrates *S. cerevisiae* cells under positive and zero turgor pressure.

Figure 2.2: a) Sketch of a *S. cerevisiae* cell under positive turgor pressure. The cell assumes its ellipsoidal shape. b) The turgor pressure is zero. The cell shrinks under the absence of the turgor pressure.

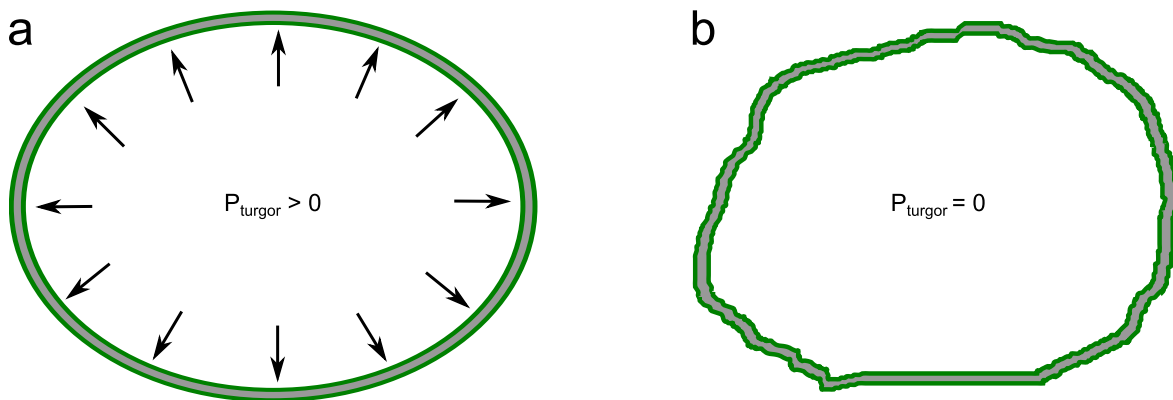When the external osmotic pressure (Π_e) rises *S. cerevisiae* can adapt its internal osmotic pressure (Π_i) to some extent. A *S. cerevisiae* cell achieves this by accumulating glycerol into its vacuole [24]. This glycerol accumulation is mediated by the high osmolarity glycerol (HOG) pathway [25]. The vacuole is the main storage site of solutes in *S. cerevisiae* [26] and hence of utmost importance for osmoregulation and maintenance of positive turgor pressure. Another way to increase the internal osmotic pressure lies in the increase of the internal ion concentration. This ion concentration is probably a passive response to membrane stretching, which induces the opening of mechanosensitive ion channels [27].

Yeasts require a positive turgor pressure in order to maintain their shape and to facilitate cellular growth by means of cell wall stretching [28, 29]. A positive turgor pressure stretches the cell wall, which facilitates breaking of molecular bonds in order to incorporate new cell wall material [17]. When growing under confinement, a yeast cell has to build up a turgor pressure higher than the mechanical pressure acting on the cell wall from the outside. As a consequence the external mechanical pressure at which growth seizes is equal to the maximal turgor pressure a cell can establish [30].

2.3 The cell wall of *S. cerevisiae*

The cell wall of *S. cerevisiae* is essential for osmotic and physical protection and it defines the shape of the microorganism [31, 32]. Furthermore, the cell wall has to be able sustain the turgor pressure or the cell would simply burst.

The thickness of the cell wall in *S. cerevisiae* is about 125 nm [33]. Hence, for a cell with an average diameter of 5 µm the cell wall composes about 14% of the cellular volume.

The cell wall of *S. cerevisiae* consists of two layers, one stiff internal and a softer external layer [32]. The main component of the stiff inner layer is β1,3-glucan (50-55% of the cell wall dry weight) [32]. β1,3-glucan is a polysaccharide that forms 3D networks in the cell wall with a mesh size that allows for permeation of most proteins [34]. Chitin is also part of the cell wall. It is mainly found in bud scars (the sites of cell division) with about 90% of the overall chitin content. Hence, it plays an important role in cell division (see section 2.1). Chitin rich cell wall sections are stiffer than chitin scarce sections [20]. The external layer is mainly composed of cell wall proteins that are bound to the polysaccharide scaffold of the internal layer. These cell wall proteins are important for numerous functions (e.g. cell adhesion, growth, metabolism, etc. [32]). Under adverse growth conditions the composition of both cell wall layers changes to adapt to the environmental cues. The aforementioned values of cell wall size and composition are typically found in exponentially growing cells in glucose-rich medium [32].

Several studies have been conducted to measure the cell wall elasticity of *S. cerevisiae*. Depending on the method used for the measurement the Young's modulus can differ a lot. In atomic force microscope (AFM) measurements the Young's modulus was found to be in the order of 0.1-1 MPa [20, 35–38]. Micromanipulation measurements, in which a cell is compressed between two parallel plates, give a Young's modulus in the order of 100 MPa for the cell wall [39–42]. It has been argued that AFM measurements penetrate the cell wall so little that only the soft external layer, which mostly consists of cell wall proteins, is probed. However, micromanipulation measurements allow for probing of the whole cell wall due to the relatively large deformations [43].

2.4   Cell adhesion of *S. cerevisiae*

Since *S. cerevisiae* cells are nonmotile eukaryotes, cell wall proteins are important for the cells to interact with their surroundings. The adhesins are an essential class among these cell wall proteins. They are required for adhesion to substrates and to other cells [44].

A strong cell-cell adhesion mechanism found in *S. cerevisiae* is known as flocculation, in which cells form velcro-like interconnections [45]. Interestingly, most lab strains (e.g. S288c) have been evolved against flocculation by human selection, such that they do not adhere in contrast to their undomesticated counterparts (e.g. BR-F). This inability to flocculate arises from a mutation in one of the flocculin-encoding genes found in *S. cerevisiae*. This mutation prohibits the lab strain to express the cell wall flocculins (proteins) flo1p and flo11p. Flo1p is essential for cell-cell adhesion while flo11p drives the adhesion of cells to (abiotic) substrates [46].

The undomesticated yeast strain BR-F is capable of local flocculation between single cells and cells belonging to this strain can form long chains of cells known as pseudohyphae. These pseudohyphae enable the otherwise nonmotile cells to access nutrient sources away from the initial colony [47]. Furthermore, the BR-F cells are able to invade agar, when grown on a flat surface of agar and starved for essential nutrients [48]. It has been shown that the flocculin flo11p is required for both pseudohyphae formation and surface agar invasion [49]. This explains why the lab strain S288c does neither form pseudohyphae nor invades agar surfaces. Figure 2.3 shows an example of such an agar invasion for BR-F yeasts. We let colonies of BR-F yeast grow on YPD agar surfaces at room temperature. YPD is a glucose rich growth

medium for *S. cerevisiae.* After about 3 days we observe that the cells invade the agar gel as small roots beneath the colony. In our experiments the lab strain S288c has never shown any sign of agar invasion.

The flocculin flo1p (involved in cell-cell adhesion) provides a remarkable adhesion strength. An average force of 2000 pN is needed to separate two *S. cerevisiae* cells that had an initial contact area radius of about 90 nm [50]. These values translate to an adhesive pressure of about 80 MPa. This value is roughly 65 times as high as the largest growth-induced pressure we measured in our BR-F strain experiments (1.2 MPa). El-Kirat-Chatel *et al.* found that cells of the lab strain S288c do not exhibit any measurable adhesion strength and hence do not adhere noticeably to each other [50], except during cell division.
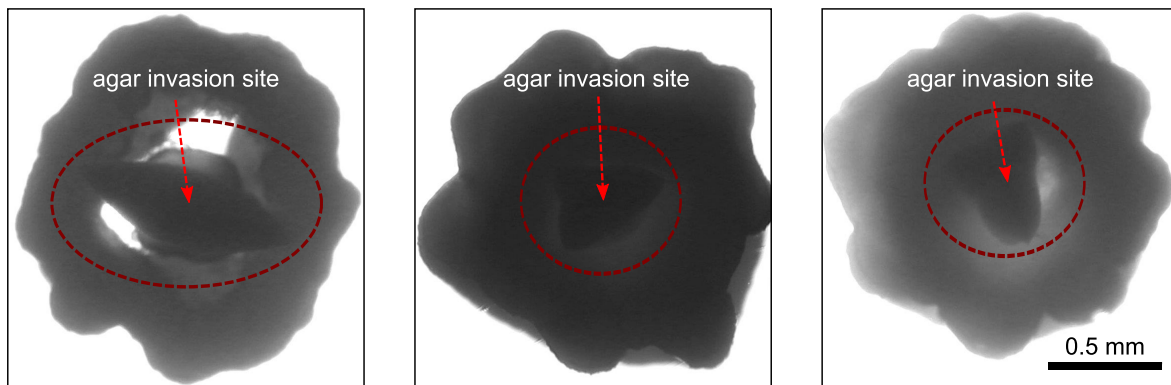

Figure 2.3: Three examples of agar invasion by BR-F yeast. The yeasts were grown at room temperature on a YPD agar surface for about 3 days until we observe the formation of roots beneath the agar surface. This root formation is due to the invasion of agar surfaces by the BR-F strain.

2.5 *S. cerevisiae* under stress

Yeast cells react to (sudden) environmental changes via stress responses. The first broadly studied stress response is the heat shock that has been investigated in *S. cerevisiae* since the beginning of the seventies. A sudden increase in environmental temperature results in extensive changes in the cell's gene expression. Following the heat shock, total protein synthesis is down-regulated while the transcription of heat shock protein genes is heavily up-regulated. The synthesized heat shock proteins facilitate the repair and recovery of the cell from harmful conditions. Furthermore, this increased abundance of heat shock proteins help the cell to resist further stresses. This stress tolerance buildup is probably the most important result of the cellular stress response [51].

It has been shown that *S. cerevisiae* shows similar responses to a diversity of stresses e.g. exposure to salt, to reactive oxygen species, to heavy metals or to acids, starvation or increase in osmolarity [51]. Each individual reaction to stress in *S. cerevisiae* is part of a general protective program, the environmental stress response. Since the same program is activated under various environmental stresses, cells that experience one stress acquire resistance to a second different environmental stress [52]. Furthermore, stress sensitivity seems to be related to the growth conditions. Yeast cells undergoing fast proliferation show weak stress resistance [53] while cells close to the stationary phase are more resistant to stress

[54, 55]. Elliott and Futcher have shown that a slow growth rate is strongly correlated to an increased resistance to heat shock and degradation of the cell wall by the enzyme Zymolyase [56]. Furthermore, in a recent study first evidence was provided that cells are more resistant to mechanical stress when cultured at slow growth rates [57]. Additionally, the position of the cell in its cell cycle has hardly any influence on its stress resistance [56]. These findings provide first hints that increased stress resistance is not unique to stationary phase cells. The stationary phase rather marks the end of the spectrum with total growth delayed cells expressing the highest stress resistance [56].

The adaption of turgor pressure can also be understood as a stress response. Under hyperosmotic shock *S. cerevisiae* cells shrink. This can lead to a decrease in growth rate since growth and cell division are only possible if a cell maintains a minimal volume. As a response to hyperosmolarity *S. cerevisiae* cells can increase their turgor pressure in order to recover their size [51].

2.6   Clogging and jamming

In many-particle-systems clogging is readily observed when large numbers of particles pass through bottlenecks [58]. Depending on the geometry of the orifice the flow of particles is fluid-like, intermittent or completely clogged [58]. In a completely fluid-like flow no clots appear while in a completely clogged systems no particle movement occurs through the orifice. An intermittent flow is observed when clots take turns with fluid-like behavior [58, 59]. A clot can be dissolved when the driving force of the system is large enough to overcome frictional forces between neighboring cells or between cells and the surrounding material of the orifice [60].

Interestingly, the widening and subsequent closing of an escape channel can promote clogging. Helbing *et al.* simulated pedestrians escaping through channels similar to the one depicted in figure 2.4 [61]. They found that clots form more frequently for larger channel widening and narrowing angles. We exploit this finding by designing analog structures to control the flow of *S. cerevisiae* cells (cf section 5.1.1).

In a clogged state a many-particle-system might get jammed. A jammed system does not deform irreversibly under small finite stresses, while flows occur at any stress in an unjammed system [62]. Clogging and jamming are not necessarily the same phenomenon. Particles that
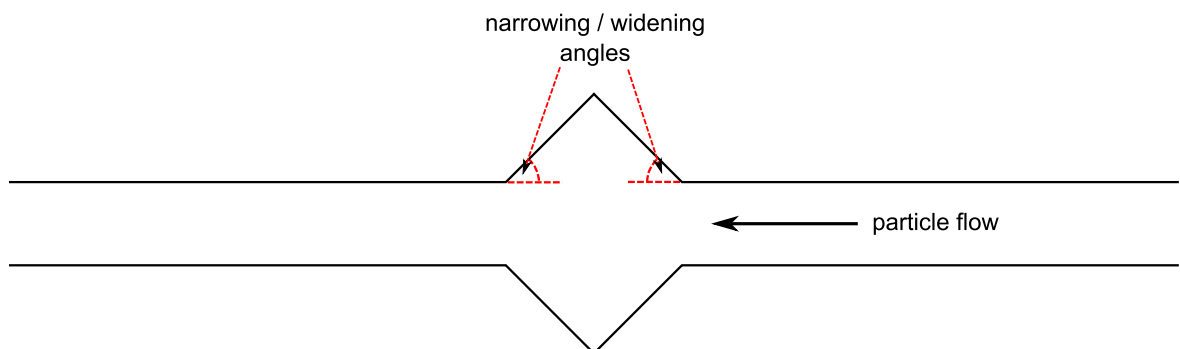

Figure 2.4: A sketch of an escape channel is illustrated. The subsequent widening and narrowing of the channel promotes clot formation. The larger the channel the more clogging occurs [61]. The sketch was adapted from [61].

are trapped by a clot might still rearrange. These rearrangements would be incompatible with the definition of a jammed state. A clot can also be thought of as a local jamming event, since a clot must not deform irreversibly in order to be preserved.

2.7 Forces in cellular growth and division

2.7.1 Consequences of growth forces

The growth forces that cells exert onto their surroundings can be exploited in various ways. Single bacteria of the species *E. coli*, *B. subtilis* and *P. aeruginosa* have been encapsulated in agarose hydrogels [63]. When these bacteria grow, they deform the surrounding gel matrix. The cell wall elasticity of these bacteria can be extracted from the displacement of the surroundings as 50-150 MPa for *E. coli*, 100-200 MPa for *B. subtilis* and 100-200 MPa for *P. aeruginosa* [63]. Another way to exploit the growth forces of cells is to grow microbial colonies into long vertical cylinders. The yeast *S. cerevisiae* can form cylinders with a height to diameter aspect ratio of 4:1 on paper filters lying on nutrient agar surfaces. To achieve this vertical growth the nutrient supply to the colony is horizontally constrained by blocking the pores of the filter paper with polydimethylsiloxane (PDMS). The growth forces enable the cells in contact with the nutrient source to push thousands of cell layers in the upper part of the cylinders towards the vertical direction [64].

Cells are also able to mechanically interact with their surroundings via growth forces. The growth of populations of the rod-shaped bacterium *E. coli* in microfluidic channels can induce ordering of the cells. This ordering is observed as a transition from a disordered phase to a nematic phase. The long axis of the cells align during this transition. The growth forces can be interpreted as mechanical short range interactions that lead to a large scale ordering in the bacterial population [65]. Furthermore, the ordering of *E. coli* under confinement by microfluidic channels is believed to facilitate escape of cells from the confinement and diffusion of nutrient into the bulk of the population [66].

Cells that grow under physical constraint can change their shape due to the growth forces acting on them. *S. cerevisiae* cells grown in rigid cubic holes adapt their shape to the physical constraint [15]. From our point of view it is not yet clear if the cell wall is only elastically deformed or if the cell wall architecture is remodeled in the case of *S. cerevisiae*.

Gram-negative bacteria have a thinner cell wall than gram-positive bacteria. Gram-negative bacteria *E. coli* are able to squeeze through rigid channel with a width half as large as the short axis of the cells. They push each other through a narrow channel with help of forces exerted by growth and division of the cells. When the *E. coli* cells escape the channel they show distorted cells shapes. These shape changes most likely enable the cells to pass through the channels in the first place and are a result of an adaption of cell wall architecture. Interestingly, gram-positive bacteria of the species *B. subtilis* are not able to pass through channels narrower than their short axis. Furthermore, *B. subtilis* cells do not alter their shape in the way *E. coli* cells do. Männik *et al.* attribute this inability to traverse narrow channels to the thicker cell wall the gram-positive *B. subtilis* possess (about 30-40 nm compared to 3 nm for the gram-negative *E. coli*) and to the higher osmotic pressure acting inside of *B. subtilis* cells, which is as high as 2-5 MPa compared to 0.2-0.3 MPA in the case of *E. coli* [16].

When gram-negative *Caulobacter crescentus* bacteria are grown in cylindrical holes they adapt their cell wall curvature to the physical constraint of the holes. After removal from the

physical constraint the cells retain their curvature when further cellular growth is inhibited. This shows that the physical constraint initiates an adaption of cell wall architecture in the gram-negative bacterium *C. crescentus* [17].

2.7.2   Measurement of growth-induced pressure

Few techniques have been developed to measure the growth-induced forces (or pressures) cells exerts. Cheng *et al.* embedded cancer spheroids (non-metastatic murine mammary carcinoma 67NR cells) and fluorescent beads in agarose gels [4]. The displacement of the beads was measured to access the stress field around tumor spheroids. A growth-induced pressure of about 3.7 kPa was measured after 30 days of growth. The growth of the tumors in confinement was followed by cellular necrosis. Upon stress release, which resulted from the formation of cracks in the agarose gels, tumor growth was resumed [4].

In another study tumor spheroids (WT mouse colon carcinoma CT26, HeLa and mouse sarcoma S180 cells) were enclosed in permeable, deformable, hollow microspheres made of alginate. Once the tumor cells started to deform the shell of the microsphere the growth-induced pressure exerted by the tumor could be measured from the deformation. After 8 days growth-induced pressures of about 3.3 kPa were measured. In terms of dynamics the pressure curves of all tested cell types share a common behavior. For the first 24 hours the growth-induced pressure showed a fast linear increase of about 2.4 kPa/day. The pressure increase slowed down to about 0.2 kPa/day for the remainder of the experiments [67].

To measure the growth-induced pressure of rod-shaped fission yeast *S. pombe*, single cells were entrapped in cylindrical holes molded into PDMS. When a cell starts to grow against the PDMS walls, the growth-induced pressure is inferred from the PDMS deformation. The stalling pressure, at which growth ceases is equal to the maximal turgor pressure these cells can build up. Minc *et al.* measured the maximal turgor pressure of *S. pombe* to be 0.85 MPa. However, the approach of Minc *et al.* to measure growth-induced pressures is limited to single cell measurements [30].

A cell reactor for studies of growth-induced pressures of whole microbial populations was designed by Stewart and Robertson in 1989. A population of *E. coli* was confined in a steal casing. The exerted growth-induced pressure was measured by a pressure transducer, which was sensitive to the deformation of a membrane in contact with the bacterial population. A maximal growth-induced pressure of about 0.3 MPa was observed for *E. coli*. In these experiments higher pressure values could not be measured, since cells started to leak from the device. Additionally, their device does not allow for direct observation of cells during the pressure measurement. Cells had to be taken out in order to take microscopic images. They could modify their device to actively impose a mechanical stress onto cell populations. A simultaneous growth-induced pressure measurement was not possible due to the required modification. Stresses up to 0.9 MPa were applied for 12 hours onto the cell populations. The cells were removed from the device and their average volume was measured. Stewart and Robertson found that the average cell volume decreased with an increase in applied stress [7].

In this section we introduced how other research groups have measured growth-induced pressures of various cells. In the following chapters we will describe our experimental approach and the results obtained from our measurements.

Chapter 3

Materials and methods

3.1 Fabrication of microfluidic devices

The microfluidic devices presented in this thesis were molded into polydimethylsiloxane (PDMS). PDMS is fabricated by mixing two liquid chemicals (a base and a curing agent), which will cure after mixing in 1 to 24 hours depending on temperature [68]. It has a Young's modulus in the order of 0.1 to 1 MPa, which can be altered by using different base to curing agent ratios [69] or curing temperatures [70]. To create the devices from PDMS a mold is required, that we fabricate using photolithography on silicon wafers. In the following, a master is the structured silicon wafer used to mold PDMS. The various steps of fabrication are detailed in the next section.

3.1.1 Photolithography

Masters for parts of the microfluidic chips were created from silicon wafers (WaferNet Inc., USA) and negative photoresists SU-8 2000.5 and SU-8 3010 (MicroChem Corp., USA) using photolithography [71]. In principle, one can fabricate multilayer molds, which permit to have structures at different heights. In this thesis, we used single and double layer devices, whose fabrications are presented in the following.

It is essential to conduct the fabrication process in a cleanroom or otherwise dust particles can easily accumulate on the surface of the silicon wafer and thereby prohibit the fabrication of cohesive and well defined structures. The microfabrication of the master with photolithography is a multistep process. In order to fabricate single layer devices one has to simply leave out steps 3 to 8 in the following description.

1. A silicon wafer with a diameter of 10 cm was rinsed first with acetone (Sigma-Aldrich Corp., MO, USA) and than with isopropanol (Sigma-Aldrich Corp., MO, USA). Afterwards the wafer was dried using a N_2 blowing gun (figure 3.1a). The wafer was checked for visible particles on its surface (e.g. dust) and if any are observed the cleaning step was repeated.

2. The cleaned wafer was placed onto a hotplate set to 200°C for 10 minutes to dehydrate the surface. This helps to achieve a better adhesion between photoresist and substrate in the next step. Subsequently, the wafer was set aside from the hotplate to cool it down to room temperature. If the wafer were not cooled down, the photoresist that was poured onto it in the next step would evaporate more quickly leading to a non-reproducible photoresist layer height.

3. The wafer was mounted onto the chuck of a spin coater and 2 ml of negative photoresist SU-8 2000.5 was poured on it so that roughly two thirds of the wafer surface was covered. Initially, the wafer was spun at 500 rpm (100 rpm/s acceleration) for 10 seconds to distribute the photoresist over the whole surface. The spinning speed was increased to 3000 rpm for 30 seconds (300 rpm/s acceleration). After spincoating the thickness of the photoresist layer was approximately 0.5 µm (figure 3.1b).

4. The thickness of the photoresist was not completely uniform. Photoresist tended to accumulate during the spincoating on the edge of the wafer. This elevated part could lead to a bad resolution of the structures since it introduces a cavity between mask and wafer during exposure (see step 5). It was possible to get rid of this photoresist edge by wiping the rim of the wafer with a cleanroom wipe soaked with acetone at an angle of approximately 45° (figure 3.1c).

5. The wafer was soft-baked on a hotplate at 95°C for 1 minute and cooled down to room temperature afterwards. When the wafer had cooled down the photoresist layer should have hardened and lost its stickiness. If the wafer was still sticky it was put back onto the 95°C hotplate to let it soft-bake for one more minute and it was again checked for stickiness after letting it cool down (figure 3.1c).

6. To deposit structures onto the silicon wafer the photoresist layer has to be selectively exposed to i-line UV light (365 nm). This was accomplished by placing a mask over the silicon wafer and exposing it with 365 nm light through the mask. Quartz chromium masks were used, whereas the chromium site was in contact with the soft-baked photoresist. The mask also contained alignment marks that were transferred onto the wafer. These marks are necessary to align the wafer with a second mask in a later step so that the two different photoresist layers are positioned properly with respect to each other. Wafer and mask were mounted into a mask aligner (OAI mask aligner) to allow for good contact and alignment of both parts. The smallest structures we wanted to resolve have a size of 1 µm, for this required resolution it is important to bring the wafer and the mask in very tight contact. This was possible by using the hard contact mode of the mask aligner, in which the wafer was pushed against the mask with an additional force. For a structure height of 0.5 µm a exposure dose of about 60 mJ / cm^2 gave good results (figure 3.1d).

7. After exposure the wafer was baked for one minute on a hotplate at 95°C (post-exposure-bake, PEB) and cooled down to room temperature. As a result the parts that had been exposed to UV light in the previous step were now well cross linked (figure 3.1e).

8. The remaining parts that had not been exposed to UV light were removed chemically by immersing the wafer in a SU-8 developer (MicroChem Corp., USA) bath for 1 minutes. The wafer was removed from the bath and rinsed with SU-8 developer for 10 seconds. The remaining SU-8 developer was removed by rinsing the wafer with isopropanol for 10 seconds and drying it with a N$_2$ blowing gun (figure 3.1f).

9. The second layer of photoresist was spincoated onto the already structured wafer (or the cleaned smooth wafer in the case of a single layer device). For this layer 4 ml of SU-8 3010 was poured onto the wafer so that about two thirds of the surface were covered. In a first spin coating step of 500 rpm for 10 seconds with an acceleration of

100 rpm/s the surface was completely covered with photoresist. In the second step the spinning speed was increased to 3000 rpm for 30 seconds with an acceleration of 300 rpm/s. This yielded a photoresist height of approximately 10 μm (figure 3.1g).

10. The elevated edge and the photoresist covering the alignment marks were removed with a clean room wipe (figure 3.1h).

11. The wafer was softbaked for 7 minutes at 95°C on a hotplate and cooled down again. If the photoresist was still sticky after cooling, it was again heated for 2 minutes (figure 3.1h).

12. The wafer was mounted with another mask, carrying the (second) structures, into the mask aligner. The previously transferred alignment marks on the wafer were manually aligned with the alignment marks on the mask. Alignment was only necessary for devices consisting of two layers. This was done to properly position the two layers of photoresist with respect to each other. After alignment the wafer was exposed with an energy density of 150 mJ / cm^2, which was appropriate for the aimed structure height of 10 μm (figure 3.1i).

13. The wafer was post-exposure-baked for 3 minutes at 95°C and cooled down afterwards. If the wafer were not cooled down before it comes into contact with the developer, the photoresist might crack rendering the structured wafer unusable.

14. The photoresist that had not been exposed to UV light was not crosslinked and was removed by immersing the wafer in SU-8 developer for 3 minutes. The wafer was rinsed afterwards for ten seconds with SU-8 developer and subsequently, washed with isopropanol for another ten seconds. The structured wafer was dried with a N$_2$ blowing gun (figure 3.1j).

15. In a last step the structured wafer was hard-baked for 30 minutes at 150°C to enhance the adhesion between photoresist and silicon wafer.

3.1.2 PDMS molding and device preparation

We used Sylgard 184 (Dow Corning Corporation,USA) elastomer kits to fabricate PDMS molds. Two chemicals are part of this kit, a base and a curing agent. Base and curing agent were mixed in a mass ratio of 10:1 (as recommended by the manufacturer). The mixture was put under a low pressure environment in a desiccator for 60 minutes to get rid of air bubbles trapped in the mixture. The degassed mixture was poured over a structured silicon wafer that had previously been placed into a Petri dish. The typical height of the PDMS layer we prepared was 1 cm. The wafer with the PDMS was placed once again under a low pressure environment for 15 minutes (usually a few bubbles formed when pouring the PDMS onto the structured wafer). The degassed PDMS on the silicon wafer was placed in an oven over night that ran at 60°C to completely cure the PDMS (figure 3.2a).

A rectangular PDMS bloc containing the structures of the device was cut out with a scalpel and gently detached from the silicon wafer (figure 3.2b). Holes were punched into the PDMS bloc with a Standard FUE puncher (Mediquip Surgical, USA) with an outer diameter of 0.75 mm at positions of the inlets that were required for the device operation (figure 3.2c).

A round glass coverslip (VWR International GmbH, Darmstadt,Germany) thickness No. 1 (0.13 to 0.17mm) with a diameter of 2.5 cm and the previously prepared PDMS bloc were
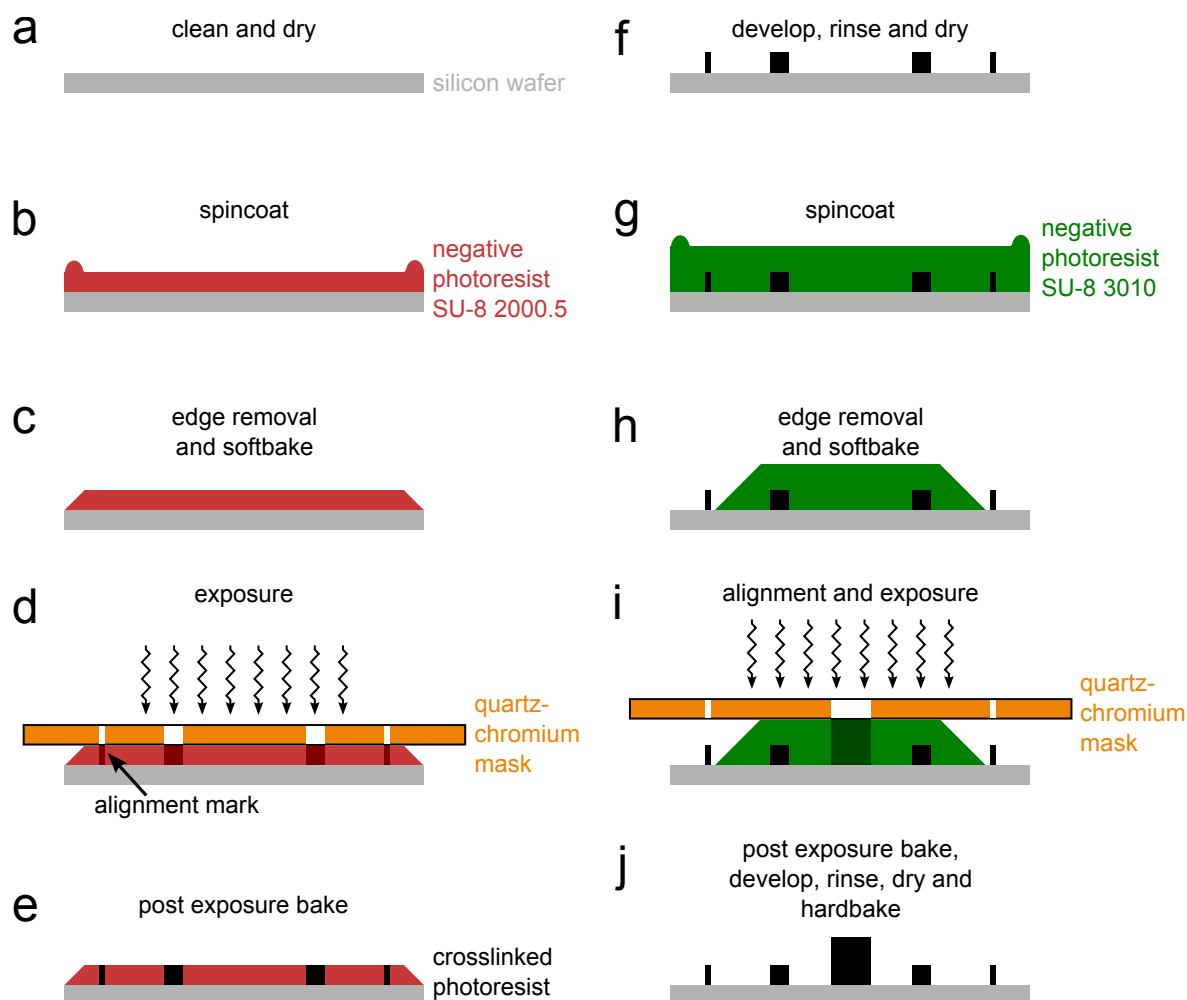
Figure 3.1: Photolithography for the fabrication of a double layered silicon wafer: a) A clean and dry wafer was prepared. b) Negative photoresist was spincoated onto the wafer and an elevated edge remains. c) The photoresist edge was removed and the remaining photoresist is softbaked. d) A quartz-chromium mask was brought into contact with the softbaked silicon wafer and the wafer was exposed through the mask with 365 nm UV-light. e) A post-exposure-baking step crosslinked the UV-exposed parts of the negative photoresist. f) The remaining non-crosslinked photoresist was dissolved by immersing the wafer in SU-8 developer. g) A second layer of photoresist was spun onto the wafer. h) The edges were removed and the alignment marks were freed from photoresist. i) A second mask was aligned with respect to the alignment marks, brought into contact with photoresist layer and exposed. j) The photoresist was post-exposure-baked and the non-crosslinked parts were dissolved by a developing step. After cleaning the wafer was hard baked to enhance the crosslinking of the photoresist.
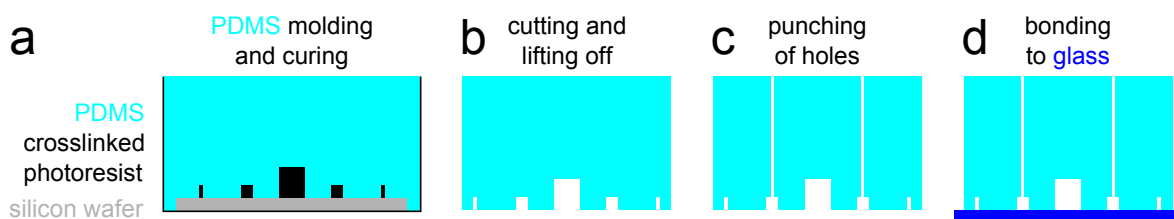
Figure 3.2: PDMS molding and preparation of microfluidic device: a) Base and curing agent were previously mixed at a mass ratio of 10:1, degassed, poured onto a structured silicon wafer to give an approximate height of 1 mm and degassed again to remove air bubbles from the mixture. The PDMS was cured overnight at 60°C. b) A rectangular bloc including the structures was cut out from the cured bulk PDMS and removed from the wafer. c) Holes were punched into the PDMS bloc to connect syringes to the microfluidic channels via tubing. d) A glass slide and the PDMS bloc were rinsed with isopropanol and dried with N_2. Afterwards both were placed in an oxygen plasma. After removing both parts from the oxygen plasma, they were brought into contact to form irreversible bonds.

rinsed with isopropanol and dried with a N_2 blowing gun. PDMS and glass treated with oxygen plasma form silanol groups (Si-O-H) on their surfaces. When bringing both surfaces into conformal contact Si-O-Si groups form resulting in irreversible bonds [72–74]. In order to achieve a strong irreversible bond glass slide and PDMS bloc were placed in an oxygen reactive ion etching (RIE) plasma chamber so that the sides that were supposed to be bound are facing upwards to be optimally exposed to the oxygen plasma. Air was pumped out of the chamber and oxygen was let in to give a pressure of about 21 Pa. The power of the chamber was adjusted to 100 W for 20 seconds. Afterwards the pressure in the chamber was equilibrated with the environmental pressure in about 5-10 seconds. Immediately once the chamber could be opened the glass slide and the PDMS bloc were brought into contact (figure 3.2d). Additionally, we gently pushed onto the PDMS bloc to enhance the bonding of glass and PDMS.

3.1.3 Composite PDMS device

For one application we required a device consisting of two layers of PDMS that were bound together. This device is different from the one we constructed by using double layer photolithography (compare section 3.1.1). We required a 10 µm thick sheet of PDMS between the different structured layers, which can not be accomplished with only one structured wafer no matter the number of photoresist layers. In figure 3.3 a sketch is shown that illustrates this device. The red structure is part of the upper layer of the device, while the black structures show the lower layer. Two layers are required since the valve is supposed to close the channel underneath by pushing onto the PDMS sheet (for details about this device see section 5.3.1). This kind of valve was previously introduced by Quake *et al.* [75], it is thus called Quake valve.

Figure 3.4 illustrates the fabrication process for a device consisting of two PDMS layers. First of all liquid PDMS was prepared as described in section 3.1.2, but with a base to curing agent ratio of 15:1 for the lower layer. This ratio results in a softer PDMS than the standard recipe. We require a higher deformability to effectively tighten channels in the lower layer. We took about 5 ml of the still liquid PDMS mixture and poured it onto a structured
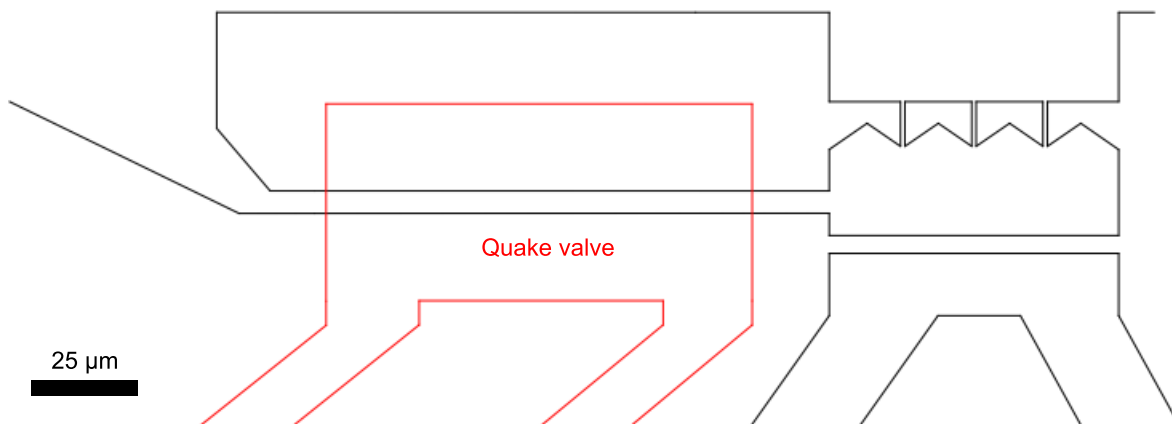
Figure 3.3: A sketch of the composite PDMS device is shown. For this device two layers of PDMS are required. The structures of the two layers are separated by a 10 µm PDMS sheet, when bound together. The red valve closes to black channel when the hydrostatic pressure in the valve is increased. This valve was introduced by Quake *et al.*, it is hence called Quake valve [75].

silicon wafer with a structure height of approximately 10 µm (figure 3.4a). We spincoated the wafer initially with a rotational speed of 500 rpm with an acceleration of 100 rpm/s for 10 seconds to completely cover the wafer with PDMS. In a second step the rotational speed was increased to 2000 rpm with an acceleration of 300 rpm/s for another 120 seconds. This recipe yields a PDMS layer height of about 20 µm, which was measured with a profilometer, Dektak XT (Bruker Corporation Billerica, MA USA). The structures were completely submerged in PDMS and an additional 10 µm of PDMS lies on top of the structures, which served as the deformable sheet (figure 3.4b). Another mixture of PDMS in this case at a base to curing agent ratio of 6.7 to 1 was identically processed and poured over a second structured wafer to give a PDMS height of about 1 mm. This yielded the top layer of our composite PDMS device. Both PDMS layers were cured over night at 60°C. A bloc of PDMS carrying the structures was cut out for the top layer (figure 3.4c), while the lower layer remained attached to the wafer. Both layers are exposed to an O_2 plasma as described in 3.1.2. The two layers were aligned with respect to each other, so that the required parts of the two layers intersect horizontally. The two parts were aligned with a stereo microscope (custom built by Dr. Jiseok Lim) and brought into contact to form irreversible bonds (figure 3.4d). They were baked in an oven for an hour at 75°C following the bonding to further strengthen the bonds. In another step we cut into the lower layer of PDMS along the outer rim of the top layer and lift off the composed PDMS device (figure 3.4e). The holes for the inlets were punched into the PDMS and the composed device was bound to a glass slide as described in section 3.2 (figure 3.4f).
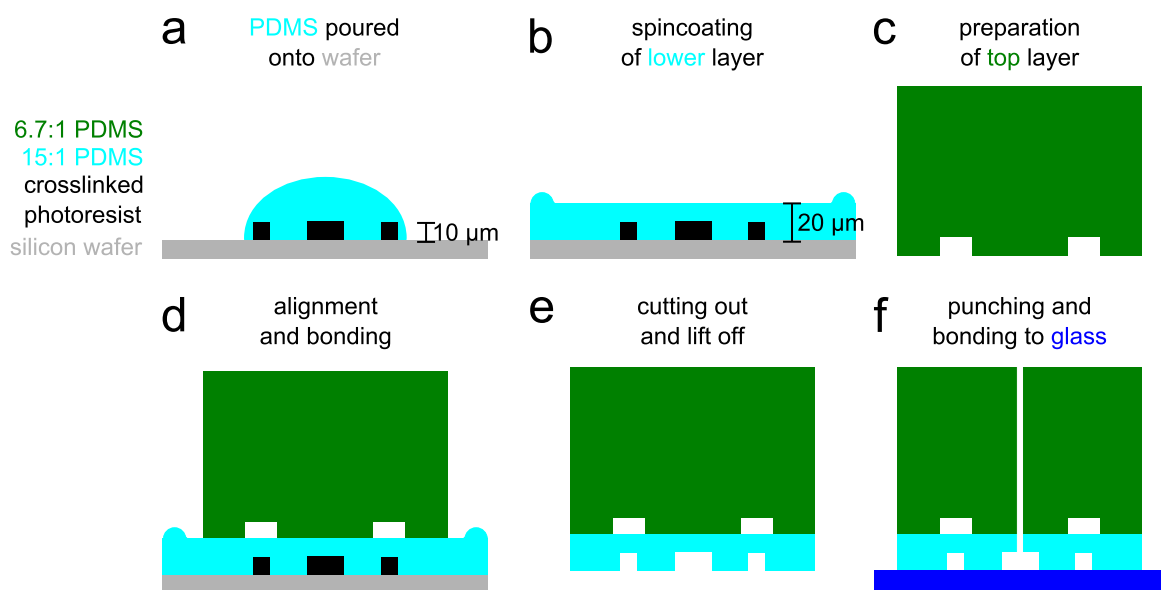
Figure 3.4: PDMS molding and preparation of composite PDMS device: a) A droplet of 15:1 liquid PDMS was poured onto a structured wafer. b) Spincoating to give a PDMS layer height of 20 µm. c) A bloc of 6.7:1 PDMS was cut out from second wafer. d) Alignment and bonding of the two layers. e) Cutting out of lower layer and lifting off from silicon wafer. f) Punching of holes and bonding to glass slide of the composite device.

3.2 Cell strains and culture

In the experiments discussed in this thesis cells belonging to the species *Saccharomyces cerevisiae* also known as baker's yeast were probed. We used several strains of this species in these experiments.

3.2.1 *Saccharomyces cerevisiae* strains

A derivative of the strain K699 [76, 77], which we term ParisCFP, was genetically modified so that it expresses the cyan fluorescent protein (CFP) [78]. We received this strain from Erin O'Sheas laboratory. The CFP in this strain can be found everywhere in the cytoplasm resulting in a non specific staining.

Additionally, we conducted experiments with a strain derived from S288c [79]. This derived strain is termed Whi5-GFP. It has a green fluorescent protein (GFP) attached to the protein Whi5. Whi5 is a cell cycle repressor, that acts on the late G1 checkpoint called Start in *S. cerevisiae*. It has a nuclear sublocalization, and relocates to the cytosol owing to multiple phosphorylations, at the onset of Start. Hence, its cellular sublocalization is an indication whether the cell in the cell cycle is located before Start (nuclear signal in figure 3.5) or has committed, irreversibly, to the cycle and further cell division (cytosolic signal in figure 3.5) [80]. We used a standard (not genetically modified) S288c strain in the experiments conducted with agar gels (cf section 3.3).

We also used an undomesticated strain of *S. cerevisiae* termed BR-F. In contrast to our lab strains (ParisCFP and S288c), this undomesticated strain is able to form strong cell-cell cohesive bonds, whose formation is made possible by the expression of flocculin proteins [50].
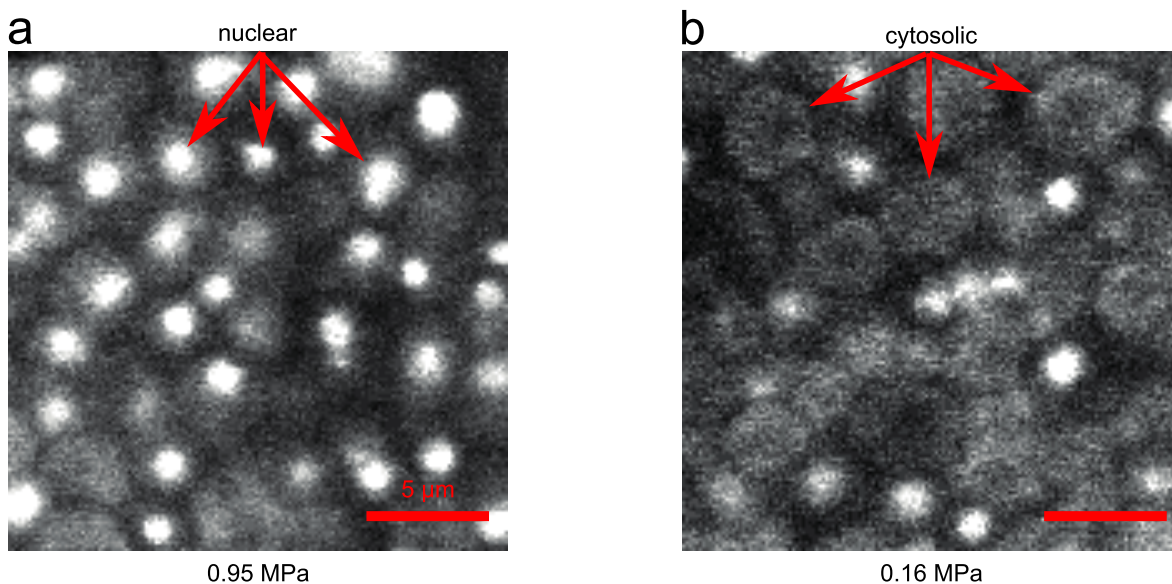
Figure 3.5: Microscopic images of the fluorescent signal during the cell cycle are shown for the Whi5-GFP yeast strain. When in G1 phase the Whi5 protein is concentrated in the nucleus, while the protein is found in the cytosol when it has committed to the cell cycle. Bright dots show cells currently in G1 phase a), whereas the more diffusive fluorescent signal with lower intensity depict cells that have committed to cell division b). The images were acquired at different growth-induced pressures.

3.2.2   Cell culture

We used two different media to culture cells YPD medium [81] and Complete Synthetic Medium (CSM) [82]. Cells were stored at -80°C, and thawed when needed. Initially, we took a small portion of the frozen cultures by scraping the surface with a 200 µl pipette tip and immersed the cells into one of the liquid media in a culture tube (VWR International GmbH, Darmstadt, Germany). The culture tube was put on a shaker (KS 260 basic, IKA®-Werke GmbH & CO. KG, Staufen, Germany) to counteract sedimentation situated in an incubator (KB 115, Binder GmbH, Tuttlingen, Germany) running at 30°C or at room temperature over night. We stroke liquid cell culture using an inoculation loop (VWR International GmbH, Darmstadt, Germany) onto a Petri dish (VWR International GmbH, Darmstadt, Germany) containing YPD or CSM agar. The corresponding agar (Sigma Aldrich, MO, USA) was fabricated by dissolving 2 vol % agar in liquid medium, which was poured into Petri dishes before solidification. The inoculated Petri dish was put into the incubator for two to three days until the cellular colonies on the agar surface had grown to a size of approximately 2 mm in diameter. The agar Petri dish was stored in a refrigerator at 4°C. We picked one colony from the agar Petri dish and resuspended it in liquid medium. The culture tube was put on the shaker in the incubator at 30°C for 4 hours or at room temperature over night. This liquid medium with cells was filled into an 1 ml syringe (Terumo Medical Corporation, USA) to be loaded into the microfluidic device. In the microfluidic experiments we loaded one to ten cells into a chamber. The experimental time zero t_0 was reached when the cells filled the whole chamber, which is accomplished by their cell division. As a consequence the absolute number of cells in the medium, before we inject the cells into our device, is of no

importance.

3.3   Cracking of agar gels

Several experiments were conducted to study cracking of agar gels under the influence of growing cell populations. In order to observe the formation or propagation of cracks two sets of experiments were designed in the scope of this thesis.

To study the propagation of cracks Petri dishes with 5 cm diameter and 1 cm height, were filled with liquid YPD agar gel that solidified after cooling down. A liquid yeast culture that grew overnight at room temperature was previously prepared. A syringe needle tip (Terumo Medical Corporation, USA) with a outer diameter of 0.4 mm was immersed into the liquid cell culture and directly punched into solid agar gel. This punching drove a hole (including initial cracks) into the agar gel and transferred yeast cells into the hole (figure 3.6I).

In order to study if yeast cells can also create cracks when growing, cellular colonies were completely trapped in agar gel matrices. Furthermore, we can measure the growth-induced pressure of a colony completely embedded in agar gel in the same experiment. Liquid YPD agar at 50°C was poured into Petri dishes to give a layer height of about 2 mm. This layer of YPD agar was cooled down to room temperature in order for it to solidify. A yeast colony, previously grown on another YPD agar Petri dish, was scraped from the surface and immersed into liquid YPD agar at 50°C in a preheated (50°C) 1.5 ml eppendorf tube. The colony and
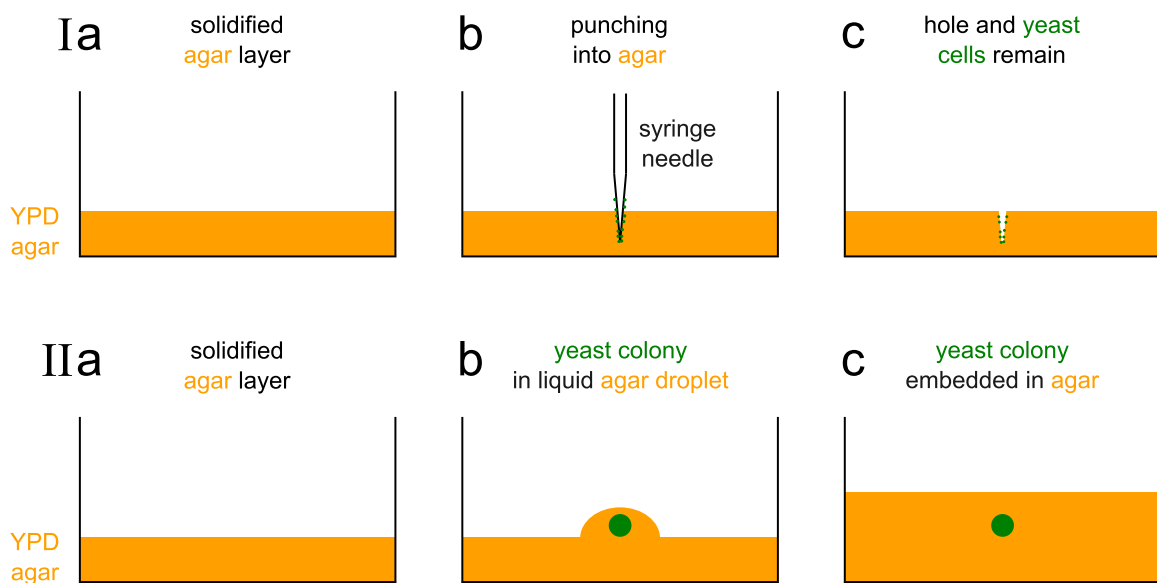

Figure 3.6: Preparation of agar gel crack experiments to study crack propagation I and crack formation II. Ia) In order to study crack propagation a solid layer of YPD agar was prepared. Ib) A syringe needle previously dipped in a liquid yeast cell culture was punched into the agar layer. Ic) The syringe needle was removed and a hole of the size of the needle remained with yeast cells covering parts of the hole surface. IIa) A YPD agar layer with a height of 2 mm was prepared. IIb) A yeast colony submerged in a liquid YPD agar droplet was transferred onto the first layer. IIc) Another layer of 2 mm liquid YPD agar was poured into the Petri dish onto the still liquid droplet of YPD agar so that the colony was completely immersed.

the liquid YPD agar was aspired with a 1 ml pipette tip[*], which was also heated to 50°C and a droplet of the liquid YPD agar containing the colony was placed onto the previously prepared YPD agar layer. Before the droplet solidifies liquid YPD agar is poured over the droplet to fill the Petri dish with another 2 mm high layer of agar (figure 3.6II). When the YPD agar had become solid the Petri dish was closed with a lid and parafilm. Small holes were inserted into the parafilm so that gas could be exchanged between Petri dish and its surroundings[†].

3.4 Imaging

In this study data was accumulated by different imaging techniques, which are briefly presented in the following.

3.4.1 Microfluidic experiments

For the study of the microfluidic experiments an inverted microscope Olympus IX 81 was used. In order to measure the growth-induced pressure and growth rate of the cells (cf section 4), bright field images were taken. Furthermore, the microscope is equipped with a helium xenon burner (MT20 Olympus) and filter sets (DAPI, CFP, GFP, YFP, RFP) to take epifluorescence images. We took epifluorescent pictures for instance to measure the distribution of glucose in the densely packed growth chamber by flowing fluorescent glucose (2-NBDG [84]) into the chamber (see section 6.2.1) or to study the Whi5-GFP strain (cf section 6.2.5).

3.4.2 Cracks in YPD agar gels

In case of agar crack experiments an inverted Olympus IX 71 microscope and a upright Zeiss AxioZoom.V16 microscope were used to take bright field images of agar cracks in Petri dishes.

---

[*]The inner diameter of the pipette tip is critical in this step. If the diameter is too small the corresponding shear forces acting on the yeast colony are strong enough to rip it apart. To decrease the shear forces the diameter can be increased by cutting off part of conically shaped pipette tip.

[†]This was necessary to counteract the saturation of YPD agar with CO_2, which is produced by *S. cerevisiae* cells when degrading sugars [83].

Chapter 4

Analysis

In the following the analysis methods are presented. If not mentioned otherwise we use MATLAB Version 2012b (The MathWorks, Inc., Natick, MA, United States) for the image processing steps.

4.1 Volume of *S. cerevisiae* colony in agar gel

We completely embedded colonies of *S. cerevisiae* in agar gels as described in section 3.3. Microscopic images were acquired while the colonies were growing and pushing against the surrounding agar gel. To extract the volume of the colony we employ several image processing techniques, which are described in the following text.

Figure 4.1a depicts a *S. cerevisiae* colony of the lab strain S288c embedded in 2% agar gel. In a first image processing step the outline of the colony is extracted by employing the Canny edge detection function[*]. As a result we obtain part of the outline of the colony as shown as the black lines in figure 4.1b. A zoom into a section of the outline, shown in figure 4.1c, reveals that the outline is not completely closed[†].
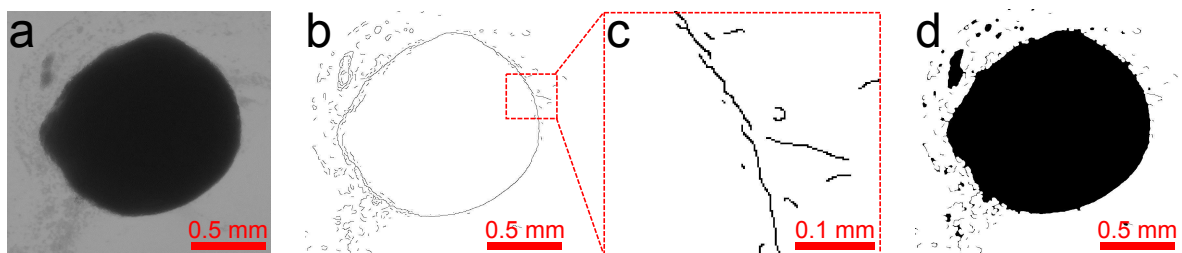

Figure 4.1: Images that illustrate the measurement of the colony volume are shown. a) A microscopic image of a *S. cerevisiae* colony of the S288c lab strain is shown. b) The edge detected image reveals the outline of the colony. c) A zoom into the outline shows that parts of the outline are not closed, the closing of the outline is described in figure 4.2. d) The interior of the outline is filled after closing and the area of the colony is measured. We assume the colony to be spherical and calculate the volume accordingly.

---

[*]Canny edge detection is described in detail in section 4.2.

[†]We require a closed outline to fill the interior of this outline in another processing step and thus obtain an area for the colony.

In order to close these gaps we employ the function imclose to further process the edge detected image. The imclose function performs a morphological close operation (image dilation followed by erosion as described in the following), which is sketched in figure 4.2. Figure 4.2a shows the pixels of a section of the outline. The outline is shown in black, while the remaining pixels are shown in grey. In the first step of the close operation the image is scanned with a structuring element. In figure 4.2b this structuring element is depicted as a red cross (the structuring element in the analysis of the experiment is a disk with a radius of 5 pixels, we chose to show a red cross for convenience). If any pixel of the structuring element overlaps with the outline, the pixel in the center of the structuring element is set to black[‡]. The result of this processing step is depicted in figure 4.2c. In the following step the image is scanned again with the same structuring element as is shown in figure 4.2d. In this step the pixel in the center of the structuring element is set to grey if any part of the structuring element overlaps with a grey pixel[§]. The result of the whole close operation is a closed outline that retains its thickness as shown in figure 4.2e.

After closing of the outline the interior is filled with the imfill function as depicted in figure 4.1d. The area of the colony is calculated as the number of black pixels by means of the regionprops function. We image the colony with transmitted light microscopy in order to extract the area of the colony at the largest dimensions of the colony[¶]. Under the assumption that the colony is roughly spherical, which we checked by eye, we can determine the volume V and radius R of the colony from the area A by

$$V \quad = \quad \frac{4}{3} \sqrt{\frac{A^3}{\pi}} \tag{4.1}$$

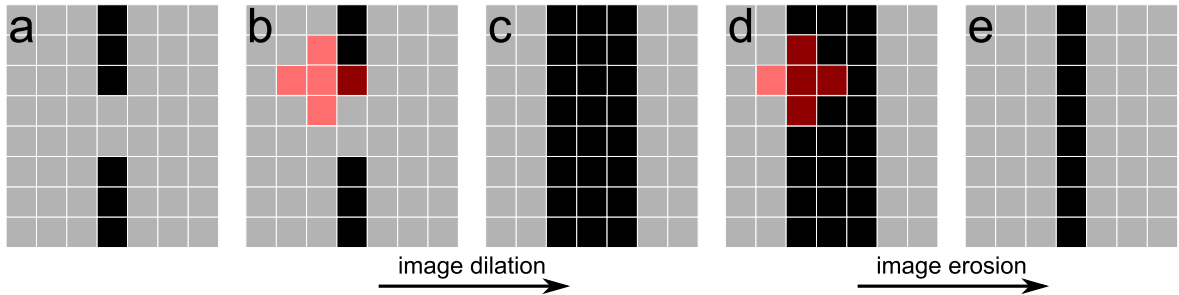$$\text{and } R \quad = \quad \sqrt{\frac{A}{\pi}}. \tag{4.2}$$

Figure 4.2: This scheme shows the steps of the imclose function that is used to close the outline of the colony. a) The black pixels schematically show parts of the outline, while the grey pixels show parts of the image that are not registered as part of the outline. b) The image is scanned with a structuring element shown as the red cross. When a pixel of the structuring element overlaps with a black pixel the pixel in the center of the cross is set to black. The resulting image is shown in c). d) The resulting image is scanned with the same structuring element. If part of the structuring element overlaps with a grey pixel the pixel in the center of the cross is set to grey. The result is depicted in e).

[‡]This part of the close operation is known as image dilation.
[§]This part of the close operation is known as image erosion.
[¶]If the colony is spherical this would be a cut right through the middle of the colony.

4.2   Pressure measurement in the microfluidic device

The growth-induced pressure measurement techniques we developed for the microfluidic experiments all rely on image processing. We either extract the position of a membrane or the width of a channel to obtain the growth-induced pressure.

The membrane (and the channel) need to lie parallel to one of the image axis for our analysis. For some of our experiments we have to rotate the images in a post-processing step accordingly. We use ImageJ [85] for this task, where the rotated image is calculated by a bilinear interpolation. Figure 4.3 shows an example of such an image rotation.

When extracting the membrane position it is necessary to correct the images for drift (especially perpendicular to the membrane). Hence, the drift correction algorithm as described in section 5.4.2 is applied. For the measurement of the channel width a drift correction is not as important since the channel edges will move simultaneously when the image drifts.

After image rotation and drift correction we apply a Canny edge detection algorithm in a region of interest (ROI). The ROI either contains the middle part of the membrane or a section of the channel as indicated in figure 4.4a. The result of the edge detection is a binarized image, in which edges are segregated from the rest. Edges are identified by means of image intensity gradients, where the algorithm allows to chose thresholds for the gradient magnitudes. Gradients above the threshold are identified as edges. Examples of the application of the edge detection on two regions of interest are shown in figures 4.4b, 4.4c and 4.4d, 4.4e respectively. From these binarized images we measure the membrane position or channel width as indicated in figures 4.4c, 4.4e by averaging over the outermost pixels identified as edges.
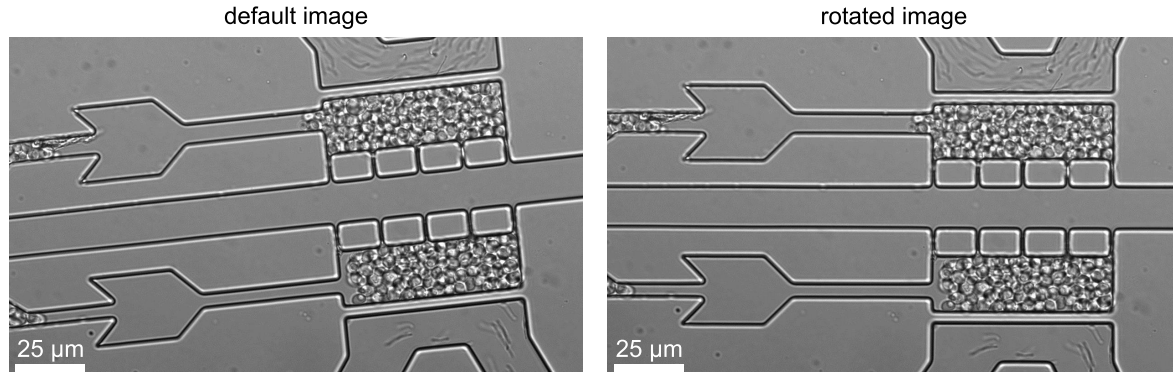

Figure 4.3: An example for an image rotation is displayed. The image is rotated so that the membrane and channel between growth chamber and valve are parallel to the horizontal image axis. This alignment is required for the growth-induced pressure measurement.
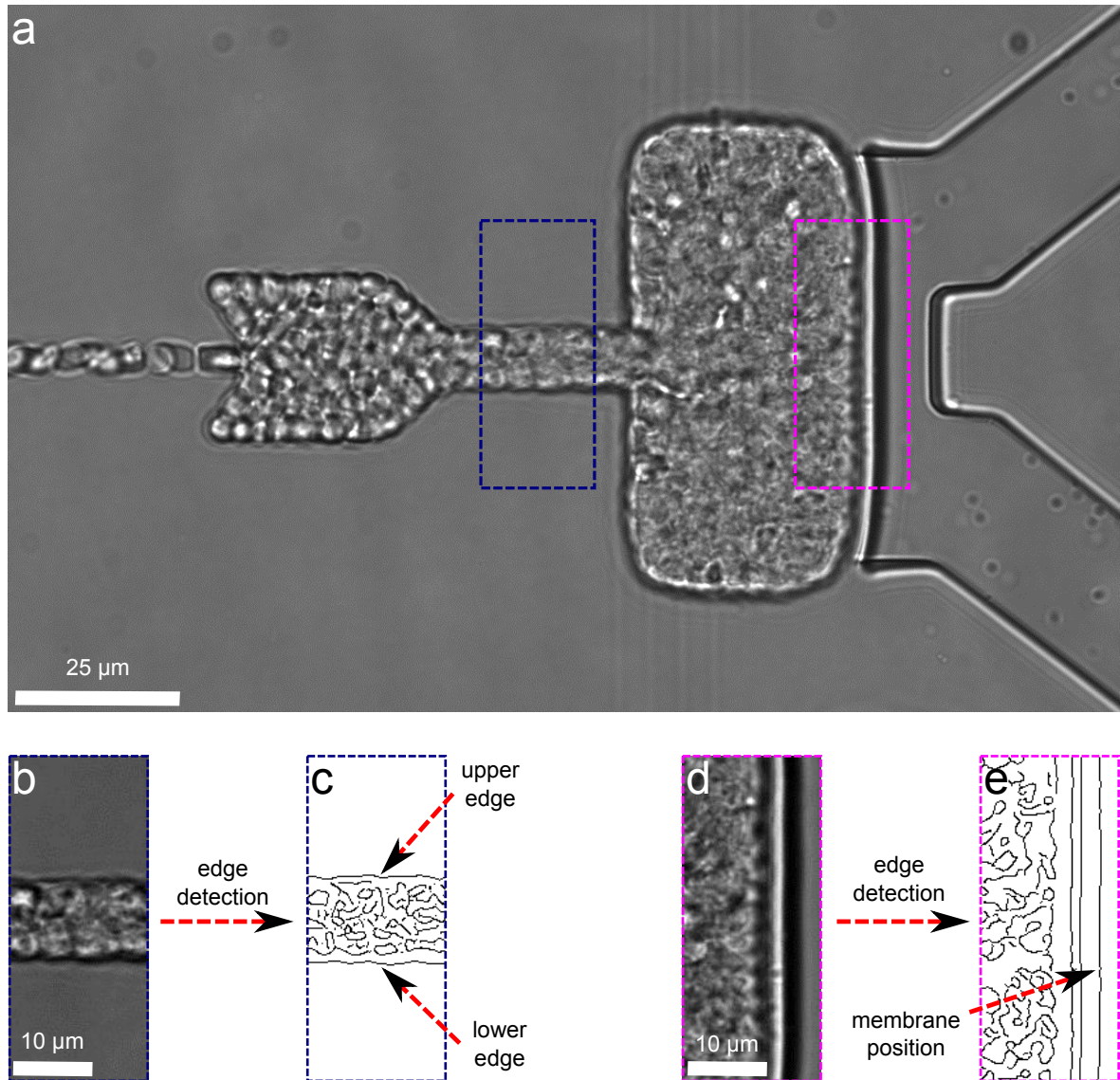
Figure 4.4: Measurement of growth-induced pressure via channel width and membrane displacement. a) Image of microfluidic device, in which the dashed rectangles mark the selection of the regions of interest. b) The region of interest (ROI) in the dashed blue rectangle is shown. c) The image in b) is processed by a canny edge detection algorithm. We measure the width of the channel by automatically averaging over the uppermost and lowermost pixels for each column in the ROI as indicated by the arrows. d) The ROI in the dashed magenta rectangle is shown. e) The image in d) is processed by a Canny edge detection algorithm. We measure the position of the membrane by averaging over the right most pixels for each row in the ROI as indicated by the arrow.

4.3   Particle image velocimetry

Cell flow velocities are measured to characterize the cell flow valves by their degree of confinement (cf section 6.2.1) and to determine the growth rate as a function of the growth-induced pressure (cf section 6.2.4). The bright field images we acquire do not allow for cell segmentation and consequentially a different approach was required to measure cell flow velocities.

We developed a MATLAB program that applies particle image velocimetry (PIV) to achieve this cell flow velocity measurement. The program determines the velocity of the cells as a continuum velocity. The PIV algorithm calculates the correlation between subsequent images. The correlation calculation is similar to the drift correction algorithm (compare section 5.4.2). In the PIV algorithm we use the shift in x and y direction to determine the cell velocity between the two images[‖]. The shift is divided by the time difference between the two images (typically 2-5 min) to obtain the cell velocity. In figure 4.5 we applied our PIV algorithm on two images that show the channel leading from growth chamber to the valve.
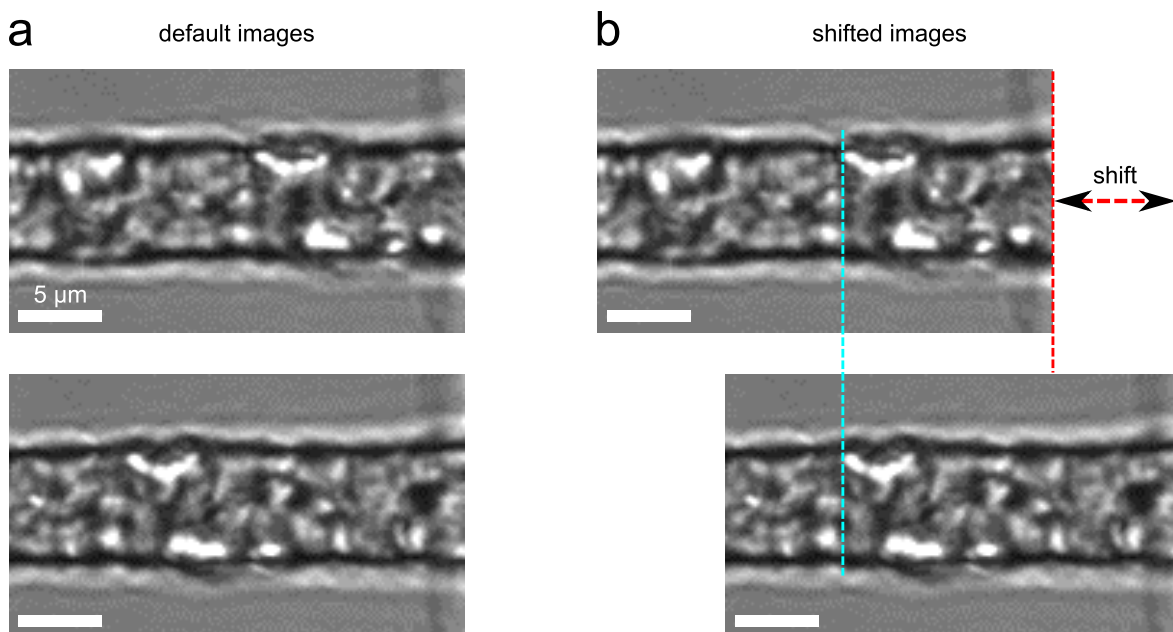

Figure 4.5: Illustration of PIV algorithm. a) The default images are shown. b) The PIV algorithm calculates the shift by taking the maximum of the correlation function into account. The calculated shift is shown by the displacement of the two images.

4.4   Finite element simulations

Finite element simulations are a powerful tool to solve partial differential equations with boundary conditions. The basic principle of the finite element method is that the modeled system is divided into elements of finite size. For each of these elements the partial differential equations are solved numerically. This makes it possible to numerically solve

---

[‖]Notably, the time lapse series are drift-corrected before the application of the PIV algorithm. For the drift correction a region of interest is chosen that does not include any cells to prohibit any bias that might result from cell movement.

differential equations for complex geometries. We use the finite element software Comsol Multiphysics ®(Version 4.0.0.925) to simulate several aspects of our experiments.

4.4.1 Colony embedded in agar gel

In order to extract the growth-induced pressure from the volume of the colony embedded in agar gels, Comsol simulations were conducted.

We mimic the experimental setup (compare section 3.3) by implementing the agar gel as a cylinder with a diameter of 55 mm and a height of 10 mm (see figure 4.6a). The agar gel we use in our experiments has a agar mass percentage of 2%. The Young's modulus of the 2% agar gel is set to 0.2625 MPa in the simulations, as was previously measured by Nayar *et al.* [86]. The agar gel mostly consists of water (compare section 3.2.2) and consequentially the Poisson ratio is close to 0.5 [86]. Notably, a Poisson ratio of exactly 0.5 results in a singularity (indicated by the red box in equation (4.3)) in the stress-strain constitutive relation given by linear elasticity [87]

$$\sigma_{ik} = \frac{E}{1+\nu}\left(\epsilon_{ik} + \frac{\nu}{\boxed{1-2\nu}}\epsilon_{ll}\delta_{ik}\right). \tag{4.3}$$

with σ being the stress tensor, ϵ being the strain tensor, δ_{ik} being the Kronecker delta, E being the Young's modulus and ν being the Poisson ratio[**]. As a test we compare two simulations with different Poisson ratios (0.49 and 0.499) for the agar gel. The results for the two Poisson ratios (0.49 and 0.499) differ less than 0.3% from each other (see figure A.2 in section A.1). This difference does not influence our results in a noticeable way. Since the Comsol simulation might become prone to errors when approaching a Poisson ratio of 0.5 due to the singularity in equation (4.3), we decided to set the Poisson ratio of the simulated agar gel to 0.49.

We implement boundary conditions for the agar gel layer that mimic the experimental setup by fixing the displacement of the agar gel surfaces (in contact with the plastic walls of the Petri dish in the experiments) as is indicated by the surfaces colored in red in figure 4.6b.

In the center of the cylinder a spherical gap with the size of the initial colony[††] is implemented (see figure 4.6c). We simulated growth-induced pressures between 0.0125 and 0.1

[**]The Einstein notation is used in the preceding equation.

[††]For each experiment we conduct one Comsol simulation. The size of the spherical gap is adjusted to the corresponding initial volume of the colony.
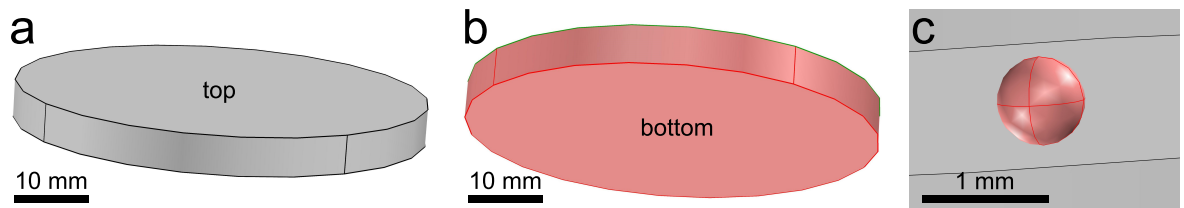

Figure 4.6: The geometries of the comsol model used in simulating the growth of colonie embedded in agar are depicted. a) The agar gel is simulated as a cylinder with a diameter of 55 mm and a height of 10 mm. b) The displacements of the surfaces colored in red are fixed to zero, since these surfaces are in contact with the Petri dish in the experiments. The top of the cylinder can still be displaced. c) In the center of the cylinder a spherical gap is implemented, which represents the colony embedded in agar gel.

MPa that push onto the surface of the spherical gap. The pressures push the surface of the sphere outwards into the agar gel. For each simulated pressure the corresponding volume of the sphere is measured. Figure 4.7a, 4.7b and 4.7c show examples of the displacement of the sphere surface for three different pressures and an initial sphere radius of about 0.7 mm. The volume of the sphere is plotted as a function of the simulated pressure in figure 4.7d together with a linear fit of the data points[‡‡]. We extract the growth-induced pressures in our experiments from these linear fit functions.
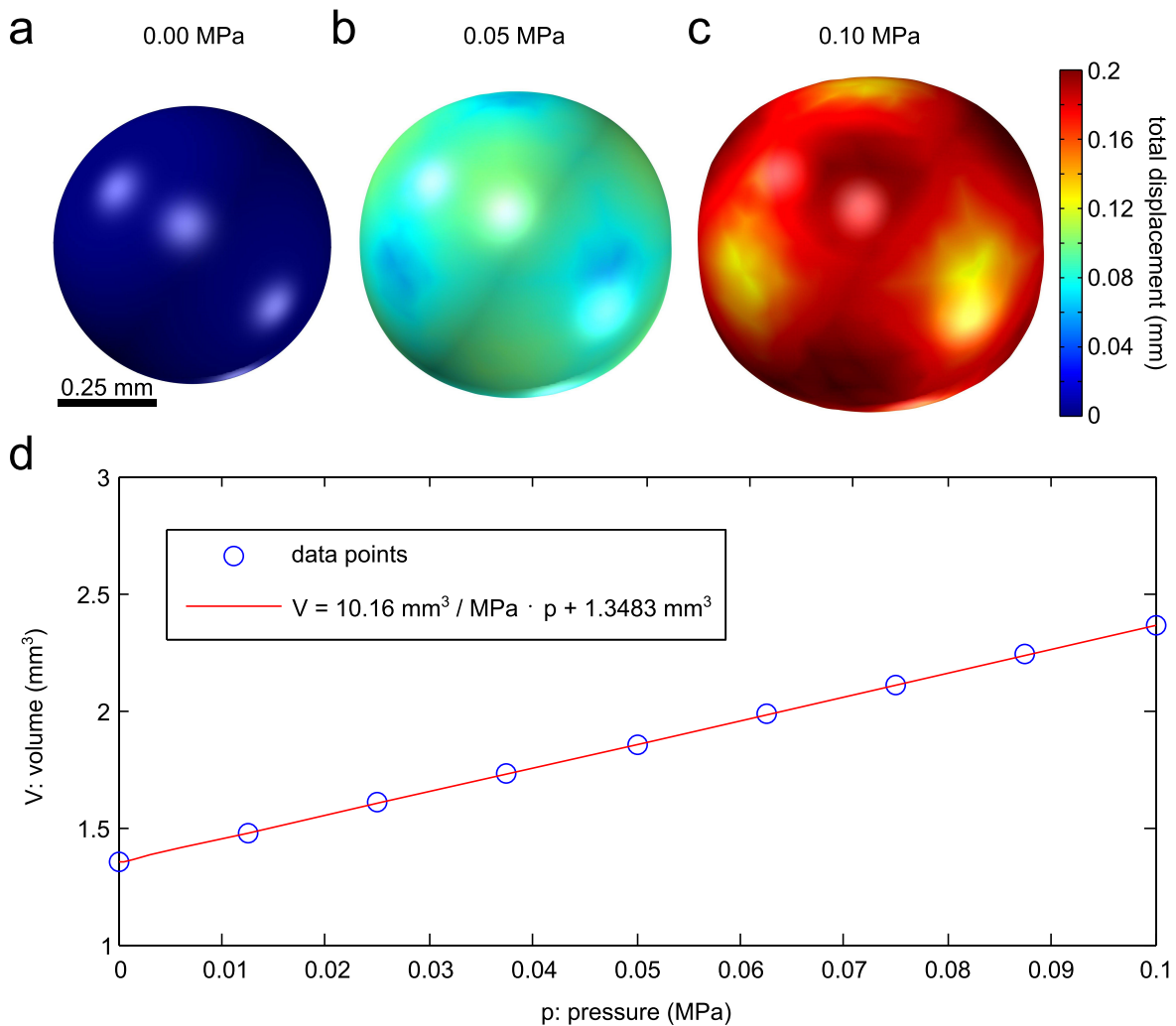

Figure 4.7: The results of a Comsol simulation for an initial colony radius of 0.7 mm are shown. a), b) and c) The total displacement of the colony at different pressures is shown. d) The volume is plotted as a function of pressure together with a linear fit.

[‡‡] The graphs of the remaining Comsol simulations for the different initial sphere volumes are shown in the appendix in section A.1.

4.4.2 Microfluidic device

Deformation of PDMS under pressure

In one of our Comsol simulations we study the deformation of PDMS under pressure. We built the geometry of the growth chamber, control channel, membrane and exit channel with the model builder of Comsol (shown from the bottom view in figure 4.8).

In order to simulate the displacement of the membrane we define boundary conditions for the surfaces in the model. The bottom surface (colored red in figure 4.8) that corresponds to the part of the device that is bonded to glass is set to have a fixed position. This assumption is reasonable since the glass will be hardly displaced at the simulated pressures, which are in the order of 0.1 to 1.0 MPa, while the Young's modulus of borosilicate glass[§§] is about 63 GPa [88]. We simulate pressures ranging from 0 to 1.1 MPa with an increment of 0.1 MPa onto all surfaces belonging to the growth chamber and exit channel. Furthermore, we conducted simulations for different Young's moduli (1.6, 1.8, 2.0, 2.2, 2.4 MPa), which lie in the range of what we expect for the stiffness of our devices [70]. The Poisson's ratio is set to 0.45 as has previously been used by others [89]. Figures 4.9a, 4.9b and 4.9c show the displacement of the membrane for a Young's modulus of $E = 2.0$ MPa at different pressures. The color bar

---

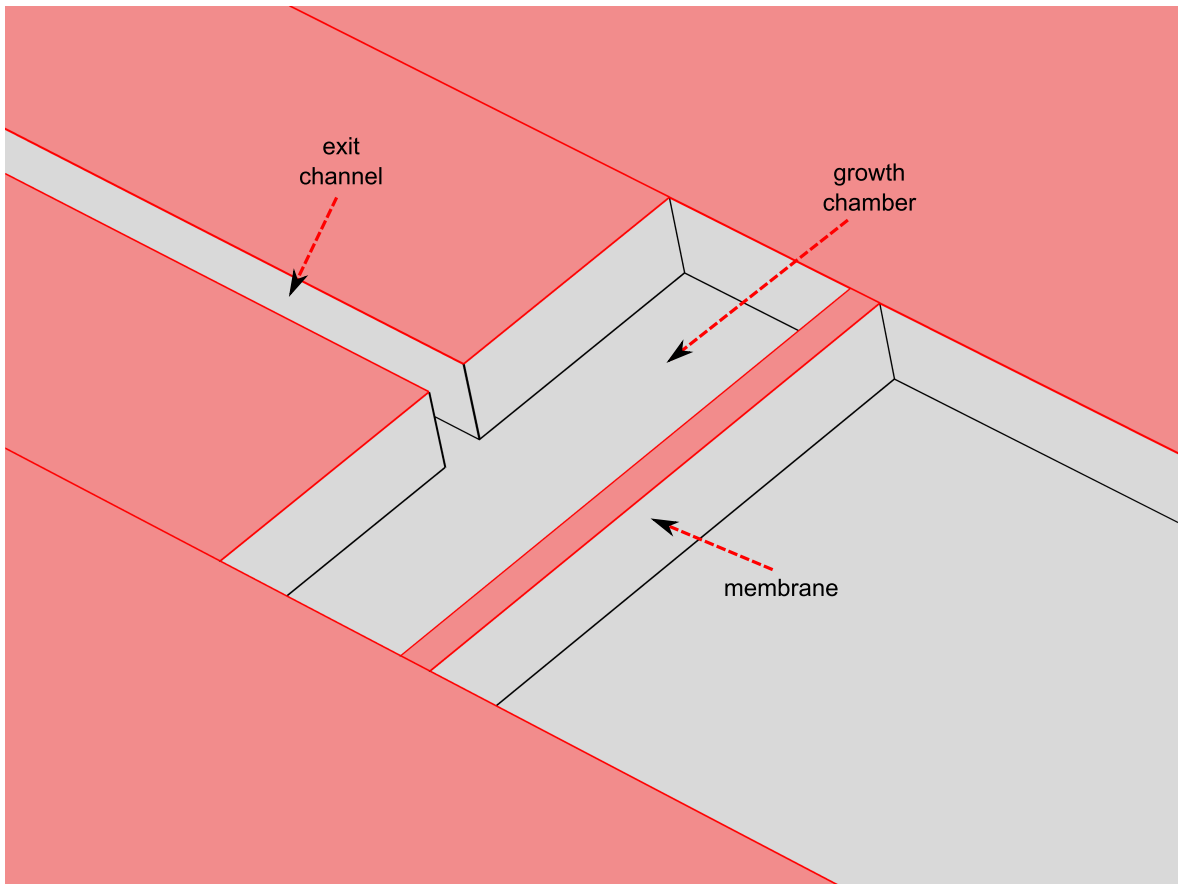[§§]Borosilicate glass is the material of the here used glass slides.

Figure 4.8: A part of the geometry we built in Comsol is shown. The bottom surface bound to glass (in the experiments) is colored in red.

represents displacement values of the membrane normal to its default surface. We measure the maximal membrane displacement for various values of the simulated pressure divided by the Young's modulus p/E and plot the results in figure 4.9d. The data points collapse for the different Young's moduli and the functional relationship between displacement and pressure is linear over the whole simulated pressure range.

Furthermore, we extract the width of the exit channel as a function of pressure divided by the Young's modulus of PDMS. Figure 4.10a, 4.10b and 4.10c show the deformation of the channel¶¶ at different pressures for a Young's modulus of 2 MPa, while the channel width is plotted as a function of p/E in figure 4.10d. For plots that relate the cross-section of the exit channel with pressure and maximal channel width see section A.1. The results from these plots are required for the cell flow measurements.

The growth chamber volume gives a measure of how many cells are present in the device provided cell density does not change. Since the growth chamber volume increases with growth-induced pressure, we have to take this relation into account when calculating the growth rate as a function of time (compare section 6.2.4). Figure 4.11a, 4.11b and 4.11c show the growth chamber at different simulated pressure values. The volume increases noticeably with pressure. We measure the volume of the growth chamber for pressures between 0.1 and 1.1 MPa and plot the result in figure 4.11d. The linear fit indicates that the volume increases linearly with pressure.

Nutrient supply

In another set of Comsol simulations we probed the distribution of nutrients in our device. In a first simulation we consider the diffusion of nutrients without flow in the growth chamber of our device. The concentration of nutrients in the nutrient channels is fixed to a constant value of C_0. Furthermore, we implement the consumption of nutrients by the cells as described in section 6.2.1. This consumption can be mimicked in Comsol by adding a reaction term to the model. The reaction term describes at which rate a chemical is transformed. This is analog to a consumption rate since in both cases the concentration of the nutrients is diminished at a defined rate (see figure 4.12a).

In a second nutrient concentration simulation we first derive the velocity field in the growth chamber from the experimental boundary conditions (see figure 4.12b). The inflow in the nutrient channels on one side of the growth chamber is set to 0.2 nl/s while the outflow on the opposite side of the growth chamber is set to the same value. The resulting velocity field is taken into account when the distribution of nutrients is simulated. The results of the nutrient distribution are presented in section 6.2.1.

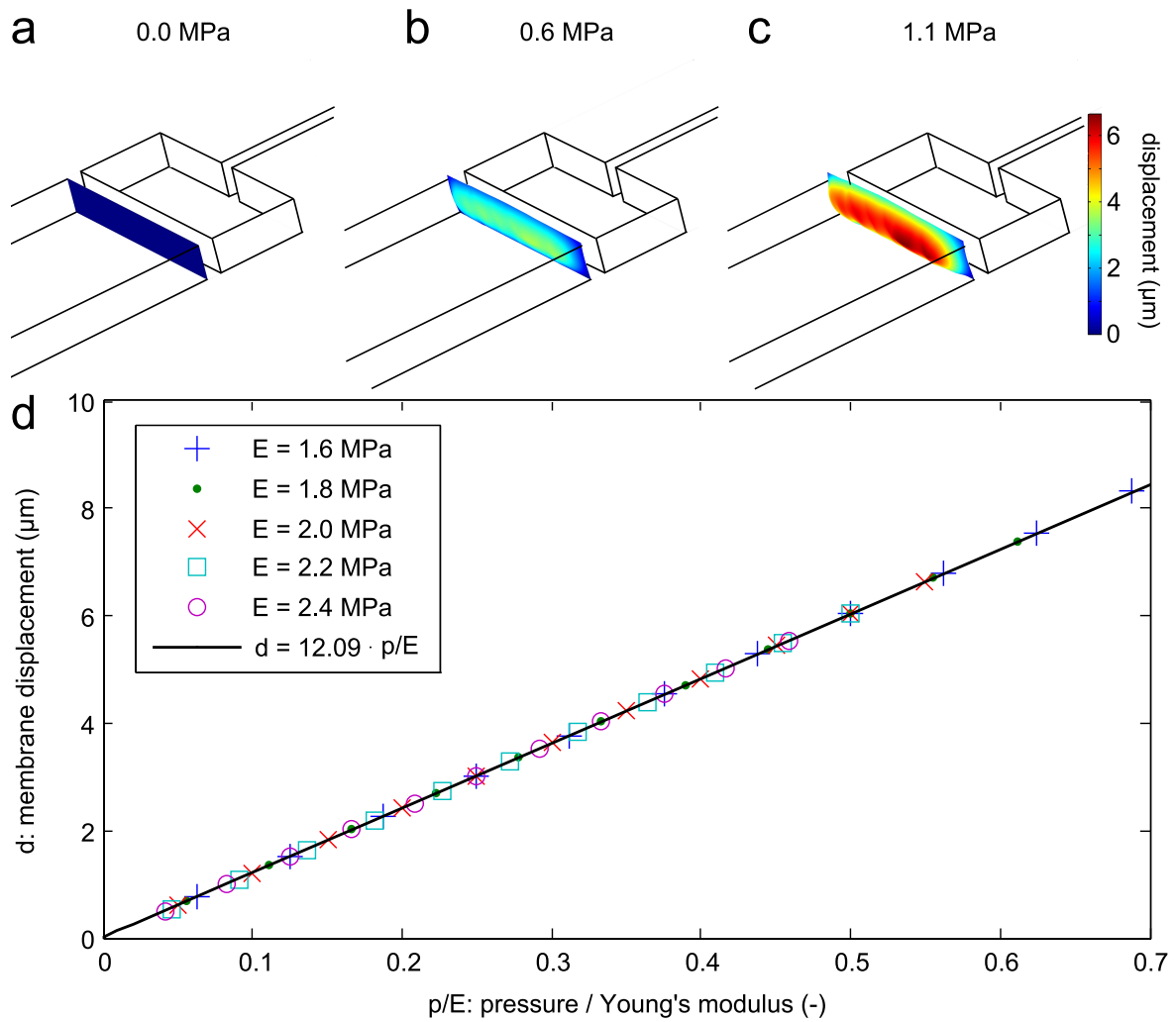¶¶The color bar represents the total displacement values derived by Comsol.

Figure 4.9: Results of the finite element simulation of the membrane displacement. a,b,c) The displacement of the membrane is shown for three different pressures for a Young's modulus of 2 MPa. The color bar represents the displacement of the membrane perpendicular to its default surface. d) The maximal displacement of the membrane is measured for different values of pressure divided by the Young's modulus p/E. We extract the linear dependency of the displacement as a function of p/E from these data.
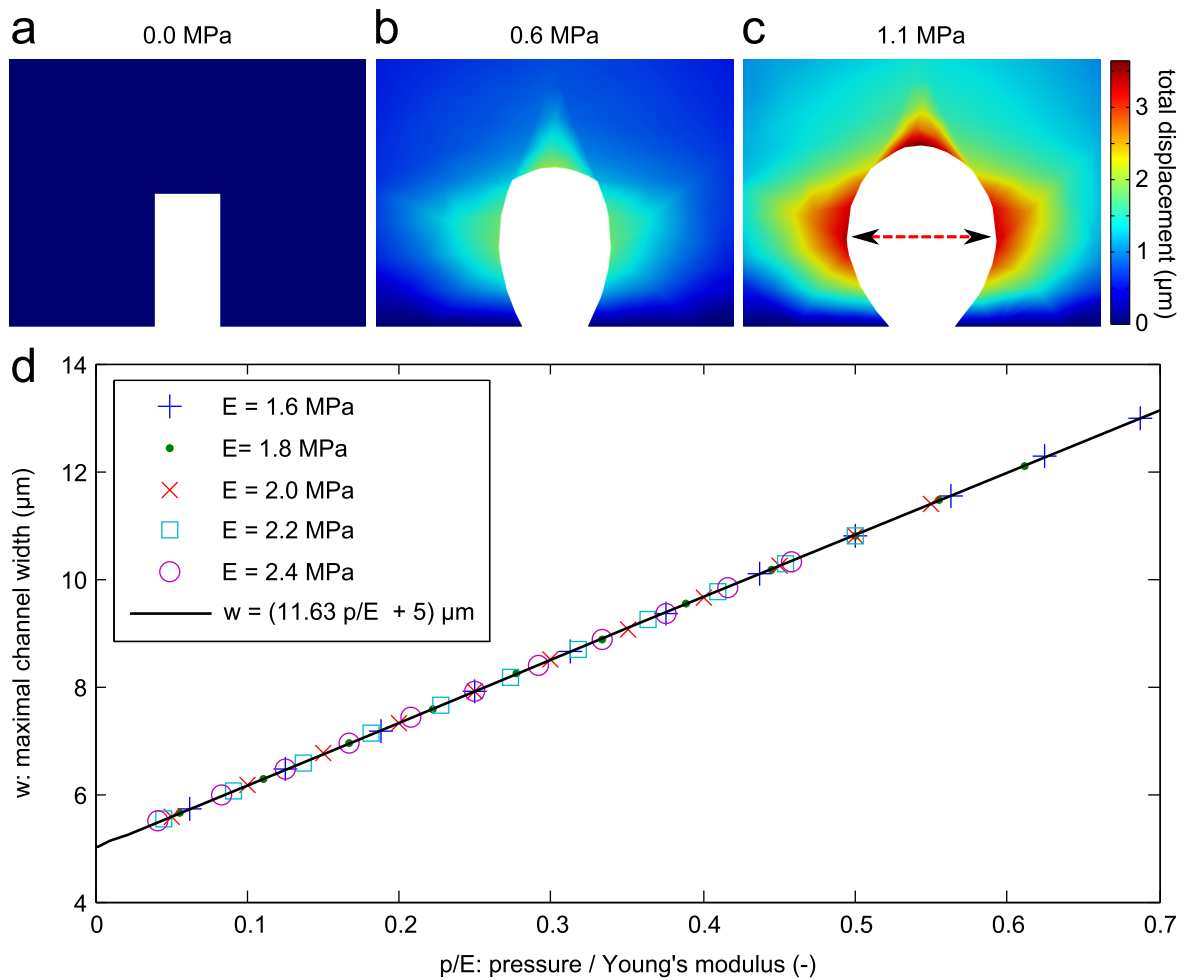
Figure 4.10: Results of the finite element simulation of the channel width. a,b,c) The deformation of the channel is shown for three different pressures for a Young's modulus of 2 MPa. The color bar represents the total displacement. d) The maximal channel width is measured for different values of pressure divided by the Young's modulus p/E. We extract the linear dependency of the displacement as a function of p/E from these data.
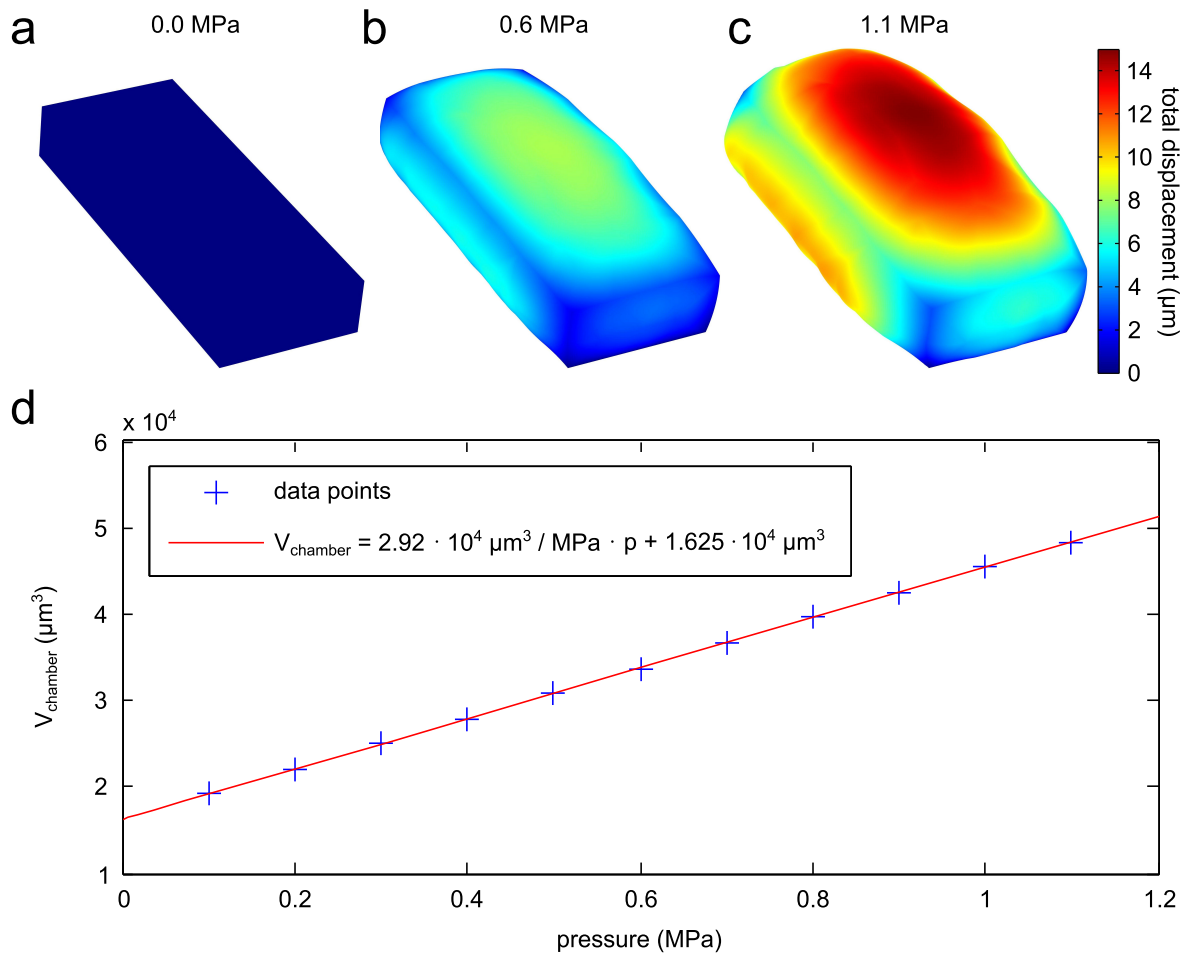
Figure 4.11: a,b,c) Comsol simulation of the growth chamber volume at different pressures with color coded total displacement. d) The growth chamber volume is plotted as a function of pressure for a Young's modulus of 1.7 MPa together with a linear fit through the data points.
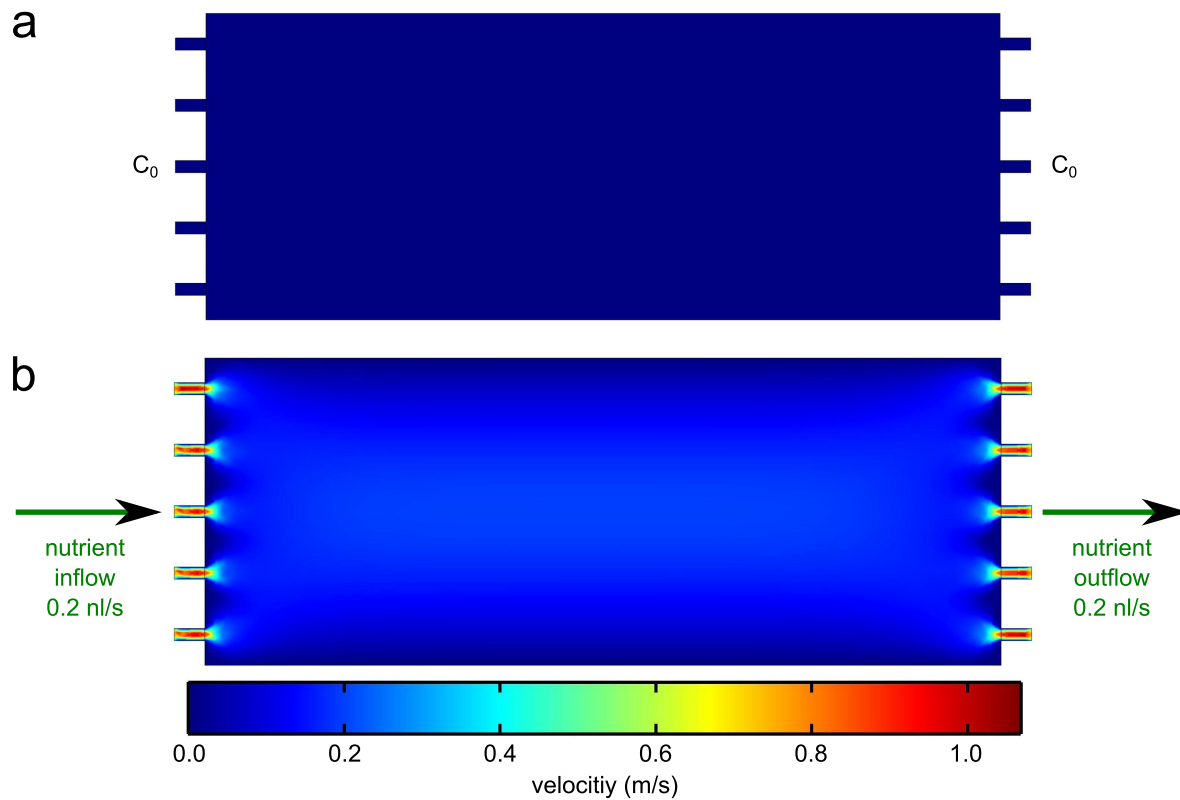
Figure 4.12: Velocity fields of the two Comsol simulations that were conducted to measure the concentration of nutrients in the growth chamber. a) In this case only diffusion is considered, so that the velocity field is zero everywhere. The concentration in all nutrient channels is set to C_0. b) The velocity field in the growth chamber is derived from boundary conditions in this second case. Liquid is flowing into the growth chamber from the left at a flow rate of 0.2 nl/s and flowing out at the opposite side at the same flow rate. The color code represents the magnitude of the velocity.

4.5 Cell avalanche statistics

4.5.1 Data extraction

We observe intermittent behaviors of the pressure curves in some of our microfluidic experiments. We determined that large drops in pressure result from the dissolution of cell clots followed by cell avalanches (cf section 6.2.3). Here we describe the extraction of the pressure drops Δp and survival times of the cell clots τ from the data.

The pressure curves are discrete functions of time $p(t_i)$ with t_i the time corresponding to the i-th data point. In a first step we calculate the moving average for three time points of the pressure curve to smooth out noise from the pressure values by

$$p_{\text{smooth}}(t_i) = \frac{1}{3} \sum_{j=-1}^{1} p(t_{i+j}).$$ (4.4)

In the next step we scan the data to find drops in pressure. We identify the local pressure maximum at time t_k and local pressure minimum at time t_l of a given pressure drop. We calculate the pressure drop as

$$\Delta p_{\text{test}} = p_{\text{smooth}}(t_k) - p_{\text{smooth}}(t_l) \text{ with } t_k < t_l.$$ (4.5)

If Δp_{test} is greater or equal to a threshold of 0.02 MPa we detect an avalanche. In order to give values for the pressure drop we use the raw data:

$$\Delta p = p(t_{k'}) - p(t_{l'})$$ (4.6)

with $t_{k'} \in t_{k-1}, t_k, t_{k+1}$ and $t_{l'} \in t_{l-1}, t_l, t_{l+1}$. Due to the moving average calculation it is possible that the local extrema shift by ± 1 time steps. As a consequence we have to search for the local maximum and minimum in pressure in ± 1 neighborhoods.

In conclusion we use a smoothed pressure curve to identify cell avalanches but we calculate the actual pressure drops from the raw data. This methods helps to avoid artificial pressure drops that result from noise. The smoothed pressure drops are always smaller than the actual drops. This is a bias we circumvent by taking the raw data into account when having already identified a cell avalanche.

The survival times of clots τ are given as the time difference of two subsequent cell avalanches. We define τ as the time difference between the local pressure minimum of a first avalanche and local pressure maximum of the subsequent avalanche.

4.5.2 Survival function

We employ survival functions to further analyze the distributions of pressure drops Δp and survival times τ of the cell avalanche statistics. Survival functions are a convenient tool to compare data sets with different experimental conditions. The survival function for a probability density function (pdf) $f(t)$ is defined as

$$S(T \geq \tau) = \int_{\tau}^{\infty} f(t) \, dt$$ (4.7)

with $S(T \geq \tau)$ being the probability to find events T in the data that are greater or equal to τ. In figure 4.13 we plotted the probability density function of a Gaussian distribution

(variance of 2). The survival function for $\tau = 0.5$ is equal to the shaded area beneath the pdf.
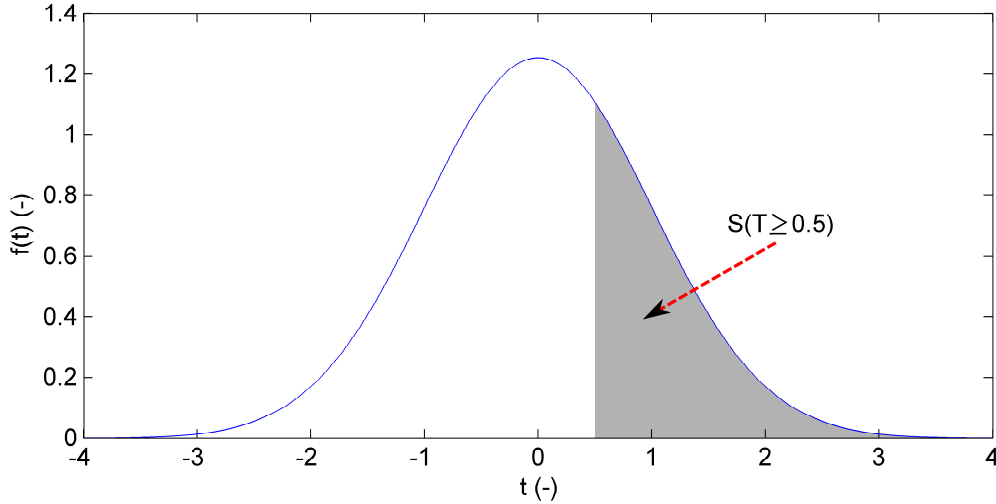

Figure 4.13: The blue curve is the probability density function of a Gaussian distribution with a variance of 2. The shaded grey area is equal to the survival function $S(T \geq \tau)$ for $\tau = 0.5$.

We are especially interested in the tails of the survival functions since it has been shown for other intermittent flows that the corresponding tails show power-law decay behavior [58, 90, 91].

We assume that the pdf $f(t)$ exhibits a power-law decay for $t \geq \tau_{\min}$

$$f(t) = \begin{cases} g(t) & \text{for } t < \tau_{\min} \\ \beta \cdot t^{-\alpha} & \text{for } t \geq \tau_{\min} \end{cases} \tag{4.8}$$

with $g(t)$ some pdf and β the normalization constant. A power-law decay exponent of $\alpha > 1$ is required to satisfy the normalization condition

$$\int_{-\infty}^{\infty} f(t) \, dt \overset{!}{=} 1, \tag{4.9}$$

since for $\alpha \leq 1$ the integral does not converge. The survival function for $\tau \geq \tau_{\min}$ is given as

$$S(T \geq \tau) \quad = \quad \int_{\tau}^{\infty} f(t) \, dt = \int_{\tau}^{\infty} \beta \cdot t^{-\alpha} \, dt \tag{4.10}$$

$$= \quad \left[\frac{\beta}{-\alpha + 1} \, t^{-\alpha+1} \right]_{\tau}^{\infty} \tag{4.11}$$

$$= \quad \frac{\beta}{\alpha - 1} \, \tau^{-\alpha+1} \propto \tau^{-\alpha+1}. \tag{4.12}$$

In words, if the pdf has a power-law tail that decays as $t^{-\alpha}$, the survival functions decays as $\tau^{-\alpha+1}$.

Chapter 5

Microfluidic setup

The microfluidic device, employed in most of the experiments described in this thesis, has been developed based on previous work of Nils Podewitz and Dr. Hedvika Toncrova. Here, the different steps in device development as performed by the author of this thesis are detailed.

5.1 Design

5.1.1 Version I

We present here the device previously designed by Nils Podewitz and Dr. Hedvika Toncrova. It is a single layered device with structures having a height of approximately 10 µm. The experiments conducted with this version of the device were performed by Dr. Hedvika Toncrova and data analysis was conducted by the author of this thesis.

In figure 5.1a an overview of the overall structures of the device is shown. The design for the various inlets is based on a device previously developed by Rowat *et al.* [92]. The filters adjacent to the inlets prevent large dust particles from entering and obstructing the channels. The loading of cells and the supply with nutrients are provided separately by different inlets. Channels connected to the corresponding inlets meet at a junction (figure 5.1b). When the flow from the cell inlet is switched off and the nutrient flow is maintained, cells upstream from the junction are transported back to the cell inlet (see Supporting Information in [92]). This backflow helps to prevent cells from entering the device after it had already been sufficiently loaded. The cells everywhere in the device increase exponentially in number [22]. Consequentially, if the yeast cells are not hindered from entering the device from the inlet after loading all channels are filled with cells after some time.

The control channels, which are essential for the growth-induced pressure measurement (figure 5.1a), can be filled with distilled water via their inlets. After they are completely filled the outlets are closed.

Figure 5.2 shows a zoom into the functional parts of the device, which are located just downstream from the junction in figure 5.1b. This is also the region of the device of which the microscopic pictures are taken. Several components of the device which are crucial to our experiments are displayed. The two growth chambers act as defined volumes, in which cell populations grow. In figure 5.3 a growth chamber filled with different cell densities is shown. The volume of the growth chambers was chosen such that it can contain between 100 and 200 cells depending on cell size and packing fraction. The width of the channel connected to the growth chamber is as wide as one average cell diameter (the average diameter of a
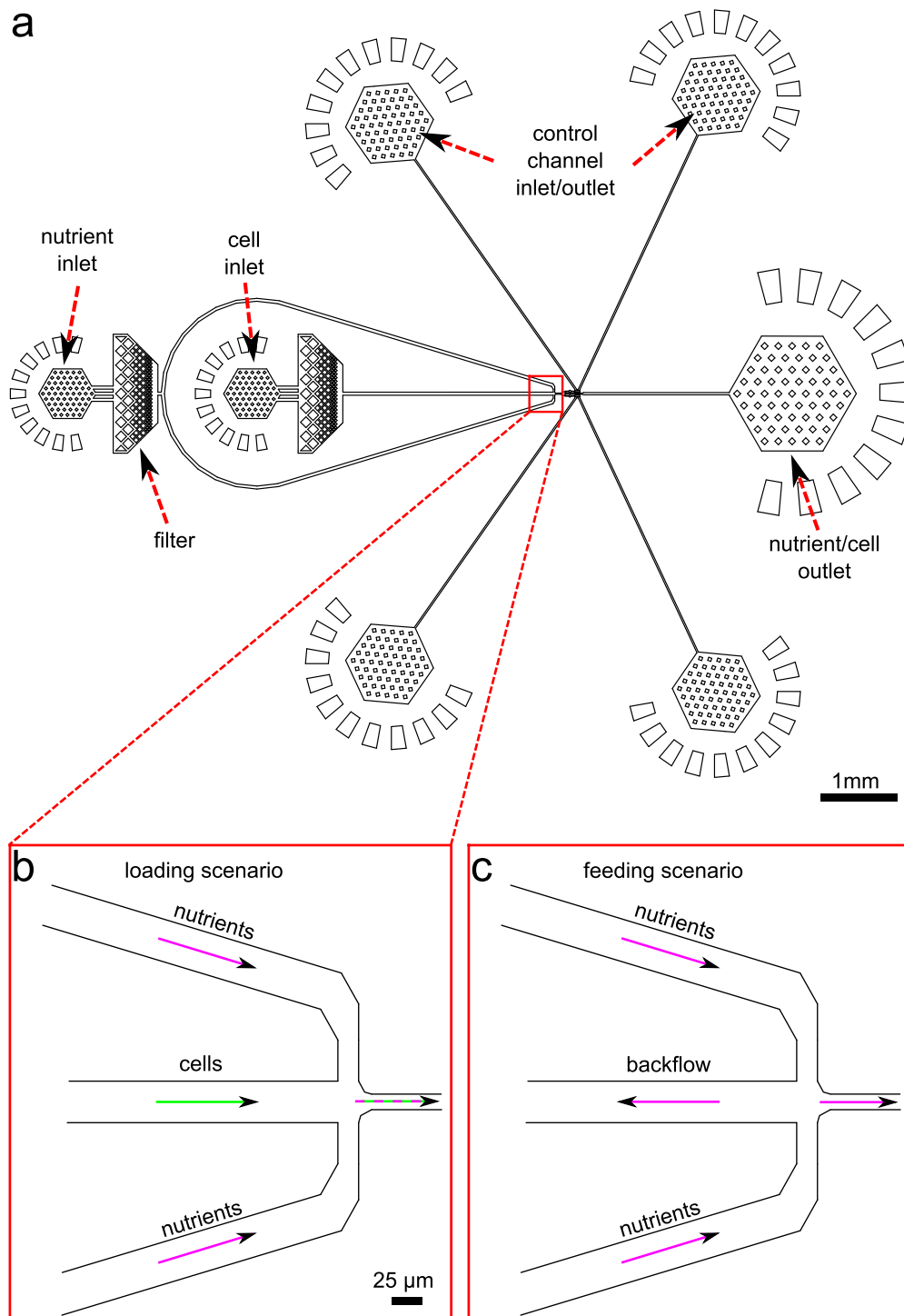
Figure 5.1: Structures of the Version I device are detailed. a) An overview of the structures is shown. The design for the inlets and filters were adapted from [92]. b) A zoom in onto the junction at which nutrient medium and liquid cell suspension flows intersect. c) When the liquid cell suspension flow is switched off, a backflow of nutrients in the direction of the cell inlet helps to keep cells from entering the whole device when proliferating.
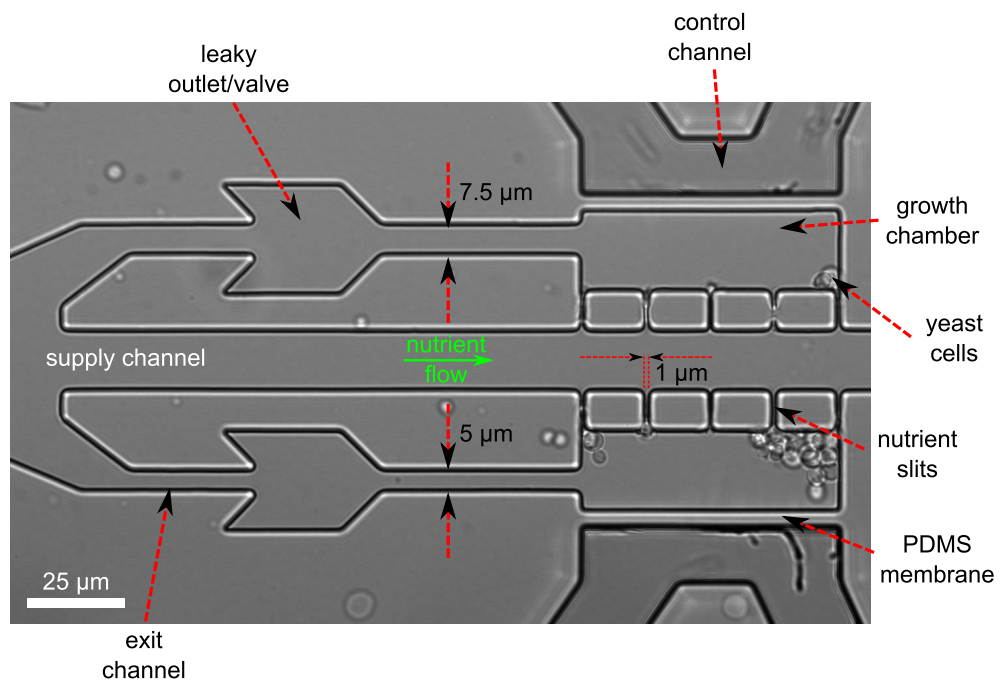
Figure 5.2: Image showing the section of the Version I device, in which the experiments are conducted. The growth chamber is the compartment, in which the growth-induced pressure is measured by detecting the displacement of a PDMS membrane separating the growth chamber from a control channel. The leaky valves promote the formation of cell clots that result in a increase of growth-induced pressure. The bottom exit channel is 5 µm wide, while the top exit channel has a width of 7.5 µm. Nutrients are supplied to the cells via a supply channel and nutrient slits that are 1 µm wide.
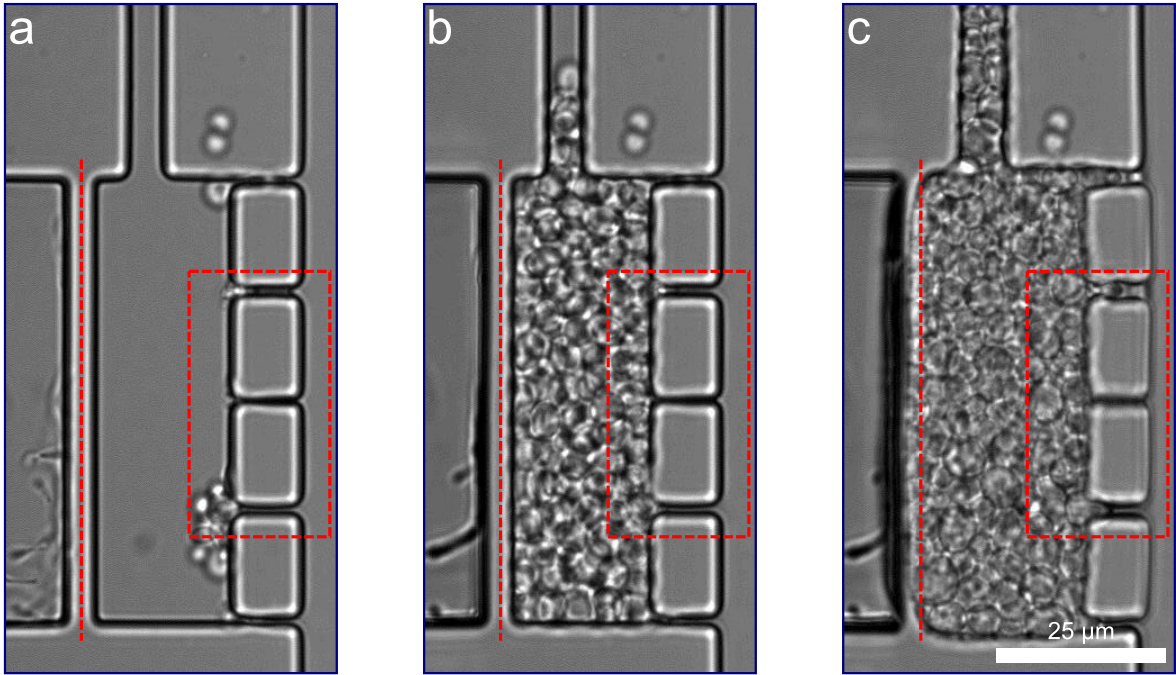
Figure 5.3: Growth chamber of the device filled with different cell densities: a) Cells (*S. cerevisiae*) were loaded into the growth chamber. b) The cells have proliferated for about 7.6 hours and the growth chamber is filled with cells, but the growth-induced pressure is still zero. c) Cells have proliferated for another 7.6 hours. The growth-induced pressure has noticeably increased, which can be seen by the deformation of the surrounding PDMS walls.

S. cerevisiae cell is approximately 5 µm [93]). The growth chamber is initially loaded with a few cells as shown in figure 5.3a. The cells proliferate, filling the growth chamber (figure 5.3b). At this point the growth-induced pressure is still zero and no deformation of the PDMS is apparent. In figure 5.3c, the build-up of growth-induced pressure by the confined cells is evident as seen by the deformation of the PDMS. Notably, the deformation of the membrane between the control channel and the growth chamber, marked by the dashed line, and the deformation of the rectangles between the nutrient slits, indicated by the red, dashed rectangle, are obvious.

Another essential component of the device is the cell outlet. We designed different outlets in order to confine yeast populations in the growth chambers. In this version of the device three different designs for outlets have been implemented. They differ in their opening angle (45°, 90° and 135°) towards the exit channel (see figure 5.4). Yeast populations are partially confined by these outlets. Several cells are pushed towards the exit at the same time due to the broadening and subsequent narrowing of the exit channel. This leads to a clogging of the outlets, which depends on the exit channel width (see section 6.2.2). Once the mechanical pressure increases due to forces developed by cell growth, the cells and the surrounding PDMS deforms further. These forces can lead to breaking of the cell clot and a subsequent pressure decrease until another cell clot forms. This process gives the outlets a leaky nature. Since these outlets essentially act as valves when we consider the cellular populations as fluids we term them leaky valves.

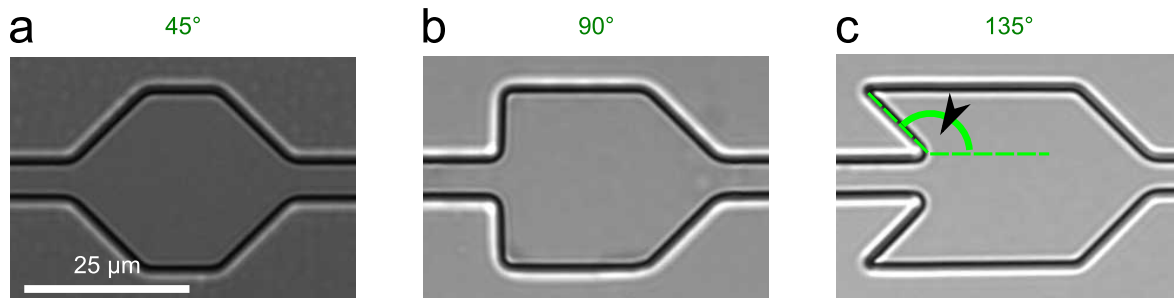In between the two growth chambers a supply channel is implemented (figure 5.2). After

Figure 5.4: The designs of the three leaky outlets/valves are shown. They differ in their opening angle towards the exit channel.

loading the growth chambers with cells, a continuous flow of 1 nl/s of nutrient medium is applied to this supply channel. Nutrients enter the growth chamber by flow and diffusion through the nutrient slits. These slits are 1 µm wide so that a *S. cerevisiae* cell with a minimal diameter of about 3.4 µm [15] cannot simply escape through them. The nutrient slits are also necessary for loading of the growth chambers with cells, since a portion of the liquid cell suspension flows into the growth chamber, while cells are trapped at the nutrient slits.

The main application of our device is the measurement of growth-induced pressures exerted by cell population under confinement. In order to accomplish this task we rely on the deformability of PDMS at the pressure range we are interested in. As already mentioned in section 3.1.2 PDMS[*] stiffness can be tuned in the order of 0.1 - 1 MPa. The maximal growth-induced pressure that we measure for a cell population is about 1.2 MPa (section 6.2.2). When taking this growth-induced pressure and the Young's modulus range of PDMS into account we can assume that deformations due to growth-induced pressure in PDMS are noticeable. This is also apparent in figure 5.3, where the growth chamber deforms under the pressure the cell population exerts. It is clear that the stronger the deformation is, the more accurate the pressure measurement is. For instance a PDMS membrane with a width of 4 µm deforms more than a bloc of 1 mm at a given pressure. We exploit this by implementing control channels that are separated from the growth chambers by 4 µm thick membranes. The deformation of this membrane can be observed in figure 5.3. In the first two images of figure 5.3a, 5.3b the growth-induced pressure is zero whereas it increases to a value in the order of 0.1 MPa in figure 5.3c. This pressure results in a well deformed membrane.

5.2 Pressure measurement

The growth-induced pressure measurement method relies on the displacement of the PDMS membrane between growth chamber and control channel. The displacement of the membrane is balanced by adjusting the hydrostatic pressure inside of the control channel. The sketches in figure 5.5 illustrate the measurement technique. Figure 5.5a shows the default situation, in which the pressures in the growth chamber and control channel are zero[†]. Then, the pressure in the growth chamber in figure 5.5b rises to about 0.4 MPa, which is higher as the pressure in the control channel resulting in a displaced membrane. The hydrostatic pressure in the control

---

[*]Sylgard 184 silicone elastomer kit, Dow Corning Corporation MI United States

[†]We only consider effective pressures defined as $p_{\text{eff}} = p - p_{\text{atmosphere}}$
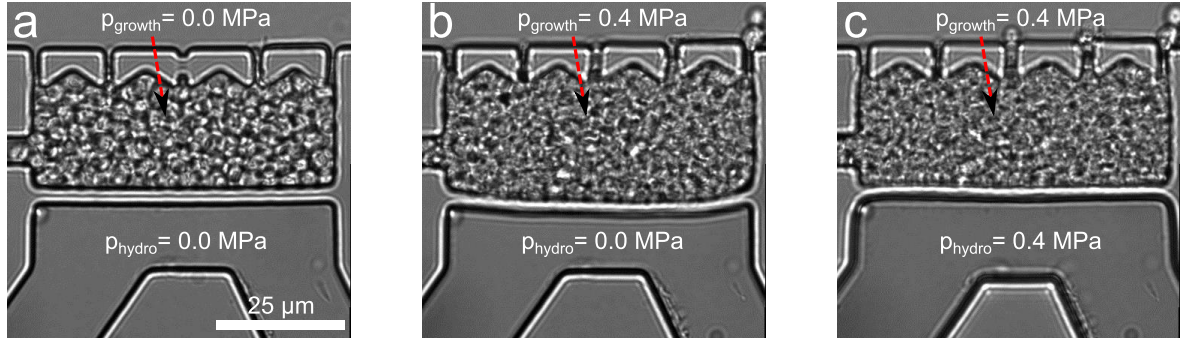
Figure 5.5: Microscopic images illustrate the balancing of the membrane between growth chamber and control channel. The given values are the growth-induced pressures in the population. a) The default situation is shown, in which the pressures in growth chamber and control channel are zero. b) The growth-induced pressure in the growth chamber has increased while the hydrostatic pressure in the control channel is still zero, which results in a displaced membrane. c) The hydrostatic pressure in the control channel has been increased to recover the initial position of the membrane. In this case the two pressures are equal.

channel is increased accordingly (figure 5.5c) to match the pressure in the growth chamber. In this case the membrane assumes its default position, so that the hydrostatic pressure in the control channel is equal to the growth-induced pressure in the growth chamber. In the experiments in which we directly measure the growth-induced pressure, the position of the membrane is balanced every one to two minutes. In fact, we did not wait until the membrane deforms as strongly as shown in 5.5b, before we increase the hydrostatic pressure. We would otherwise artificially exert a force onto the cell population by displacing the membrane by such a large amount.

In the experiments conducted by Dr. Hedvika Toncrova the hydrostatic pressure in the control channel was changed by means of a syringe (1 ml, Terumo Medical Corporation, New Jersey, USA) filled with 1 ml air in contact with the distilled water reservoir in the control channel. By compressing the air in the syringe the hydrostatic pressure in the water reservoir increased. The ideal gas law was assumed to hold true in this case

$$pV = nRT, \tag{5.1}$$

with pressure p, air volume V, amount of moles n, ideal gas constant R and temperature T. For an isothermal process at constant amount of moles a change in volume from V_1 at atmospheric pressure p_1 to V_2 results in a pressure of

$$p_2 = p_1 \frac{V_1}{V_2}. \tag{5.2}$$

We are only interested in the effective pressure p_{eff}, that is the pressure p_2 subtracted by the atmospheric pressure p_1

$$p_{\text{eff}} = p_1 \left(\frac{V_1}{V_2} - 1 \right) \tag{5.3}$$

$$\text{or } V_2 = V_1 \frac{p_1}{p_1 + p_{\text{eff}}}. \tag{5.4}$$

This method of measuring the hydrostatic pressure is prone to errors especially for high pressure values. This can be visualized by extracting values from V_2 as function of p_{eff} (see figure 5.6). For instance the volume V_2 changes to achieve effective pressures of 0.35 MPa and 0.4 MPa respectively are

$$
\begin{aligned}
V_2(p_{\text{eff}=0.35\,\text{MPa}}) &= 222 \text{ µl} & (5.5) \\
V_2(p_{\text{eff}=0.4\,\text{MPa}}) &\approx 200 \text{ µl.} & (5.6)
\end{aligned}
$$

The error with which the initial volume V_1 ml is set to 1 ml is already in the order of 1% (10 µl), so that pressures above 0.35 MPa can not be measured with sufficient precision. One can easily see in figure 5.6 by the decrease in slope of the curve that pressure measurements with this method become increasingly inaccurate at even higher pressure values (> 0.4 MPa). Over the course of this project we developed more sophisticated techniques to measure the hydrostatic pressure that allow us to also resolve high pressure ranges (see section 5.4).
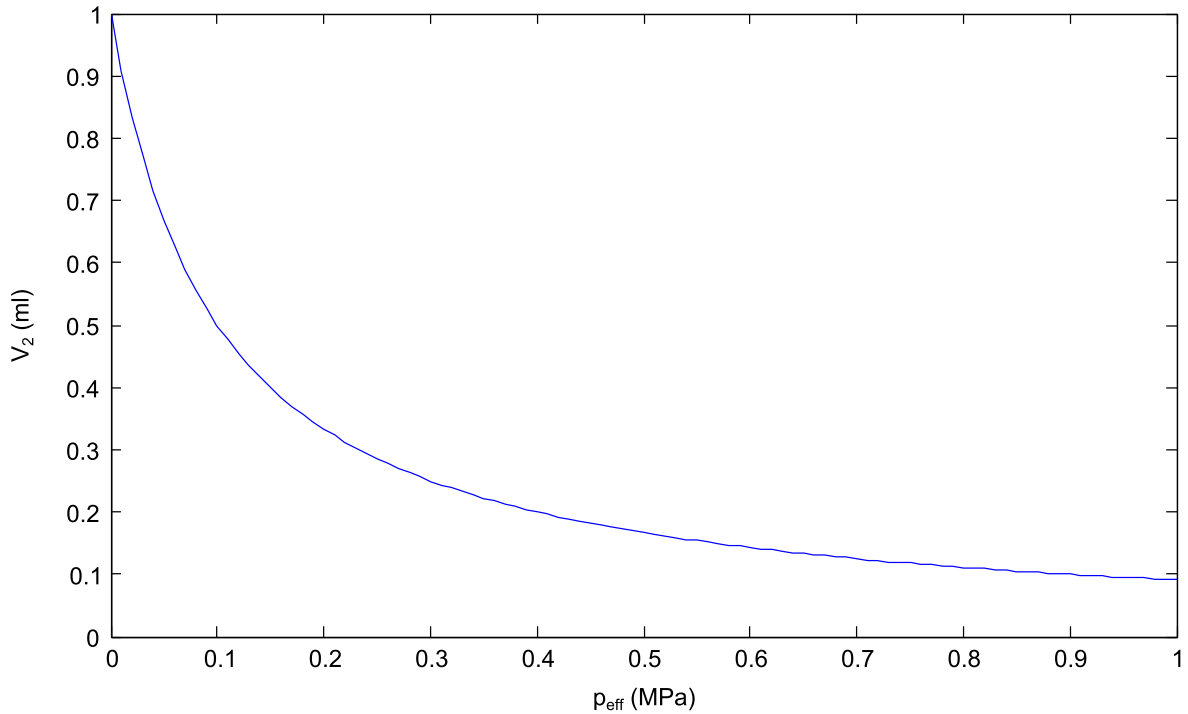

Figure 5.6: The volume of the air reservoir in the syringe is plotted as function of the effective hydrostatic pressure p_{eff} for an initial volume $V_1 = 1$ ml and initial atmospheric pressure $p_1 = 0.1$ MPa.

5.3 Development of experimental design

In this section changes in the design of the device are presented to guide the reader through the development process.

5.3.1 Valves

The valves that had already been developed do not allow for an active control of the growth-induced pressure acting in the growth chamber. By choosing one of the three leaky valves (45°, 90° or 135°) in the experiment, we set the range of mechanical pressures a cell population exerts and consequentially experiences.

Several strategies for controlled closing of microfluidic channels with active valves by other research groups have already been developed. One example are Quake valves which work by implementing a second (or higher order) valve layer on top of a microfluidic channel layer [75]. One can close channels in a lower layer by increasing the hydrostatic pressure in the corresponding valve channel above. The two layers are separated by a thin horizontal layer of PDMS. A similar approach is used in a valve described by Abate *et al.* in [94] that we term Abate valve for convenience. Abate valves close a channel by increasing the hydrostatic pressure in an adjacent channel, with both channels being separated by PDMS walls. In this case all structures are part of the same horizontal layer.

First, we designed Quake valves as an active control of the growth-induced pressure. These valves are constructed to reduce the height of the exit channel. Parts of the two layers that compose the device are shown figure 5.7. The valve that is located over the exit channel pushes onto the PDMS layer when a hydrostatic pressure is applied. The fabrication process of this device which is made up of two structured PDMS molds is described in section 3.1.2.

Although, we successfully conducted experiments with this Quake valve design, which are presented in section 6.2.2, we decided to develop a different strategy to actively control the growth-induced pressure since the fabrication process of the Quake valves is difficult and non-reproducible. The fabrication of the Abate valve device is easier since only a single layer of PDMS is needed. The difficulties in producing Quake valves are due to the fact that the two PDMS layers require accurate alignment. In order to establish a bond between the two layers needed for a Quake valve we have to activate the surfaces in an O_2 plasma. After this
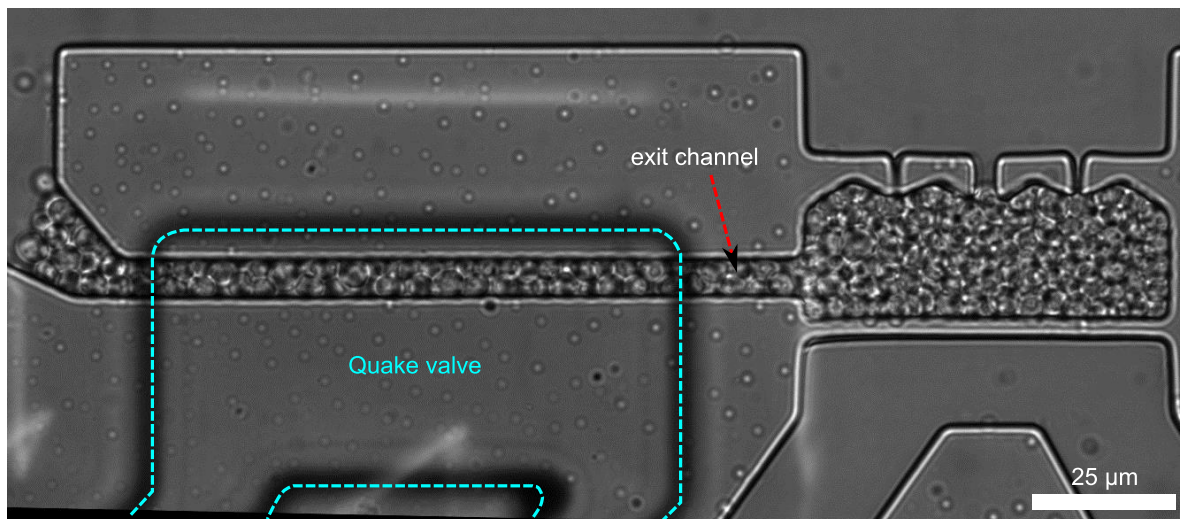

Figure 5.7: The Quake valve device is shown in this microscopic image. The Quake valve is positioned above the exit channel. The layer of the Quake valve is situated 10 µm above the lower layer and thus appears blurred since the focus is set to the lower structures. The boundary of the Quake valves is indicated by the turquoise, dashed lines.

plasma treatment the alignment of the two layers and the establishment of a contact have to take place during 1 minute. If this time span is not met, the bonding between the two PDMS layers is not strong enough to sustain the high hydrostatic pressures we want to apply onto the valves. The bonding strength of PDMS depends strongly on the parameters used during O_2 plasma treatment [72]. Another factor that complicates the process is that the two layers immediately bond upon contact. This means that small errors in alignment can occur easily (e.g. a shift in the order of 10 µm), which render the fabrication process non-reproducible since the effectiveness of the valve depends on its position above the exit channel. We decided to test Abate valves as a possible alternative, since these devices only require a single PDMS layer and consequentially are easier to construct in a reproducible way.

To this end an Abate valve with a length of 65 µm lying next to the exit channel separated by a 4 µm thick PDMS membrane as shown in figure 5.8 is implemented.

Unfortunately, the valve does not close the exit channel to a sufficient extent. We did not measure any difference in growth-induced pressure for valve pressures from 0.25 to 0.45 MPa. Additionally, we discovered that the close vicinity of the valve and control channel is disadvantageous. The PDMS between these channels separates frequently at valve pressures of about 0.5 MPa resulting in a leaking channel, which consequentially renders the valve unusable.

In the latest design (shown in figure 5.9) of the Abate valve we increased the distance from control channel to valve channel. Additionally, we increased the length of the valves to 300 µm and implemented a second Abate valve on the opposite side, so that the exit channel can be compressed from both sides. This device enables us to control the growth-induced pressure of the cell population as is presented in section 6.2.2. In order to incorporate the second Abate valve on the opposing side of the exit channel a new design of the nutrient supply system was necessary. This new design is introduced in the following section.

The aforementioned active Abate valve can in principle completely confine a cell population. In order to achieve this complete confinement a valve pressure higher than the maximal growth-induced pressure has to be applied. From the experimental data we found that this maximal growth-induced pressure can be as high as 1.2 MPa for *S. cerevisiae* (see section 6.2.2). When one applies a hydrostatic pressure of this magnitude (or even a pressure as low
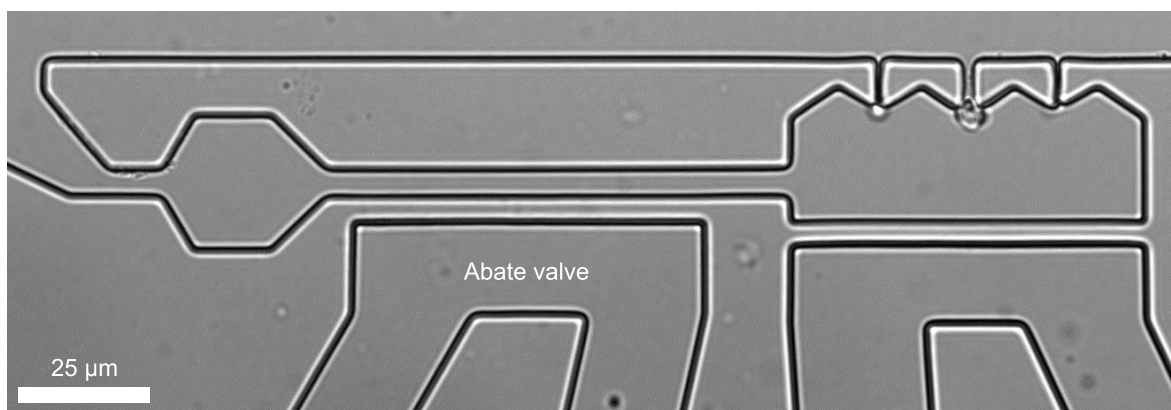

Figure 5.8: First design of the Abate valve, which has a length of 65 µm and is situated next to the exit channel. The idea behind this set-up is that the PDMS wall between exit channel and Abate valve gets displaced when the hydrostatic pressure in the latter is higher than in the exit channel.
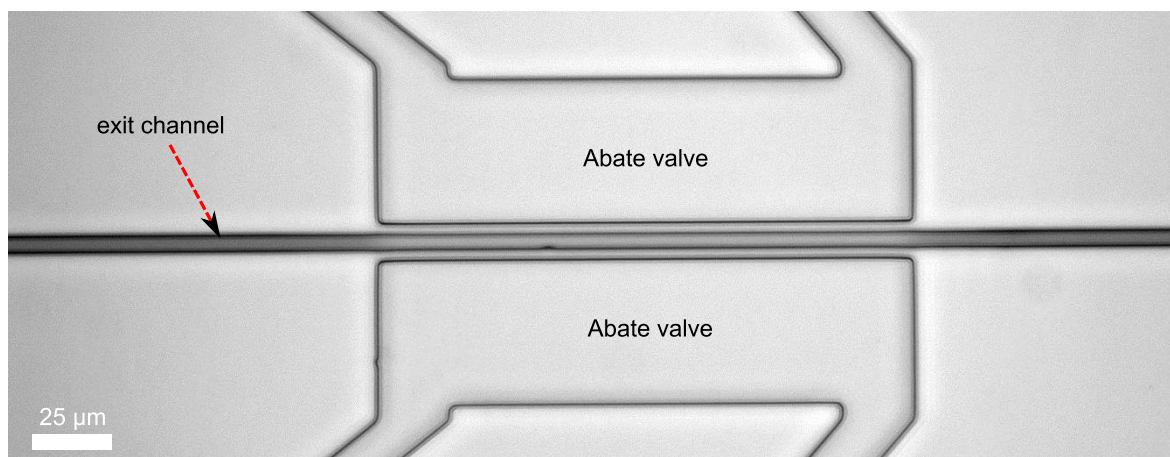
Figure 5.9: The final design of the Abate valve device is shown. The two Abate valves are 300 µm wide and situated next to the exit channel. Thus, the exit channel is compressed from both sides when a hydrostatic pressure is applied.

as 0.5 MPa) in a microfluidic PDMS channel bonded to glass, the PDMS can separate from the glass slide [72]. These high pressures can also detach the tubing from the inlets/outlets[‡]. As a consequence, we had to develop a different technique to completely confine yeast populations.

We designed a passive valve that exploits the growth-induced pressure the cells exert by letting the cells actuate the valve themselves, hence we name it self-closing valve. Figure 5.10 shows a self-closing valve in its open and closed state. The cells that proliferate in the extremities next to the exit channel push onto the surrounding PDMS (and thus push against the walls of the exit channel) resulting in narrowing of the exit. This process closes the valve nearly completely. The exit channel is narrower than the other valves we use (3 µm instead of 5 µm). However, it is still possible to load the device with *S. cerevisiae* cells, which have

_____

[‡]Of course, this can also be problematic for the actual growth-induced pressure measurement we conduct, but we fortunately found a solution for this problem (see section 5.4).
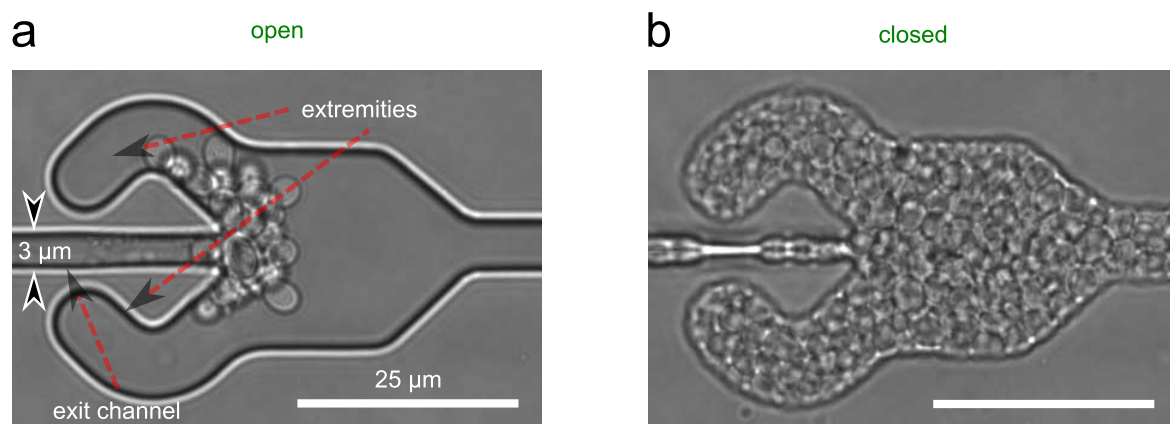

Figure 5.10: Microscopic images of the self-closing valve in its open a) and closed b) state. The growth-induced pressure exerted by the cells in the extremities narrow the exit channel.

a minimal diameter of 3.4 µm [15] since we can apply a high hydrodynamic pressure during loading of the device, which results in deformations that broaden the exit channel temporarily. For a detailed description of the dimensions of the various valve types be referred to figure A.4 in appendix A.

5.3.2   Nutrient supply

As described before (section 5.1.1) nutrients flow through and diffuse into the growth chamber by means of the nutrient slits. We observed in our experiments that *S. cerevisiae* cells can be pushed through these 1 µm wide nutrient slits provided that the growth-induced pressure in the growth chamber is at least as high as 0.2 MPa. Figure 5.11 shows an example of cells escaping via the nutrient slits. The possibility of cells escaping through these nutrient slits negatively influences the effectiveness of the designed valves rendering a complete confinement impossible. Furthermore, tracking and counting the cells that leave the growth chamber is nearly impossible. Due to the high flow velocity in the supply channel of $v_{\text{supply}} = 1\frac{\text{nl}}{\text{s}}/(10 \text{ µm} \cdot 15\text{µm}) \approx 6.7 \cdot 10^3 \frac{\text{µm}}{s}$ cells are washed away in about 0.02 seconds when slipping out of the left most nutrient slit[§]. Still, we want to estimate the number of cells leaving the growth chamber as well as possible in order to measure the growth rate as function of the growth-induced pressure (see section 6.2.4).
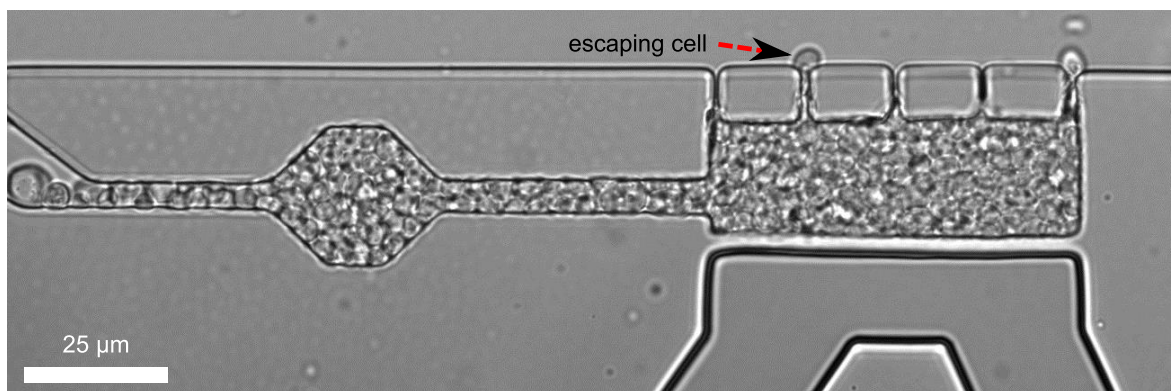

Figure 5.11: Microscopic image of the first version of the device is shown. Cells escape through the nutrient slits already at a pressure of about 0.2 MPa.

In a first attempt we changed the geometry of the pillars separating the nutrient slits from one another to a concave-planar shape (figure 5.12). The idea behind this approach is that cells pressing onto the concave side of the pillars would narrow the nutrient slits and thus keep cells from slipping through. As a result, cells are mostly escaping through the nutrient slits at the borders of the growth chamber as indicated by the arrows in figure 5.12. The minimal growth-induced pressure, at which cells escape through the nutrient slits in this device is still about 0.2 MPa.

Consequentially, we redesigned the device as shown in figure 5.13 by removing the slits at the borders of the growth chamber to close off the main reason for an unwanted loss of cells. We found that cells are still able to escape through the remaining slits, as can be observed in figure 5.13. The pressure at which cells escape is still about 0.2 MPa. Interestingly, no

---

[§]The length of the supply channel section that is still in the field of view during the imaging is about 80 µm.
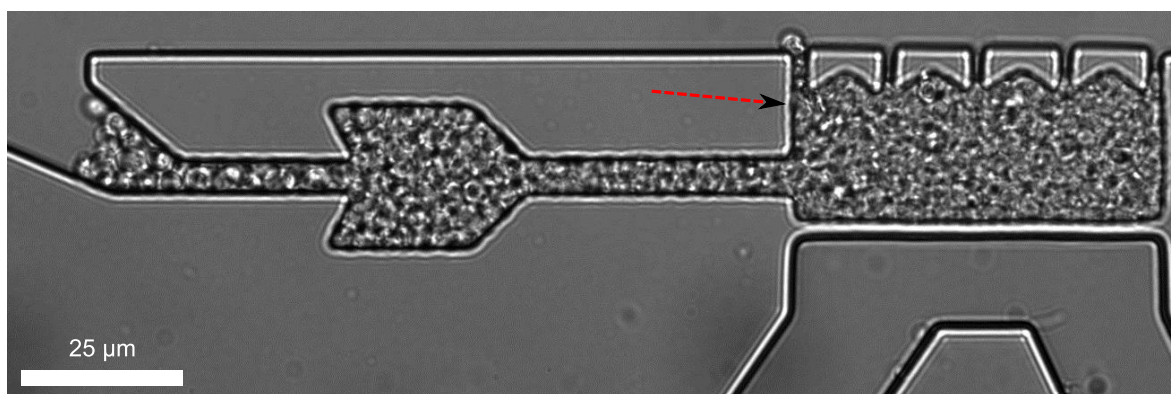
Figure 5.12: Microscopic images of the first redesign of the nutrient slits to have a concave-planar shape. Cells mostly escape through the nutrient slits at the borders of the growth chamber as indicated by the arrow. The pressure, at which cells start to escape through the slits is still about 0.2 MPa.
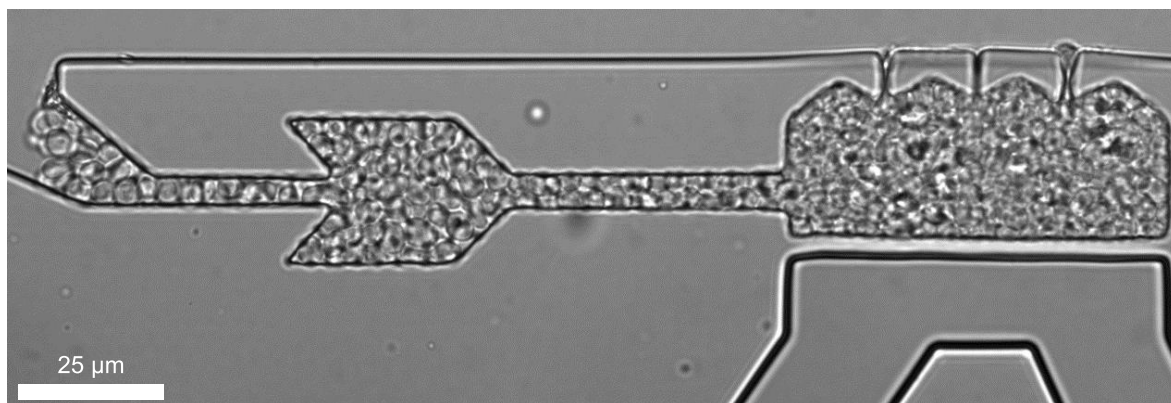

Figure 5.13: Microscopic images of the second redesign of the nutrient slits. The slits at the borders of the growth chamber have been removed. The pressure at which cells start to escape through the slits is still about 0.2 MPa.

matter the geometry *S. cerevisiae* cells are able to push through these narrow nutrient slits at the same growth-induced pressure. The reported value of 0.2 MPa is close to the turgor pressure that was previously reported for non-confined cells [23]. When approaching growth-induced pressures of this magnitude the cells might increase their internal turgor pressure to counteract this external mechanical pressure (compare section 2.2). This turgor pressure increase might enable the cells to deform the narrow nutrient slits made of PDMS and squeeze themselves through. This might be similar to bacteria that pass through narrow channels simply be means of growth and division forces [16] (see also section 2.7.1).

Consequentially, we developed a nutrient supply mechanism that does not rely on nutrient slits as previously employed to feed the cells in the growth chamber in order to block this escape route for the cells. Figure 5.14a depicts a device, in which the growth chamber is centered between two self-closing valves. This device completely confines a cell population, but we find that cells do not have access to the same amount of nutrients. The valves are closer to the nutrient channel so that they have easier access to fresh nutrients as compared to
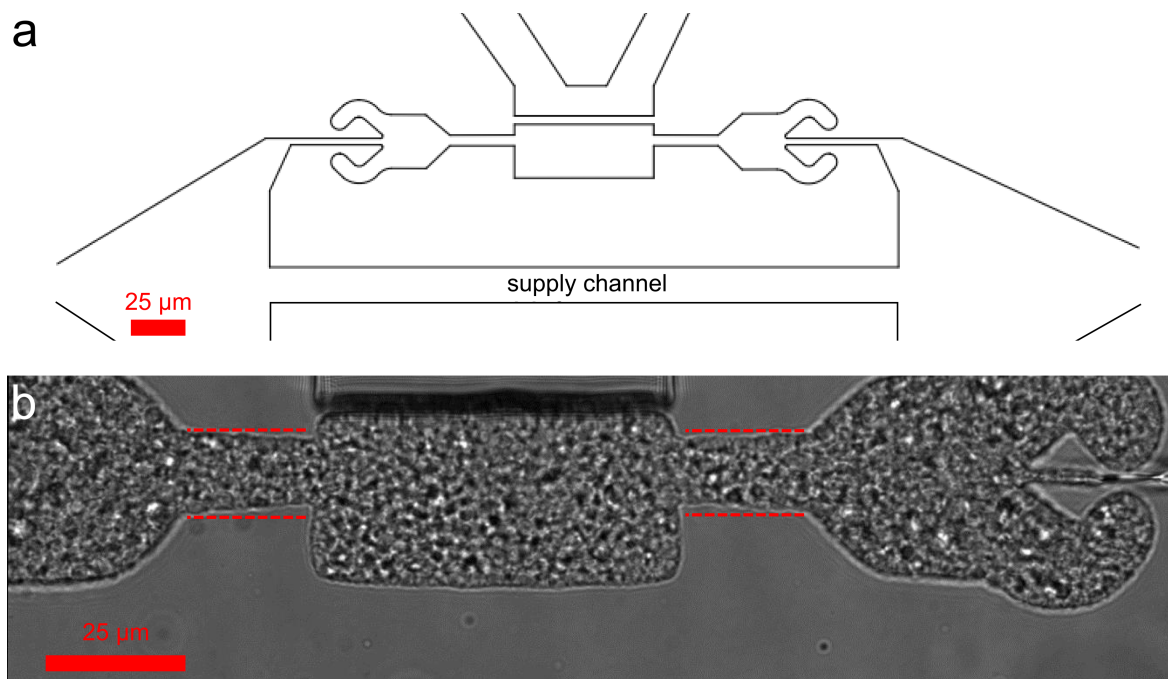
Figure 5.14: Sketch a) and microscopic image b) of a device without any nutrient slits. The growth chamber is centered by two self-closing valves. b) Cells do not grow with the same rate in the growth chamber versus inside of the walls before a steady state is reached. The pressure difference is visible by the deformation of the channels which changes with respect to the distance from the valves. This dependency hints at a higher pressure acting in the valves as compared to the growth chamber.

cells in the growth chamber. Consequentially, cells in both self-closing valves grow faster and exert higher local growth-induced pressures than in the growth chamber as long as the steady state has not been reached. The difference in growth-induced pressure and hence growth rate can be observed qualitatively in figure 5.14b. The deformation of the channels between valves and growth chamber very likely result from a pressure difference between these structures. The channels are deformed closer to the valves than near the growth chamber hinting at a non-zero pressure gradient between valves and growth chamber. We measured the velocity of cells in these channels by means of particle image velocimetry (for details of the analysis see section 4.3) and plotted the result in figure 5.15. Positive velocity values correspond to a movement of cells from left to right, while negative values indicate a movement in the opposite direction. One can observe in this plot that cells were transported from the valves towards the growth chamber by the forces generated by growth and division of the cells. This shows that the nutrient conditions in the growth chamber are not ideal, but since we want to study the effect of mechanical pressure on confined cell populations without additional influences of nutrient limitations, a more reliable method of nutrient supply to the growth chamber had to be designed.

We designed nutrient channels that deliver nutrients directly to the growth chamber. The design is depicted in figure 5.16. In this device, we do no longer require a supply channel to load the growth chamber. We simply load the device directly through the exit channel. The inset in figure 5.16 shows the side view of the growth chamber at the position where the
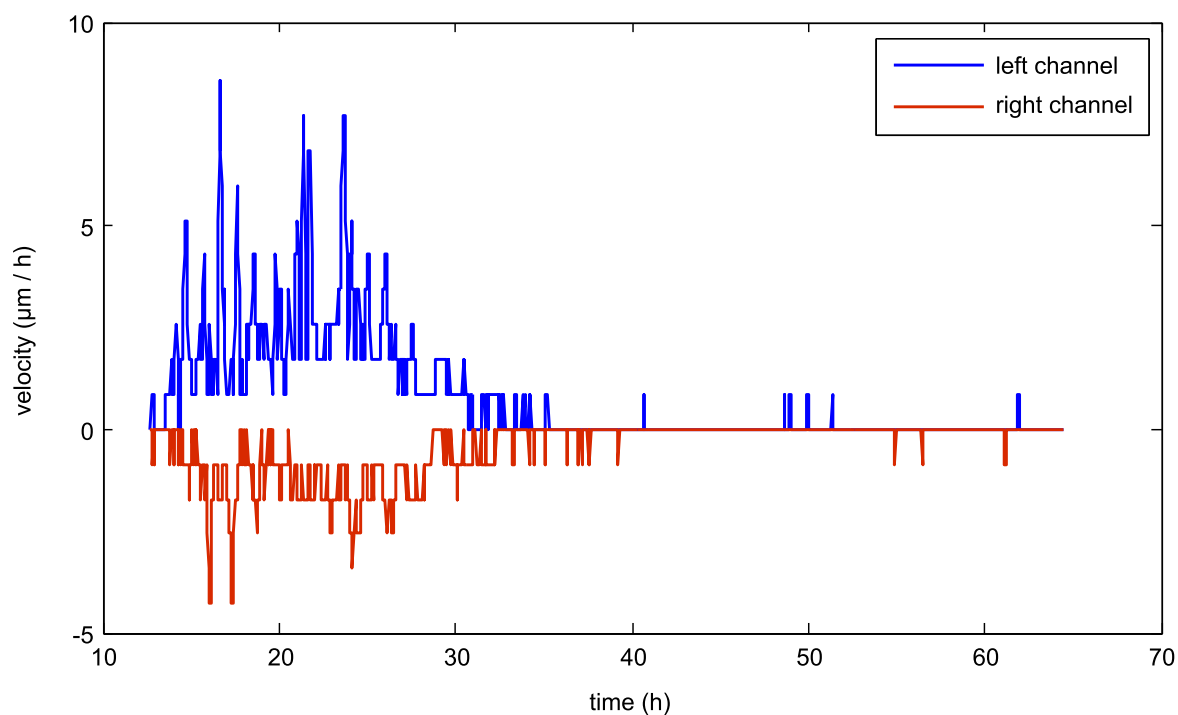
Figure 5.15: Results of the analysis of the experiment shown in figure 5.14. Cell velocity in the channel between valves and growth chamber as a function of time is plotted. A positive velocity indicates a movement of cells from left to right, while a negative velocity corresponds to a movement from right to left.
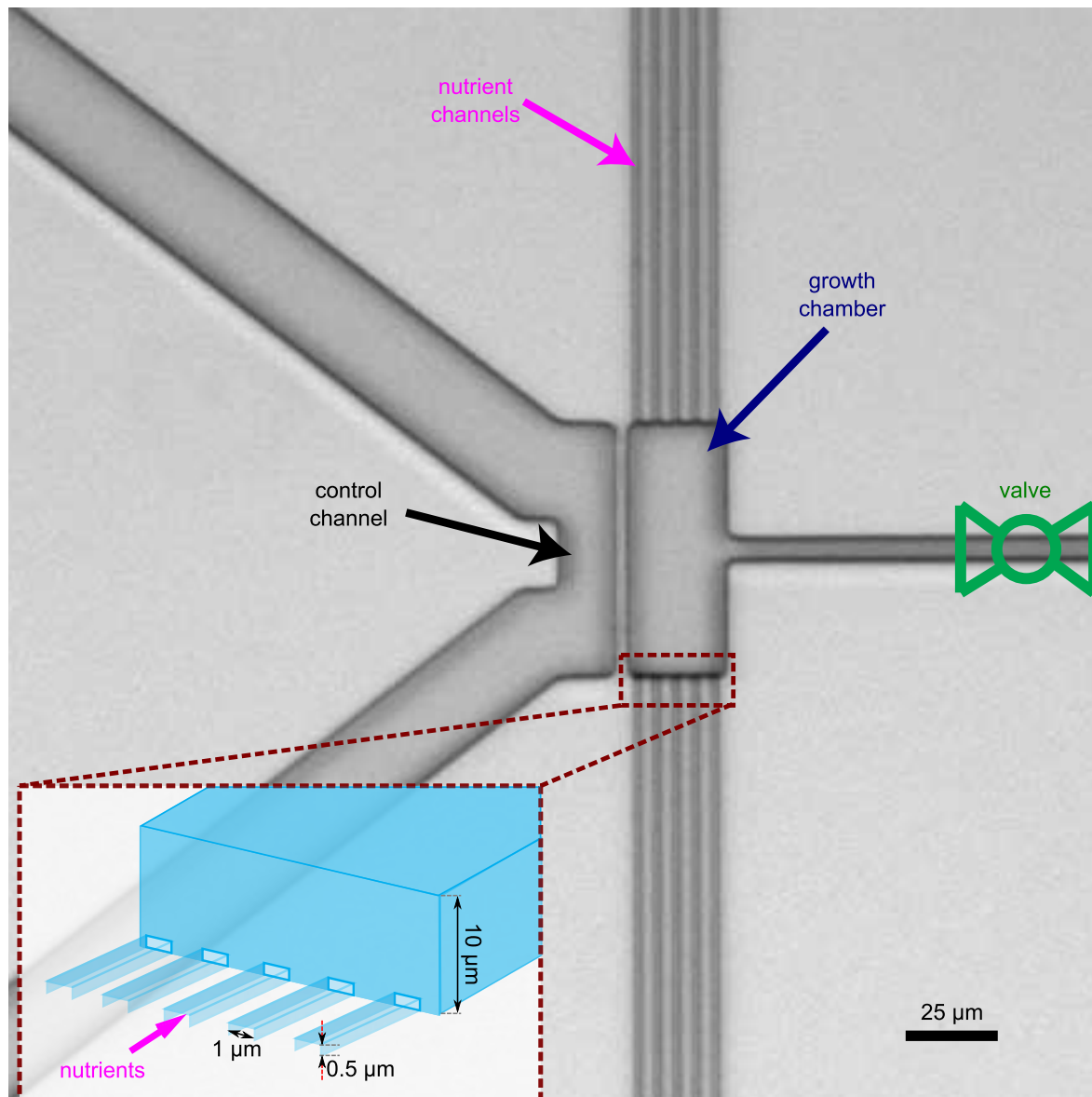
Figure 5.16: The latest design of the device is shown. Inset) Side view of the growth chamber at the position where the nutrient channels enter the growth chamber is shown. The nutrient channels are lower (0.5 µm compared to 10 µm) than all other parts of the device. These channels are nearly (except at very high growth-induced pressures) impassable for *S. cerevisiae* cells.

nutrient channels are connected to the growth chamber. The nutrient channels are only 0.5 µm high and 1 µm wide, which makes them nearly[¶] impassable for *S. cerevisiae* cells that have a minimal diameter of 3.4 µm [15].

The nutrient channels enable us to keep the nutrient conditions in the growth chamber at an ideal level. This is shown in section 6.2.1, where we determine the diffusion constant of glucose in the growth chamber filled with cells and incorporate this result into finite element simulations. Additionally, we can also change the chemical environment of the cells at any state of the experiment by replacing the nutrient medium with a desired chemical, which is then pumped through the nutrient channels.

5.4 Pressure measurement development

5.4.1 Pressure sensors

In a first step, the pressure measurement was improved by replacing the air filled syringes connected to the water reservoir in the tubes and control channel (compare section 5.2) with hydrostatic pressure sensors that are attached to a 10 ml glass syringe mounted onto a neMESYS mid pressure module syringe pump (all components were bought from cetoni, Korbussen, Germany). This setup enables us to change the hydrostatic pressure in the control channel by pumping water in or out of the PDMS device with the syringe pump. The pressure sensor generates a voltage signal that is an affine function of the hydrostatic pressure.

The implementation of pressure sensors enables us to measure the hydrostatic pressure in the control channel accurately. However, to adjust the hydrostatic pressure to counteract the growth-induced in the growth chamber precisely, is another challenge. The actual precision with which the membrane is balanced is what sets the quality of the measurement of the growth-induced pressure.

5.4.2 Feedback algorithm

In the experiments conducted during the beginning of this project, balancing of the membrane was achieved by adjusting the hydrostatic pressure manually. When the membrane was displaced it was judged by eye how to change the hydrostatic pressure to compensate for the displacement. This method is inaccurate since very small displacements can not be properly measured. Furthermore, this measurement technique turns out to be subjective as can be seen in figure 5.17. The growth-induced pressure was manually measured in collaboration with Dr. Morgan Delarue in a device, where the growth chamber is centered between two self-closing valves (compare figure 5.14a). We observe an increase in the growth-induced pressure when another researcher took over the measurement[‖] as indicated by the arrow in figure 5.17. This increase is simply an artifact since each of us judged differently when the membrane was balanced. This observation led us to set the error bars of the measurement to 0.05 MPa.

Due to these problems of the manual measurement, it was of utmost importance to develop an automatic and accurate method to balance the membrane and through this measure the

---

[¶]We found that at very high growth-induced pressures (about 1.0 MPa) the PDMS can deform enough for the cells to enter these narrow channels but these cells immediately get stuck in the channel, making it harder for the next cell to enter the nutrient channel.

[‖]We took turns to measure the growth-induced pressure manually, since the overall measurement took about 24 hours.
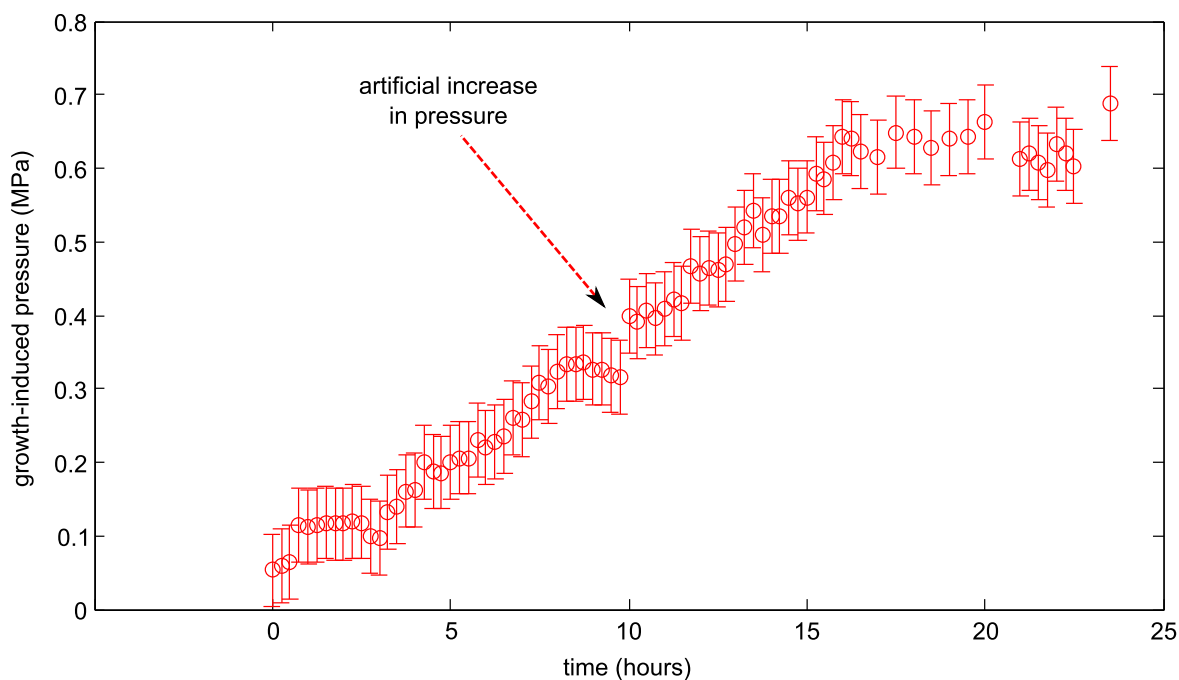
Figure 5.17: Result of a growth-induced pressure measurement, in which the pressure was measured by adjusting the membrane displacement by hand. The jump after 10 hours is a measurement artifact. This artifact arises as the first part of the measurement was conducted by another researcher than the second part.

growth-induced pressure cell populations exert in our device. To this end, a robust image processing algorithm is needed that can extract the displacement of the membrane, but the image acquisition software (Xcellence, Olympus, Hamburg, Germany) does not allow for live image processing to the required extent. It is especially important for us to be able to adjust the hydrostatic pressure in the control channel in accordance to the result of the image processing, which is used as a feedback. In a further collaboration with Dr. Morgan Delarue a live image processing algorithm was developed that allows to directly apply a pressure feedback. All hardware components are controlled via a custom Matlab program. In the following we described several aspects of this program.

The principle of the feedback algorithm is illustrated in figure 5.18. Initially, the program determines the ideal focal plane by acquiring images in a region of interest containing only the nutrient channels** at different focal planes and calculating a quantitative score for each image I individually as detailed below (figure 5.18a). For each image I the local standard deviation for each individual pixel is calculated in a 3x3 pixel neighborhood with the STDFILT function provided by Matlab. The result is a matrix J that has the same size as I with the components being the local standard deviation of the corresponding pixel in I. We define the

---

**If we would use structures of the device with cells inside, the deformation of the PDMS by the growth of the cells would alter the results for the determination of the ideal focal plane. This bias can lead to a drift in the focal plane during the experiment. The nutrient channels are the only structures in the field of view that do not contain any cells and are consequentially not influenced by this bias.
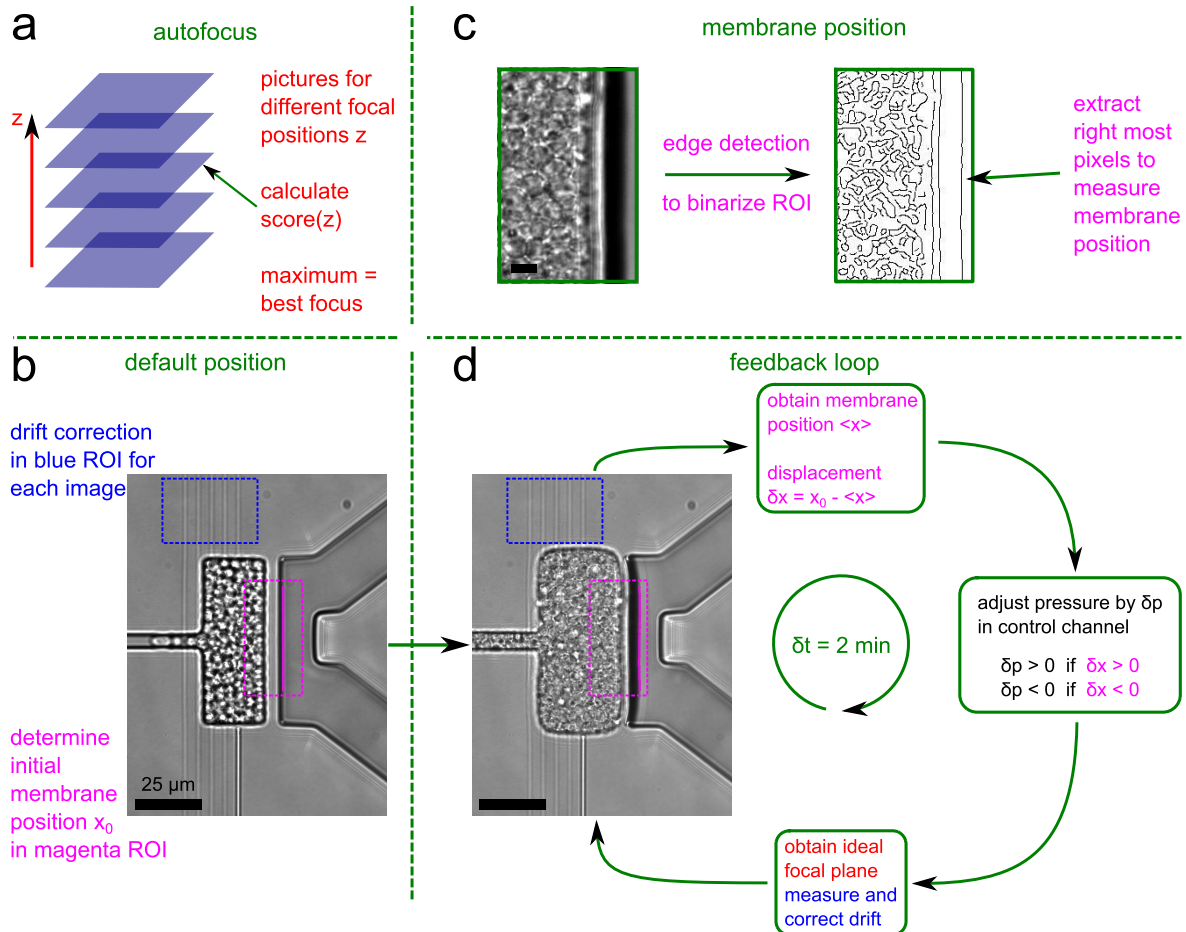
Figure 5.18: The feedback algorithm with several necessary analysis steps is shown. a) For the autofocus, images are acquired at different focal positions and a score representing the mean local standard deviation of each image is calculated. The maximum score gives the best focal position. b) The default membrane position is calculated by edge detection of a ROI around the membrane, while autofocus is maintained and possible drifts are accounted for. c) An example for the edge detection is shown. The binarized image has been inverted and the membrane position is extracted by averaging over the right most detected edge in the binarized image. d) In the feedback loop the membrane position is measured, focus is maintained and drift is corrected for. The hydrostatic pressure is changed according to the displacement of the membrane.

score for the ideal focal plane through the average local standard deviation for each image as

$$\text{score} = \frac{1}{M \cdot N} \sum_{i=1}^{M} \sum_{j=1}^{N} J_{ij} \tag{5.7}$$

for an image with $M \times N$ pixels. The ideal focal plane was defined as the image with the highest score. A high local standard deviation hints at a sharp image, while a defocused (blurred) image has a relatively low local standard deviation. The gray scale values of the defocused image do not differ as strongly, especially in a local neighborhood around each pixel.

After this autofocusing, a picture is taken at the derived ideal focal plane. Two regions of interest (ROI) are selected as shown in figure 5.18b. The dashed blue rectangle is located above the nutrient channels to correct for possible drifts perpendicular to the membrane. We correct for possible drifts at every acquisition during the experiments, hence we require a drift correction algorithm that does not use up too much computational time. We calculate the cross correlation between the ROI of the initial image A_{ROI} and current image B_{ROI}

$$C(s,t) = \sum_{i=1}^{M} \sum_{j=1}^{N} A_{\text{ROI}}(i,j) \cdot B_{\text{ROI}}(i+s, j+t)^* \tag{5.8}$$

with * denoting the complex conjugation. The second image is shifted by s pixels in x-direction and t pixels in y-direction. The direct calculation of this double sum for all possible combinations of s and t is costly in terms of computational time. Fortunately, one can calculate the Fourier transform of C by one simple matrix multiplication and by an inverse Fourier transform

$$C = F^{-1} \left[F[A_{\text{ROI}}] \cdot F[B_{\text{ROI}}]^* \right], \tag{5.9}$$

which directly follows from the convolution theorem. Matlab provides a fast Fourier transform algorithm that only requires $2MN \log_2(MN)$ arithmetic operations for each Fourier transform [95], while the direct calculation over the double sum in equation (5.8) for all s and t requires $(MN)^2$ operations in total. For a typical ROI size of about 100×100 pixels this translates to about $8 \cdot 10^5$ operations for the Fourier transform method and 10^8 operations for the direct calculation, which means that the Fourier transform method is over 100 times faster.

The position of the maximum of C gives the needed correction vector for the current image with respect to the initial image for drift correction. The position of the second ROI positioned above the membrane (dashed magenta rectangle in figure 5.18b) is drift corrected accordingly. This second ROI is required to measure the position of the membrane by means of image processing. The Matlab function EDGE with the Canny edge detection option is applied to the ROI (low threshold 0.1, high threshold 0.5). This function calculates local gray scale value gradients using the derivative of the Gaussian filtered image and generates a binary image based on the result [96]. Pixel in the ROI for which a local gradient maximum above the high threshold[††] is found are set to 1, while the remaining pixel values are set to 0 (see figure 5.18c for an example image). The detected edge indicated by the arrow in figure 5.18c are extracted from the binarized image to determine the position of the membrane. This process is repeated for an hour with pictures being taken every 2 minutes and the

---

[††]Weak edges are detected when the local gradient maxima are higher as the low threshold if they are connected to strong edges, which is not required for our image processing, but simply part of the edge detection algorithm [96].

default position of the membrane is calculated from the average of all accumulated values. Before calculating the position of the membrane in each image the best focal position is again calculated by the autofocussing algorithm and a possible drift perpendicular to the membrane is corrected for by means of the drift correction algorithm.

After the calculation of the default membrane position x_0 has been established the experiment starts. In each time step the best focal position is determined and after the pictures have been taken the drift perpendicular to the membrane is corrected as previously described. The pictures are taken in each time step and the mean position of the membrane $<x>$ is calculated from the edge detected images. If the membrane has been displaced $\delta x = x_0 - <x> \neq 0$ the hydrostatic pressure is changed accordingly by $\delta p = \text{sgn}(\delta x) \cdot 0.005\text{MPa}$ (sgn is the sign function) by activating the syringe pump (figure 5.18d). The new hydrostatic pressure is recorded and an image is acquired at the corresponding time step. The growth-induced pressure is measured with an error of 0.005 MPa with this feedback algorithm as is calculated in section 6.2.1.

5.4.3 Pressure from membrane displacement

As previously discussed the PDMS can separate from the glass when a hydrostatic pressure of about 0.5 MPa is reached in the control channel. We found that a completely confined *S. cerevisiae* population (undomesticated yeast strain BR-F) exerts a maximal growth-induced pressure of about 1.2 MPa. We are not able to measure this high pressure regime by using the feedback algorithm. Instead we can measure the growth-induced pressure directly from the displacement of the membrane. The feedback algorithm has the advantage that it is twice as precise in terms of pressure than the direct measurement of the membrane position (see section A.4 for the calculation of the error for the membrane displacement measurement technique and section 6.2.1 for the calculation of the error of the feedback algorithm measurement). The temporal resolution of the feedback method depends on the speed of the algorithm and the hardware components (e.g. pumps). The temporal resolution of the pressure measurement from the displacement of the membrane is better since it is directly determined by the frequency of image acquisition. Consequentially, we use the feedback algorithm for experiments, in which the pressure does not rise higher than 0.5 MPa and when we are not interested in a high temporal resolution. The hydrostatic pressure in the control channel is maintained at an effective value of 0 MPa (subtracted by the atmospheric pressure) when we measure the growth-induced pressure directly by the displacement of the membrane. In order to extract the growth-induced pressure from the measurement of the membrane displacement a calibration curve is required.

A test membrane with adjacent channels is implemented in each of the devices. The hydrostatic pressure on one side of the membrane is increased stepwise and the corresponding membrane displacement is measured with the edge detection method described in section 5.4.2. The maximal hydrostatic pressure we can apply without risking leakage is 0.5 MPa. Up to this pressure the calibration curve gives a linear relationship between pressure p and membrane displacement d. The average calibration curve (from all experiments) is given as

$$d = 7.30 \ \mu\text{m} \cdot p. \tag{5.10}$$

The error of the distance measurement is about 0.07 µm due to the edge detection that can only determine the position of the membrane with an error of 0.5 pixels. In the microscopic images we acquire with our microfluidic device 1 µm is equal to 7 pixels.

Since we also want to measure higher growth-induced pressures, we have to determine how the functional relationship between displacement and pressure can be described for higher pressure values. In order to achieve this we conducted finite element simulations with Comsol. The finite element simulations are described in detail in section 4.4. We obtain a relationship between the displacement of the membrane and the pressure acting in the growth chamber. The displacement is given as

$$d = 12.09 \ \mu\text{m} \cdot \frac{p}{E} \tag{5.11}$$

with E the Young's modulus of the PDMS and p the acting pressure. When comparing equations (5.10) and (5.11) we can estimate the Young's modulus of our devices, which gives a value of about 1.7 MPa. This is in good agreement with the study of Johnston *et al.*, in which the Young's moduli of PDMS was measured for different curing temperatures for a base to curing agent ratio as is used in our experiments [70].

We can also improve the pressure measurements of the old experiments, in which we measured the growth-induced pressure manually, by means of finite element simulations. In this case it is not possible to use the displacement of the membrane to measure the growth-induced pressure since the hydrostatic pressure in the control channel was changed manually, which makes it difficult to properly define the change with respect to the default position of the membrane. We chose to measure the width of the channel connected to the growth chamber instead to extract the growth-induced pressure from the change in channel width. From the microscopic images of the experiments we can measure the channel width by applying the previously described edge detection algorithm, but this time choosing a region of interest located over the channel and extracting the positions of both outer walls of the PDMS channel. The calibration curve for the channel width w as a function of pressure is calculated from the finite element simulations (details are described in section 4.4)

$$w = 11.63 \ \mu\text{m} \cdot \frac{p}{E} + 5 \ \mu\text{m}. \tag{5.12}$$

Chapter 6

Results

We present the experimental results in this chapter. First of all we show the outcomes of the agar gel crack experiments. In these experiments yeast colonies are grown embedded in agar gels or in cavities plunged into agar gels (cf section 3.3).

In the following the characterization of the latest microfluidic device, shown in figure 5.16, is presented. This characterization includes

- the degree with which the cells are confined by the various valves,

- the analysis of the nutrient supply to the cells in the growth chamber,

- and the pressure measurement technique via feedback algorithm.

In the subsequent sections the various pressure curves are shown and the growth rate as a function of pressure is presented. Furthermore, we present the results of an experiment conducted with the undomesticated yeast strain BR-F. This strain expresses strong cohesive cell-cell bonds. Further analysis of the pressure curves corresponding to the leaky valve devices gave access to statistical results on the occurring cell avalanches.

Additionally, we analyzed fluorescence time lapse series conducted with the Whi5-GFP strain. This strain enables us to distinguish between cells having committed to cell division and cells delayed in the G1 phase of the cell cycle (cf section 3.2).

Finally, we qualitatively show how growth-induced pressure influences cellular shape.

6.1   *S. cerevisiae* in agar gels

6.1.1   Plunging of cells into agar gels

We observed that *S. cerevisiae* cells can propagate cracks in agar gels. As described in section 3.3 we initiated cracks by plunging syringe needles seeded with *S. cerevisiae* cells (lab strain S288c and undomesticated strain BR-F) into agar gels. The initial cracks that result from the insertion of a syringe needle extents in opposite directions as can be observed in figures 6.1Ia and 6.1Ib. The figures show the cracks at time points at which the yeast cells filled the entire cracks by proliferation but before the cracks started to propagate. In figures 6.1IIa and 6.1IIb the cracks are depicted after 26.5 hours. The cracks maintained their main direction during propagation. We do not observe any obvious difference between the two yeast strains.

We also used pipette tips instead of syringe needles to initiate cracks in agar gels. The initial cracks for one of these experiments are shown in figure 6.1Ic and the propagated cracks
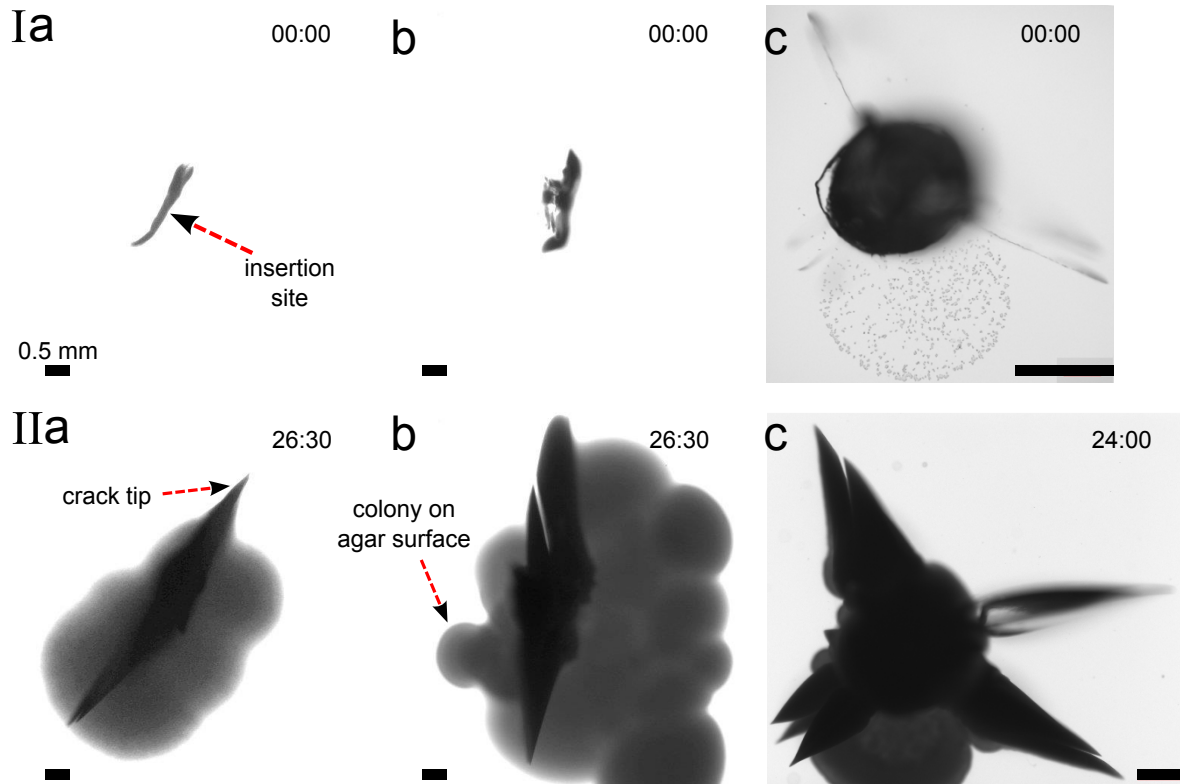
Figure 6.1: Ia,Ib) Images of initial cracks, initiated with syringe needles, in agar gels that are filled with cells of the strains S288c and BR-F, respectively. IIa,IIb) Images after 26.5 hours of the same cracks as shown in Ia, Ib, in which the cracks propagated by cell proliferation. Ic) Initial crack pattern that was initiated by plunging a pipette tip with cells of the lab strain S288c into the agar gel. IIc) The cracks propagate in the star shaped crack pattern. The crack on the right hand side of the insertion site is likely out of focus and thus not well visible in Ic.
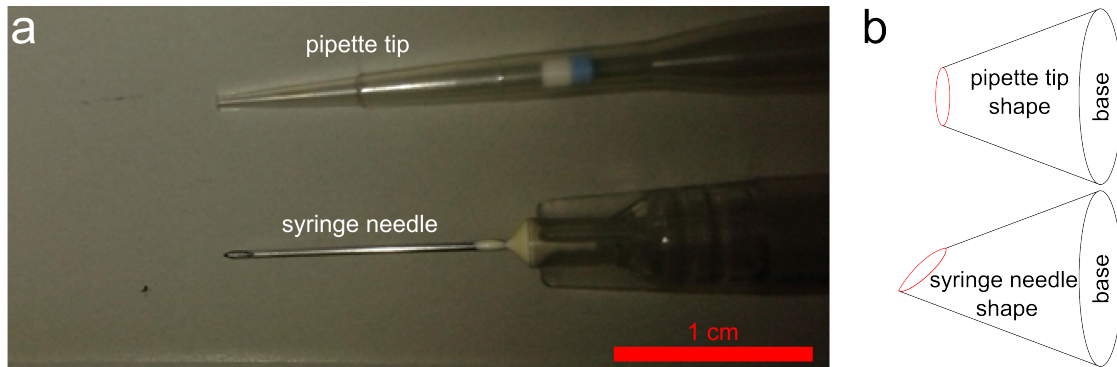
Figure 6.2: a) A pipette tip and a syringe needle that were used to plunge holes into agar gels are shown. b) A schematic representation of the shape of the tips of a pipette tip and a syringe needle are depicted as cuts from cones.

after 1 day are depicted in figure 6.1IIc. The resulting crack pattern is star shaped in contrast to cracks initiated with syringe needles. In section A.3 we present more crack patterns that were initiated either with syringes or pipette tips. The crack patterns initiated with syringe needles always extent in opposite directions from the insertion site, while the pipette tip crack patterns are star shaped in the experiments conducted here. We can explain this difference by taking the shape of the plunging tools into account (see figure 6.2a). The shape of the pipette tip can be described as a cone, which top was truncated parallel to its base. The syringe needle tip on the other hand is shaped like a cone, which top was cut off at an angle with respect to its base (cf figure 6.2b).

6.1.2 *S. cerevisiae* colonies embedded in agar gels

We embedded *S. cerevisiae* colonies of the lab strain S288c in agar gels as described in section 3.3. This method enables us to confine cells without initiating any artificial cracks. We observed that the embedded colonies of the lab strain S288c yeasts grow as shown in figures 6.3a and 6.3b. 4 to 8 hours after embedding of the colonies cracks appear in the agar gels next to the growing colonies (see figure 6.3c). The cracks are filled with cells and propagate by the growth and division of the yeasts as depicted in figure 6.3d.
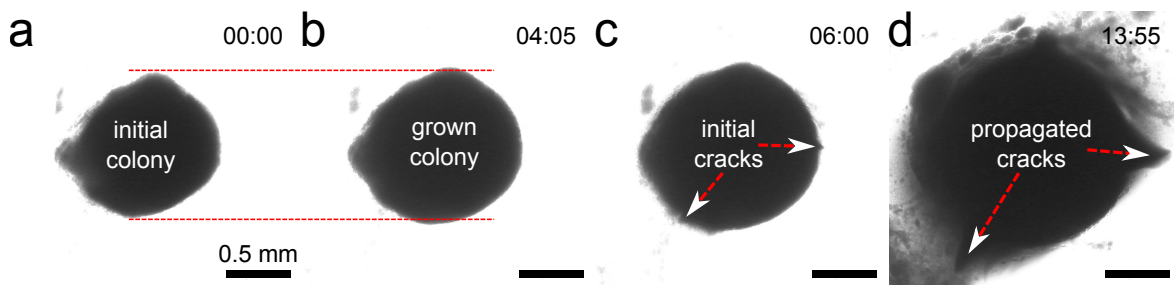

Figure 6.3: a) A yeast colony of the lab strain S288c is shown directly after embedding. b) The colony grows and compresses the surrounding agar gel in the next 4 hours and 5 minutes. c) First cracks appear adjacent to the colony. d) The cracks propagate and the colony keeps on growing.

We extracted the growth-induced pressure from the volume of the colonies (cf section 4.1 for the volume measurements) by simulating the compression of the surrounding agar gel through Comsol simulations as described in section 4.4.1. We obtained relations between growth-induced pressure and volume of the colony from these simulations that we applied to our colony volume measurements. One has to keep in mind that the formation of cracks in the agar gels leads to a release of growth-induced pressure in the colony. Consequentially, we can only extract the growth-induced pressure from the volume of the colony before any cracks appear. The time dependent growth-induced pressure curves for different initial colony volumes $V_{initial}$ are shown in figure 6.4. The pressure curves show exponential increases, where the values at the end of the curves mark the failure pressures at which the agar gels start to crack. The average failure pressure is 0.047(3) MPa, in which the error was calculated from the standard deviation of the mean. This average failure pressure is close to the compressive strength* of the agar gels with about 0.059 MPa of agar gels (for 2% agar, as we use in our experiments) measured by Nussinovitch and Peleg [97].

We embedded colonies of the undomesticated lab strain BR-F in agar gels. In all of these experiments the BR-F colonies detached part of the agar gel immediately after embedding. A cavity between the newly formed agar layers was created by the detachment and this cavity grew as shown in figure 6.5. As a consequence, we could not extract the growth-induced pressure from these experiments since the BR-F yeast colonies did not stay confined.

---

*The compressive strength is defined as the stress, at which the material fails under compression.
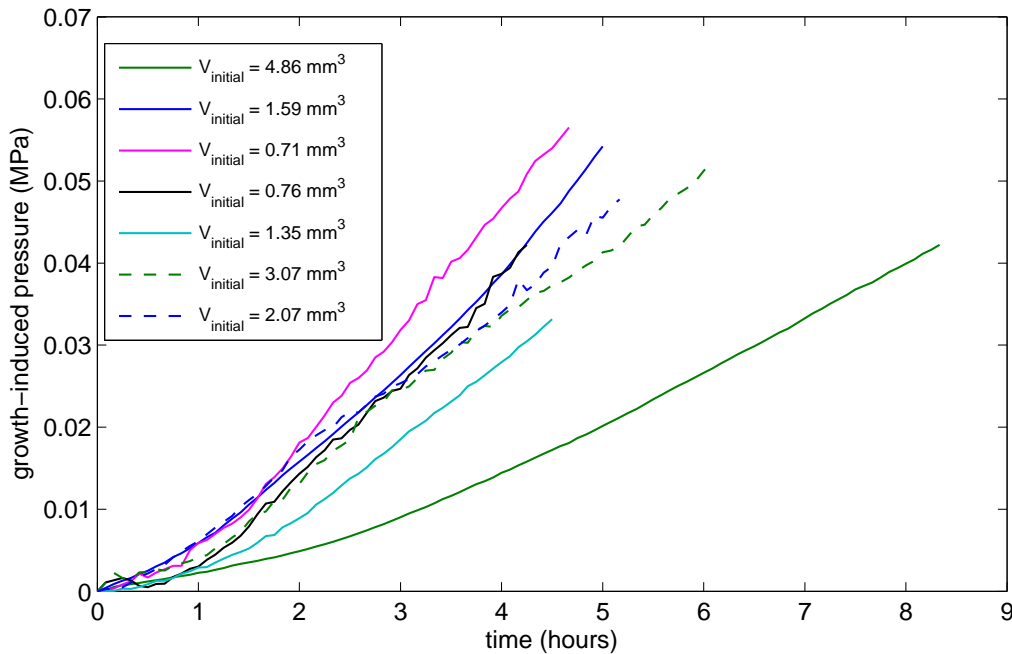

Figure 6.4: The growth-induced pressure curves of the colonies with different initial colony volumes $V_{initial}$ embedded in agar gels are shown.
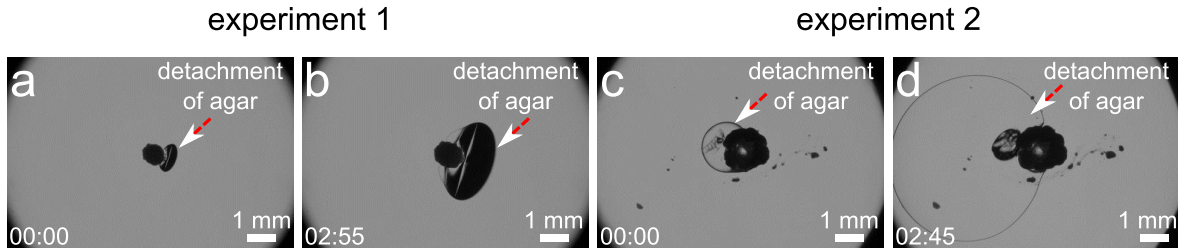
Figure 6.5: a+c) The two pictures show a BR-F colony directly after embedding. The agar gel starts to detach immediately after the colonies are embedded. b+d) The detachment of the agar gels continue. Hence, the BR-F colonies do not stay confined.

6.2 Microfluidic experiments

6.2.1 Device characterization

Degree of confinement

In order to quantify the confinement of the various valves we determine the cell flow in the channels exiting the valves. The dashed blue rectangle in figure 6.6a illustrates the position of the region of interest (ROI) used to measure the cell flow rate

$$Q_{\text{cell}} = \frac{v \cdot A}{V_{\text{cell}}}. \tag{6.1}$$

v is the cell velocity parallel to the exit channel, A the cross section of the channel and V_{cell} the average volume of a cell ($V_{\text{cell}} \approx 65\ \mu\text{m}^3$ for a spherical cell with an average diameter of 5 µm [93]). We make use of the fluid like behavior of the cell population when the cells are not confined by cell clots in order to measure the outflow of cells (cf section 2.6). We found that the cross section stays at its default value for the leaky valves since the cells do not deform the 5 µm wide exit channels. In the case of the self-closing valve the exit channel is only 3 µm wide, so that cells will deform the channel when passing through. Hence, we have to
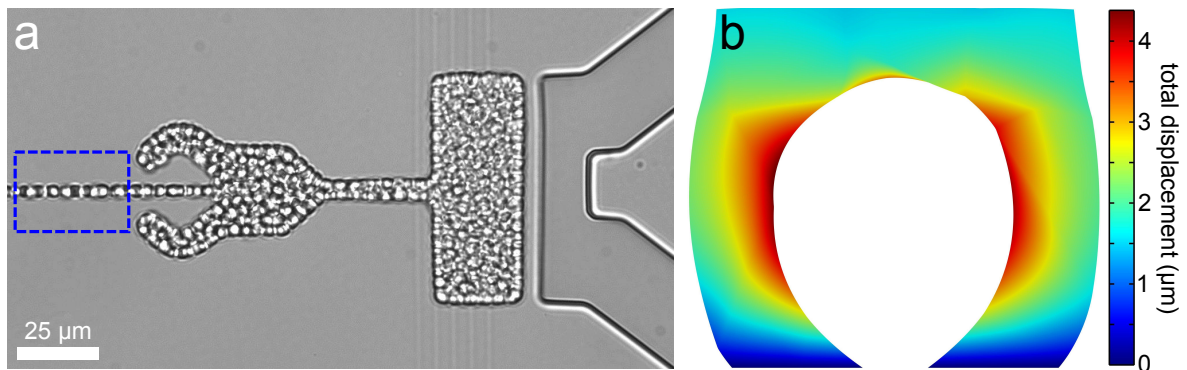

Figure 6.6: a) The cell flow velocity is measured in the region of interest indicated by the dashed blue rectangle. The velocity is determined by applying a particle image velocimetry algorithm. b) The cross section of the exit channel is shown with a pressure of 1.1 MPa acting onto the channel walls. The deformation is calculated by a Comsol simulation. The color bar represents the total displacement of the PDMS.

measure the channel width to determine the cross section. The exit channel does not deform isotropically when a pressure is applied inside of the channel as can be observed in figure 6.6b. Here, the result of a Comsol simulation is shown, in which a pressure is exerted onto the channel walls. We determine the cross section as a function of the channel width and plot the result in figure A.3 in section A.1. The cell velocity v is measured by a particle image velocimetry algorithm (PIV). The PIV algorithm determines the displacement of the cells parallel to the channel between two images. This displacement is divided by the difference in acquisition time of the two images (cf section 4.3). We define the degree of confinement for a valve as

$$doc = 1 - \frac{Q_{\text{cell, with valve}}}{Q_{\text{cell, without valve}}}. \tag{6.2}$$

We normalize the cell flow rate of a given valve by the cell flow rate through a plain 5 µm channel.

The degree of confinement for the various valves is plotted in figure 6.7. As can be seen by a *doc* of about 98 % the self-closing valves confine *S. cerevisiae* populations nearly completely only about 0.75 cells per hour escape. The leaky valves on the other hand only confine the cell populations partially. The 90° and 135° leaky valves have degrees of confinement of about 55 % and 65 % respectively. The 45° leaky valve has a significantly lower *doc* of about 20 %. The error bars correspond to the standard error of the mean calculated over all experiments of a given valve. For the 45° valve we could only conduct one successful experiment in the scope of this thesis so that we assumed an error bar equal to the average of the other leaky valves.
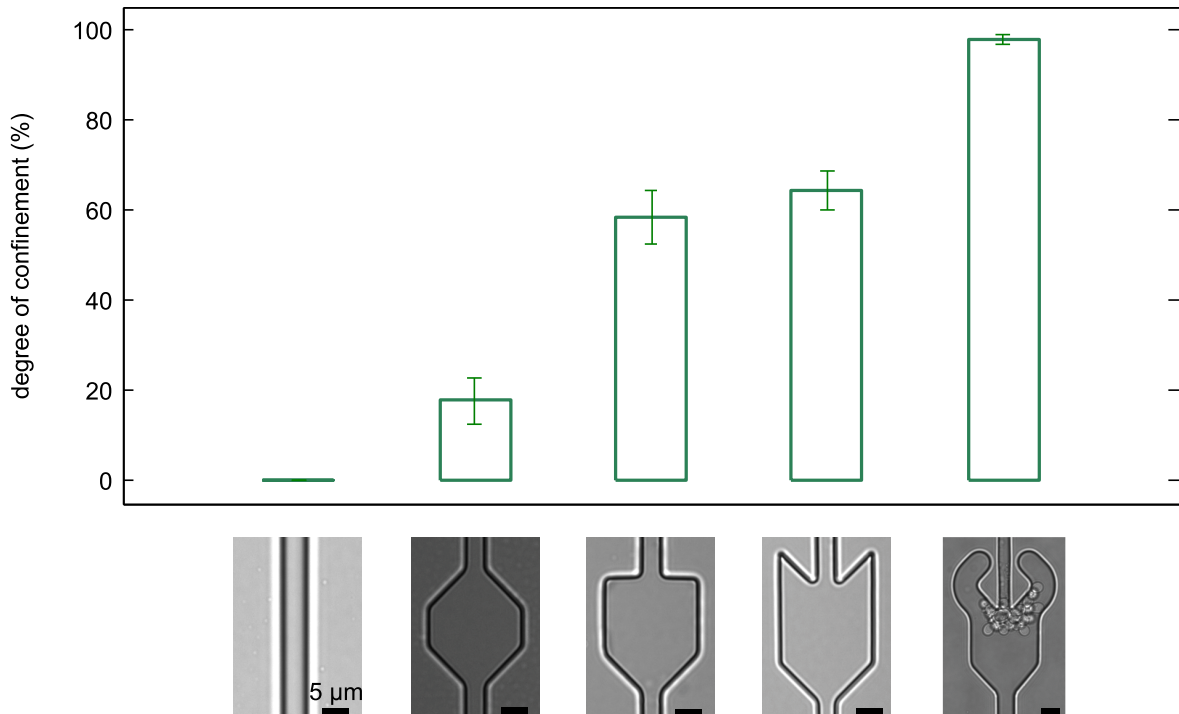

Figure 6.7: The degree of confinement is plotted for the various valves. The confinement becomes more efficient the larger the exit angle of the leaky valve is. The self-closing valve confines *S. cerevisiae* populations nearly completely.

Nutrient supply

We conducted several tests to elucidate the efficiency of the nutrient supply via nutrient channels into the growth chamber (see figure 5.16 in section 5.3.2 for an image of the corresponding device). We extracted the diffusion coefficient of glucose in the growth chamber when it is densely packed with cells. In CSM and YPD growth media glucose is the major source for ATP production in *S. cerevisiae* cells [98]. Consequentially, glucose limitation will have a pronounced impact on the growth of cells in our experiments. First, we let a cell population grow in a device with a self-closing valve until it reached a steady state. We exchange the growth medium (CSM) with a solution of 2-NBDG (a fluorescent D-glucose derivative [84]) and let the solution diffuse into the growth chamber.

In figure 6.8 fluorescent images (GFP) of a section of the growth chamber at different time points during diffusion of 2-NBDG are shown. We measured the fluorescent profile along the growth chamber at different time points and extracted the full width at half maximum (FWHM). Thus, we obtain a measure for the diffusion length of the fluorescent glucose. The FWHM is related to the standard deviation σ for a gaussian distribution by

$$\text{FWHM} = 2\sigma \sqrt{2 \cdot \ln 2}. \tag{6.3}$$

For a random walk in one dimension (which is analog to what we measure in the experiment) the standard deviation as a function of time is given by

$$\sigma^2 = 2Dt \tag{6.4}$$

with D being the diffusion coefficient. The relation between FWHM and diffusion coefficient is obtained by comparing equations (6.3) and (6.4)

$$\text{FWHM} = \sqrt{2 \cdot 4 \cdot 2 \cdot \ln 2} \cdot \sqrt{Dt}. \tag{6.5}$$

We fitted the data with a square root function in order to obtain the diffusion coefficient (see figure 6.9a)

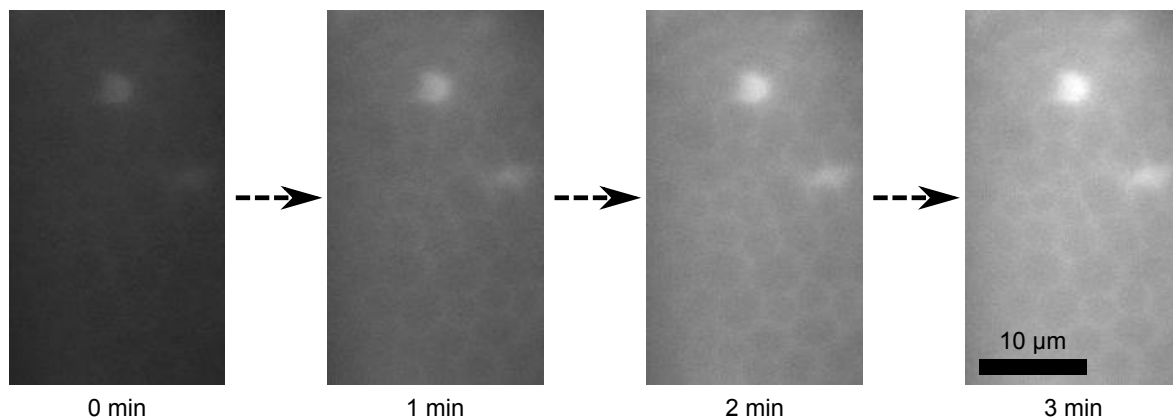$$D = 0.36 \pm 0.06 \; \frac{\mu m^2}{s}. \tag{6.6}$$

Figure 6.8: Fluorescent image series of a section of the growth chamber. The intensity increases with time, while the 2-NBDG (fluorescent glucose) diffuses into the growth chamber.

This diffusion coefficient is three orders of magnitude lower than the diffusion coefficient of glucose in free solution [99]. Furthermore, this value is a lower bound for diffusion of glucose into the growth chamber since the 2-NBDG molecules are larger than normal glucose molecules, hence they diffuse slower, and part of the fluorescence can be blocked by the tightly packed cells leading to a weaker fluorescent signal.

To estimate if cells have access to sufficient nutrients in the growth chamber we conducted finite element simulations (Comsol Muliphysics), in which we also incorporated the consumption of glucose by the cells. The fermentation yield of S. cerevisiae cells is 0.45 g of biomass / g consumed glucose [100]. If we assume that the cells in the densely packed case can still divide with the same doubling time of 2 hours as in the free solution case, the consumption rate of glucose is 4.6 $\frac{mol}{s}$[†].

We conducted two Comsol simulations with these parameters. In a first simulation we considered that glucose only diffuses into the growth chamber. We assumed a constant glucose concentration of C_0 at the sites where the nutrient channels are connected to the growth chamber. We depict the concentration of glucose normalized by C_0 in figure 6.9b. The concentration drops rapidly to zero due to the relatively high (compared to the diffusion coefficient) glucose consumption. In a second simulation we implemented a flow of glucose of 0.2 $\frac{nl}{s}$ into the model, which is the flow rate that is applied during the experiments. As can be seen in figure 6.9c the concentration of glucose does not drop below 99 %. This shows that nutrients are not a limiting factor in the growth of *S. cerevisiae* cells in the growth chamber even at high cell densities. For details about the Comsol simulation setup see section 4.4.

[†]The mass of a *S. cerevisiae* cell at the beginning of its first cell division is about 21.3 pg [101].
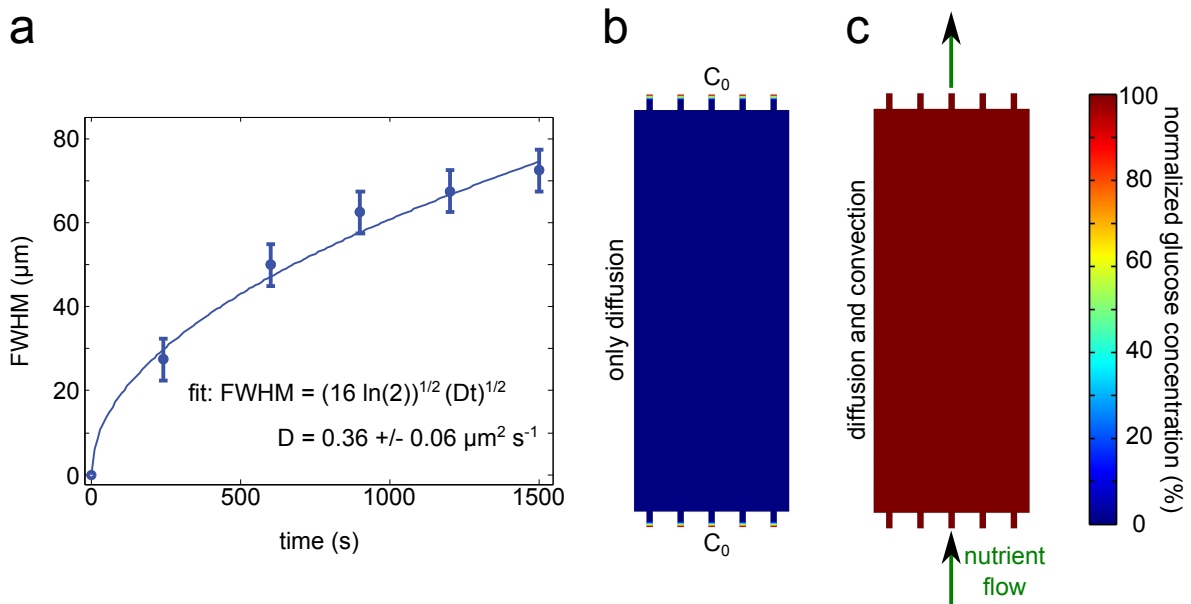

Figure 6.9: a) The diffusion coefficient of glucose was determined by fitting the FWHM of the intensity distribution along the growth chamber with a square root function. b+c) We conducted Comsol simulations of the concentration of glucose in the growth chamber. We also incorporated the consumption of glucose by the cells. b) Here, we only simulated diffusion of nutrients with the concentration at the nutrient channel inlets being fixed to C_0. c) We also implemented a flow of nutrients of 0.2 $\frac{nl}{s}$ similar to what we apply in the actual experiments.

Feedback algorithm

In the following we present the characterization of the pressure measurement via feedback algorithm. As described earlier (section 5.4) we measure growth-induced pressures exerted by cell populations either through the displacement of a 4 μm thick membrane, through the deformation of a channel or through balancing the displacement of the membrane by a feedback algorithm. This feedback algorithm is used to adjust the hydrostatic pressure in the control channel according to the membrane displacement.

In order to assess the capabilities of the feedback algorithm we impose a known hydrostatic pressure in the growth chamber. In doing so we can test how accurate the imposed pressure is mimicked by the feedback algorithm that controls the hydrostatic pressure in the control channel. The result of this test experiment is displayed in figure 6.10. As can be observed in the plot, the feedback pressure follows nicely the imposed pressure curve at least up to a pressure increase of 1 MPa/h. To relate this value to our experiments we calculate the maximal increase in pressure we can expect. The turgor pressure divided by the doubling time of *S. cerevisiae* [102, 103] is a decent estimate for this. For this fraction we obtain a value of 0.5 MPa/h. This value is only half as high as the maximal value that can be measured with our feedback algorithm. We also observe sudden drops in pressure in our experiments conducted with leaky valves. The feedback algorithm is not always able to follow these sudden drops, hence a measurement of the growth-induced pressure via the displacement of the membrane without applying the feedback algorithm is more suited to study the pressure drops we observe. Due to the linear relationship between pressure and
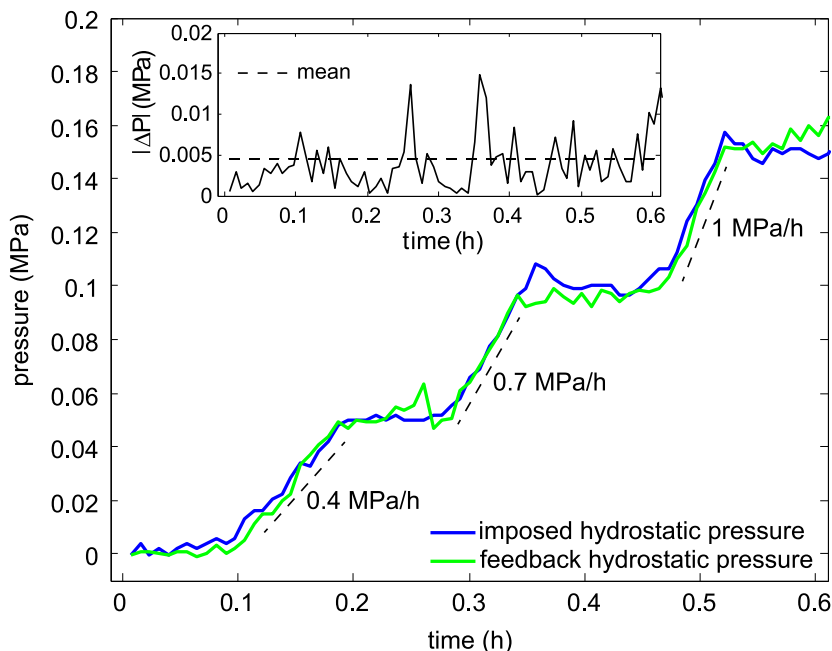

Figure 6.10: Result of feedback algorithm performance test. A known pressure was imposed onto the membrane and the feedback mimicked this imposed pressure. The inset shows the difference between the pressures in growth chamber and control channel. The mean of the difference is taken as an estimate for the error of the pressure measurement technique.

membrane displacement (cf figure 4.9d) it is sufficient to test the pressure regime shown in figure 6.10. Additionally, we cannot only measure the absolute pressure in the growth chamber but also relative changes in pressure difference between growth chamber and control channel by using the feedback algorithm. To do so, we only have to choose the default position of the membrane accordingly. For instance if we measure and set the default membrane position when a pressure of 0.2 MPa is acting in the growth chamber while the hydrostatic pressure in the control channel is zero, the feedback algorithm will balance the membrane displacement in a way that this pressure difference of 0.2 MPa is maintained. The inset in figure 6.10 illustrates a quantification of the error of the pressure measurement. We calculate the difference between imposed and feedback pressure and take the mean value as an estimate for the error of the pressure measurement. The error is equal to about 0.005 MPa.

6.2.2 Pressure curves in microfluidic experiments

In this section pressure curves acquired with the various devices are presented. If not mentioned otherwise the experiments were conducted with the lab strain S288c in CSM medium.

Active valves

First, we compare our two active valve devices (Abate, Quake valves). The result of the pressure measurement for the Abate valve device is presented in figure 6.11. In each step the Abate valve pressure was kept constant for about 10 hours (except for the first and last step) before being increased in steps of 0.05 MPa. The growth-induced pressure increases with the Abate valve pressure. The growth-induced pressure only adapts to the valve pressure after a few hours.

Furthermore, we measured the growth-induced pressure from the displacement of the membrane as a function of time for the Quake valve device. We used a different PDMS mixing ratio of base to curing agent (15:1 instead of 10:1) for this device as described in section 3.1.3. Since we did not conduct a calibration measurement for this mixing ratio, we could only estimate the Young's modulus of the corresponding PDMS device. Wilder *et al.* measured the Young's modulus of PDMS at different mixing ratios [104]. They obtained a Young's modulus of about 0.88 MPa for a base to curing agent ratio of 15:1, which is the value we used for our further analysis. Notably, they measured the Young's modulus of PDMS prepared at a mixing ratio of 10:1 to be about 1.7 MPa, which is equal to what we obtained for our 10:1 PDMS devices (cf section 5.4.3). The growth-induced pressure rises with the Quake valve pressure as can be observed in figure 6.12.

The growth-induced pressure is less compliant to the valve pressure in the case of the Quake valve. We plotted the growth-induced pressure as a function of the valve pressure for both devices in figure 6.13a. The Quake valve device differs in one important aspect from the Abate valve device (apart from the valve itself) as is indicated in figures 6.13b and 6.13c. The Quake valve device is an older design, in which nutrient slits were incorporated. Cells can readily escape through the nutrient slits, while the narrow (1 µm wide and 0.5 µm high) nutrient channels (used in the Abate valve device) are nearly impassable for the *S. cerevisiae* cells. In the Quake valve experiment we observed that cells escaped through the nutrient slits for valve pressures higher than 0.2 MPa. This hints at the importance of the development of the nutrient channels as a reliable way to feed the population.
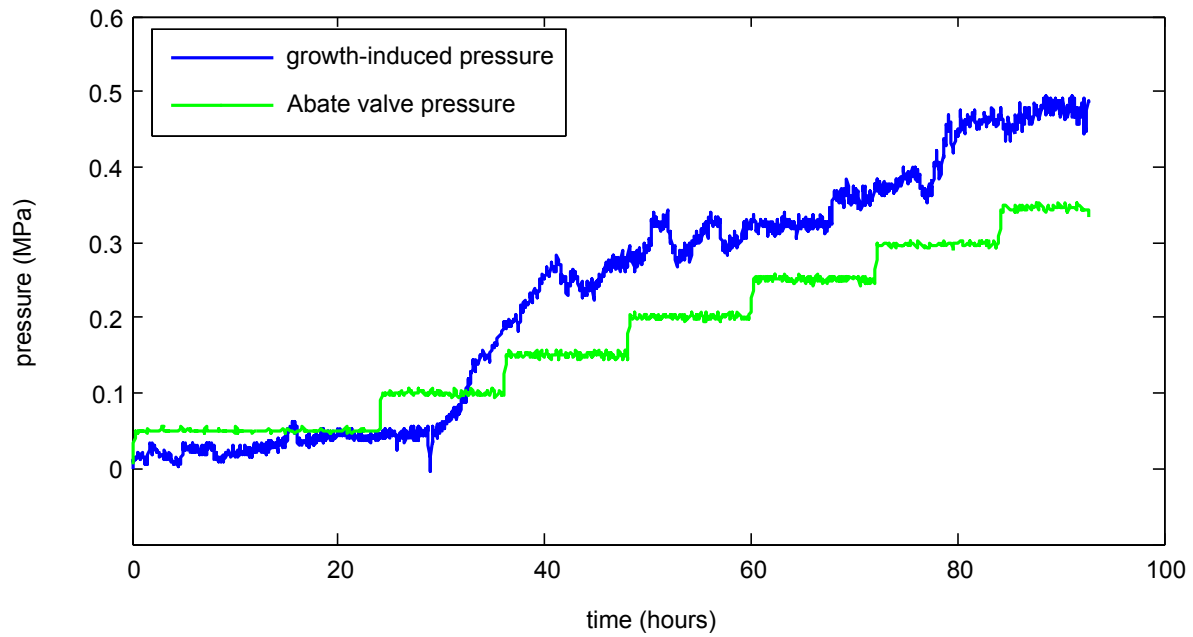
Figure 6.11: The growth-induced and the Abate valve pressure are plotted as a function of time. The growth-induced pressure rises with the valve pressure.
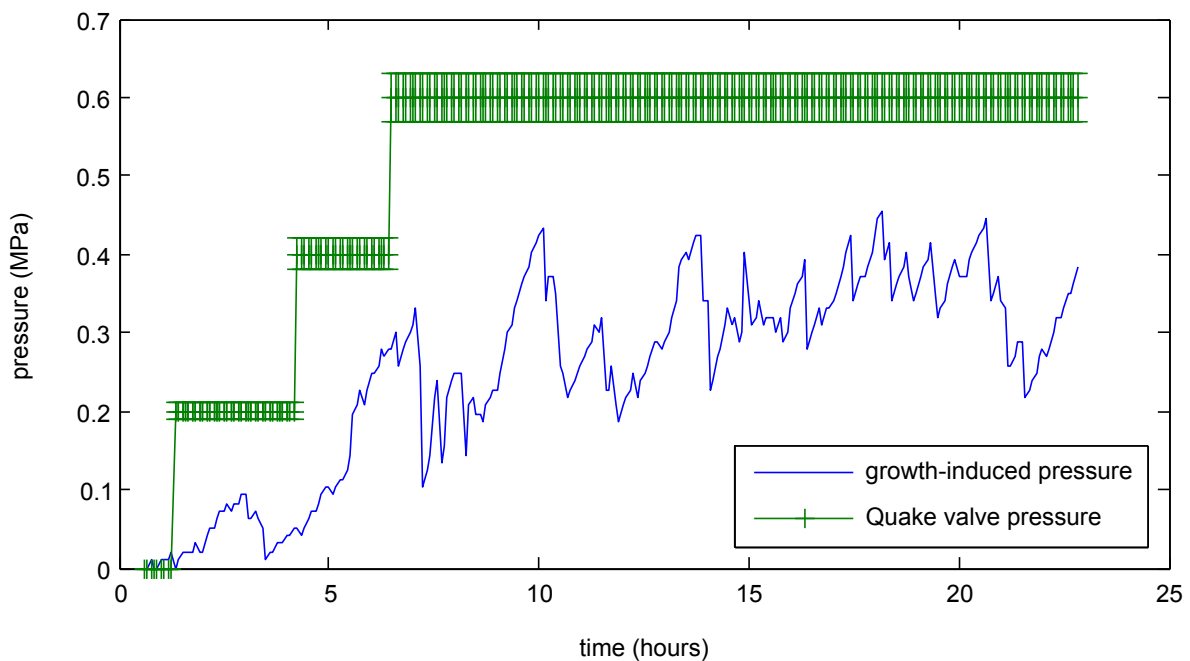

Figure 6.12: The growth-induced and the Quake valve pressure are plotted as a function of time. The growth-induced pressure rises with the valve pressure.
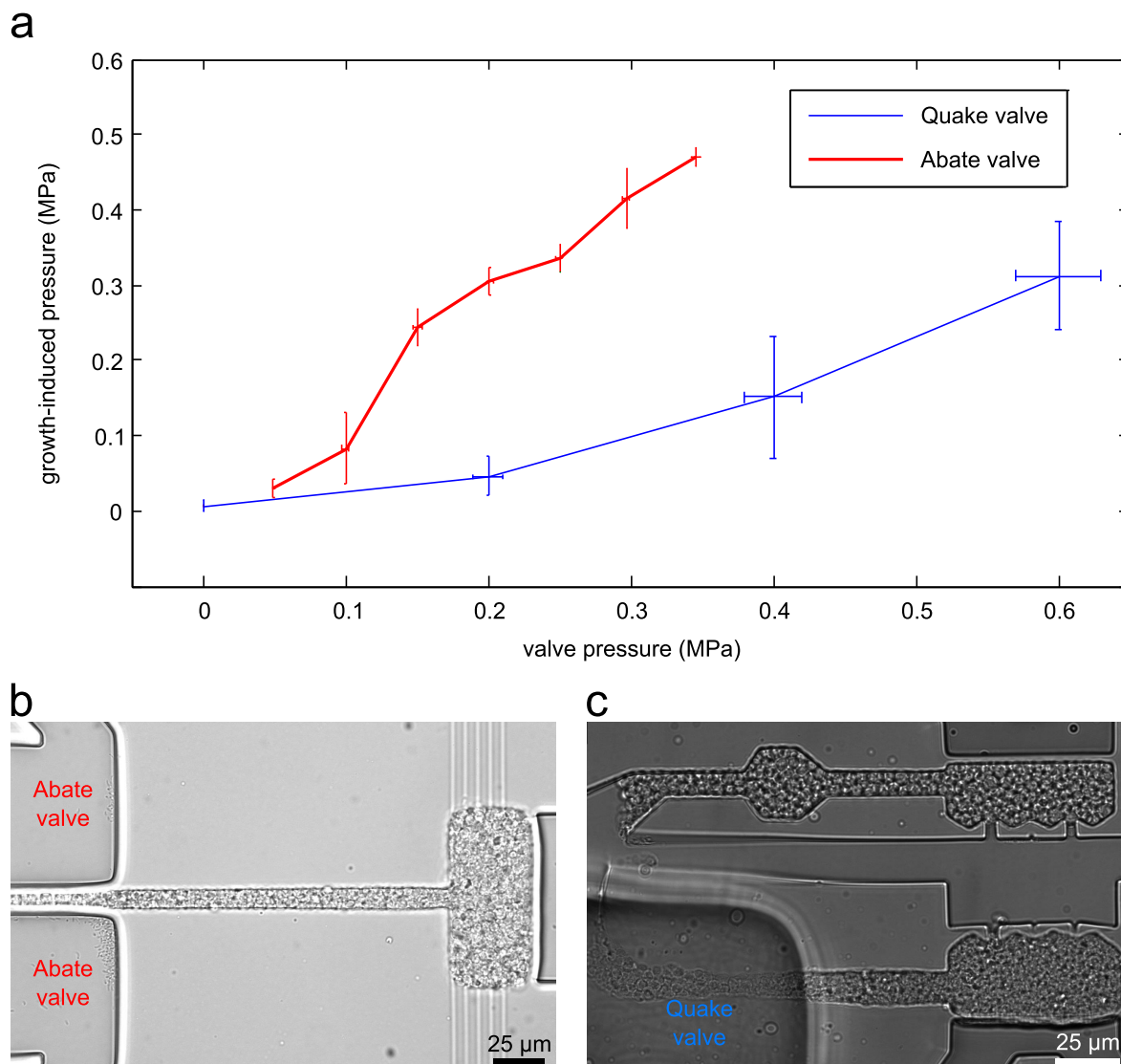
Figure 6.13: a) A comparison of the two active valve devices (Abate and Quake valve) is shown, in which growth-induced pressure is plotted as a function of the valve pressure. b) The Abate valve design is shown. The cells are fed through nutrient channels. c) The Quake valve design is displayed. In this device nutrients are supplied via nutrient slits, which provides the cells another way to escape the growth chamber.

Passive valves with nutrient channels

Figure 6.14 illustrates the pressure curves recorded for the nutrient channel devices. The data for each individual valve are displayed as data range plots. The shaded area for each color represents the extension from minimal to maximal pressure value with respect to all experiments conducted with the same valve. Furthermore, for each valve one exemplary pressure curve is plotted as a thick line. The starting time for the experiments can be chosen arbitrarily, so that the pressure curves for different valves have been shifted in time for better visibility. The beginning of each pressure curve marks the first time point when growth chamber, valve and channel in between were completely filled with cells.

The experiments conducted with the self-closing valve reach a maximum in growth-induced pressure of about 1.0 MPa. One of the self-closing valve experiments showed a faster increase in pressure in the beginning (indicated by the red shaded region). Unfortunately, this experiment could only be recorded for 17 hours due to a loss of focus, which rendered the pressure measurement unreliable. The growth-induced pressure in the 135° leaky valve devices reached maximal values between 0.6 and 0.7 MPa. In one of the 90° valve experiments the pressure rose up to over 0.5 MPa, while the other experiments with this valve only reached maximal pressures of about 0.4 MPa. The 45° valve experiment resulted in a maximal growth-induced pressure of about 0.2 MPa. Additionally, in the plain 5 µm channel device the pressure did not increase to more than 0.01 MPa.

Passive valves with nutrient slits

The corresponding pressure curves for the nutrient slit device are shown in figure 6.15. The device with the plain 5 µm channel also reaches pressure values that only fluctuate between 0 and 0.01 MPa. The curves for the 45° and 90° valves reach lower pressures (about 0.1 and 0.2 MPa respectively) as the corresponding pressure curves for the nutrient channel device (cf figure 6.14). This finding might be explained by the fact that cells tend to escape through the nutrient slits but not through the nutrient channels as described in section 5.3.2. Interestingly, the pressure curves for the 135° valve device show a different picture. The variance of pressure values is particularly high. In one of the experiments the growth-induced pressure hardly reaches 0.4 MPa (lower bound of shaded area), while in two experiments the maximal growth-induced pressure is about 0.8 MPa. This exceeds the pressure values obtained in the experiments conducted with the nutrient channel device that also contain a 135° valve. This finding is counterintuitive since the maximal growth-induced pressure reached in these experiments should be lower compared to the nutrient channel device due to the nutrient slits that provide another escape route for the cells (when using the same valve).

A possible explanation for this paradox is that the valves do not function in the same way for the nutrient slit and nutrient channel devices. In the nutrient slit experiments that reach growth-induced pressure of about 0.8 MPa, the 135° valve tends to behave like a self-closing valve, which is displayed in figure 6.16. At the exit of the valve, which is indicated by the arrows the growth-induced pressure exerted onto the valve walls results in a narrowing of the exit channel. We did not observe this behavior in any of the experiments conducted with the nutrient channel device.

It remains to be explained why the same valve behaves differently in the two devices. The most obvious difference is the way nutrients are supplied to the cells. We conducted a Comsol simulation to elucidate the concentration of nutrients in the channel next to the growth chamber under real experimental conditions. A flow of nutrients is applied through
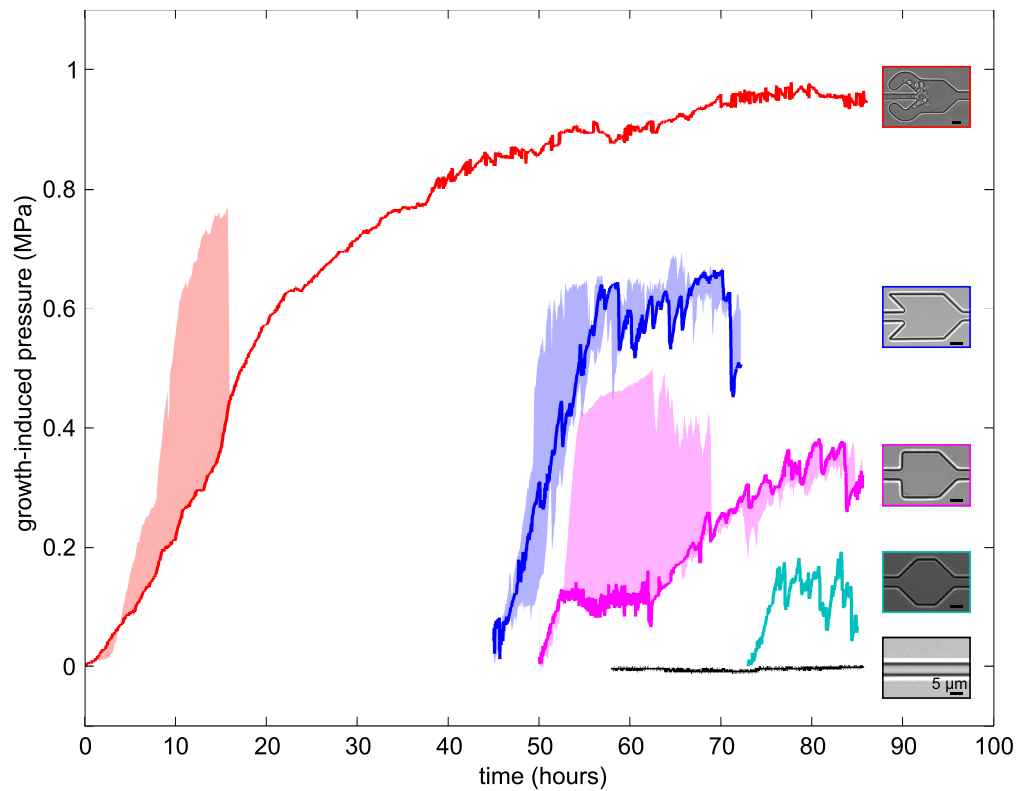
Figure 6.14: The pressure curves for the nutrient channel device are plotted in this figure. The different curves for the same valve have been plotted in terms of their data range. At each time point the maximal and minimal pressure values are shown by the shaded region. The solid line shows one exemplary pressure curve for each valve. The curves for different valves have been shifted in time to visualize them better. The time point, at which the curves start, is equal to the beginning of growth-induced pressure increase, when the device is completely filled with cells for the first time.
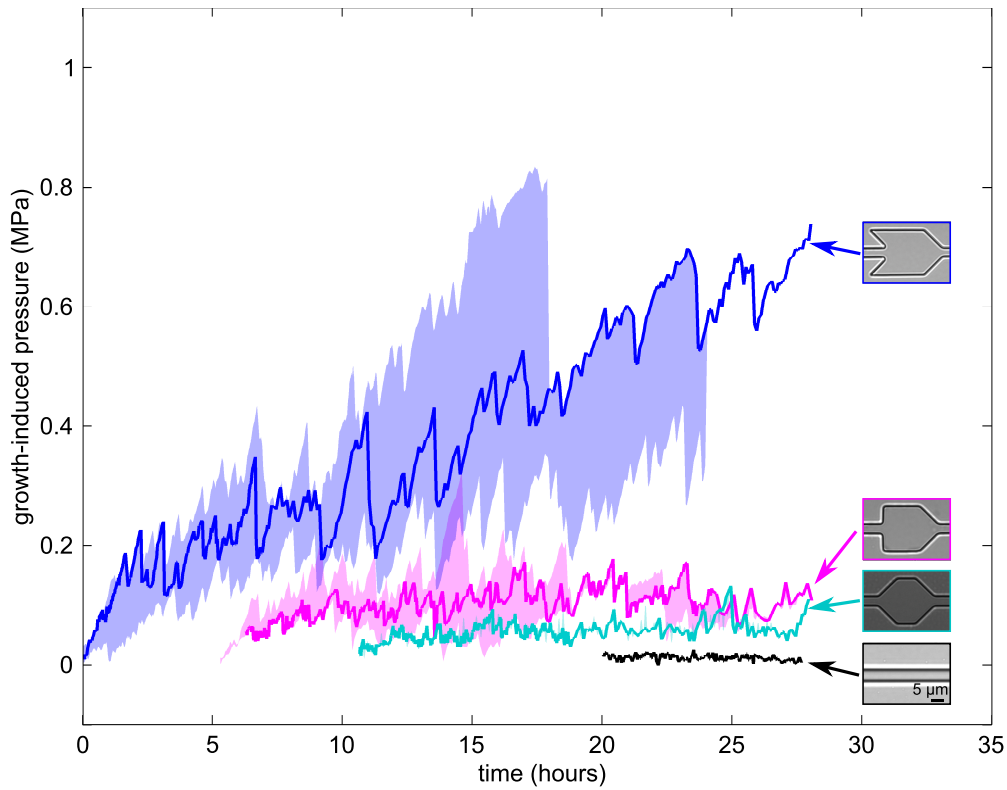
Figure 6.15: The pressure curves for the nutrient slit device are plotted in this figure. The different curves for the same valve have been plotted in terms of their data range. At each time point the maximal and minimal pressure values of all curves are shown by the shaded region. The solid line shows one exemplary pressure curve for each valve. The curves for different valves have been shifted in time to visualize them better. The time point, at which the curves start, is equal to the beginning of growth-induced pressure increase, when the device is completely filled with cells for the first time.
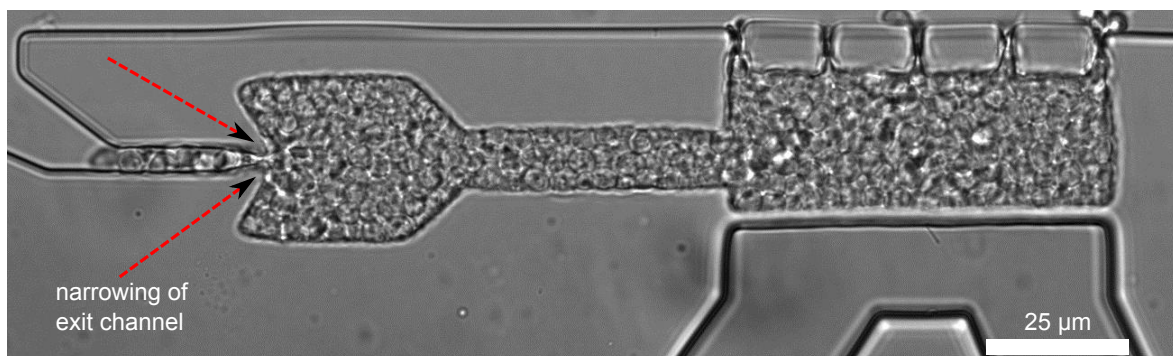

Figure 6.16: A picture in the late stages of an experiment conducted with a nutrient slit device is shown. The tightening of the exit channels is indicated. The narrowing for this type of leaky valve only occurs when using the nutrient slit device.

the nutrient channels and the cells consume the nutrients (cf section 6.2.1). The result is displayed in figure 6.17. We observe that the nutrient concentration drops to zero in the channel after about 23 µm. In the actual device the valve is positioned about 35 µm apart from the growth chamber, so that it is reasonable to assume that the cells in the valve do not have access to sufficient nutrients in order to proliferate. We conclude that in order for the 135° valve to partly function as a self-closing valve the cells need to be growing in the valve itself and not only being pushed towards the exit channel by the proliferating cells in the growth chamber[‡].
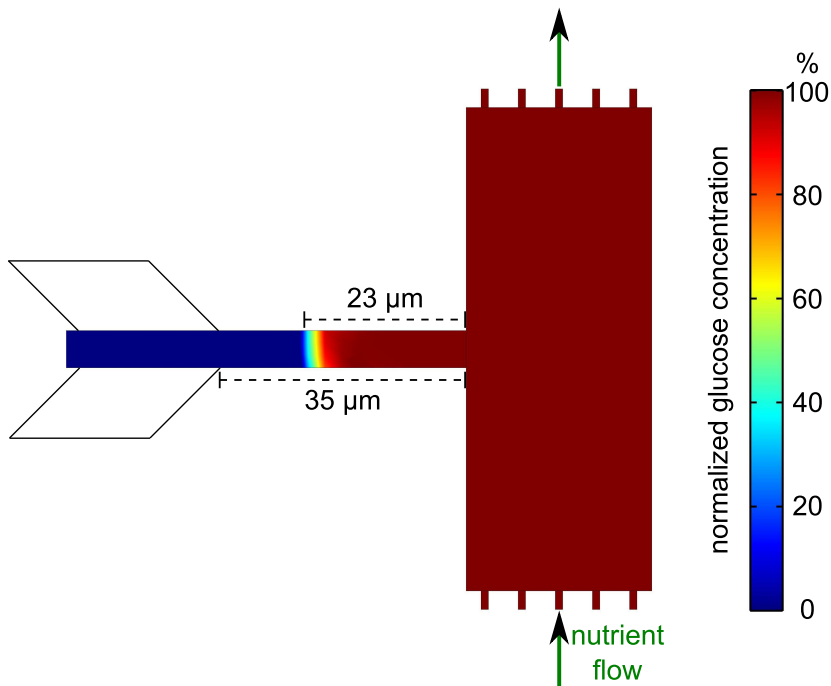

Figure 6.17: Result of a Comsol simulation of the nutrient channel device, in which the adjacent channel was incorporated. The normalized glucose concentration is shown with the nutrient concentration dropping to zero after about 23 µm along the channel. In the microfluidic device the valve is positioned 35 µm away from the growth chamber. No nutrients reach the cells in the valve. The position of the valve is only indicated in the figure and has not been incorporated in the Comsol simulation since the Comsol version (4.0) accessible in our institute was not able to find a solution for this slightly more complicated model.

Influence of channel width

In figure 6.18a two pressure curves are shown that were recorded in the same device with lab strain S288c yeasts. Figure 6.18b shows an image of the experiment just before the cells completely fill the 135° valves. The channels connected to the valves and growth chambers are 7.5 µm and 5 µm wide for the upper and lower part of the device, respectively. The

---

[‡]Notably, we could not simulate the nutrient concentration in the nutrient slit device, since the Comsol version available in our institute (version 4.0) is incapable of finding a solution for this more complicated model.
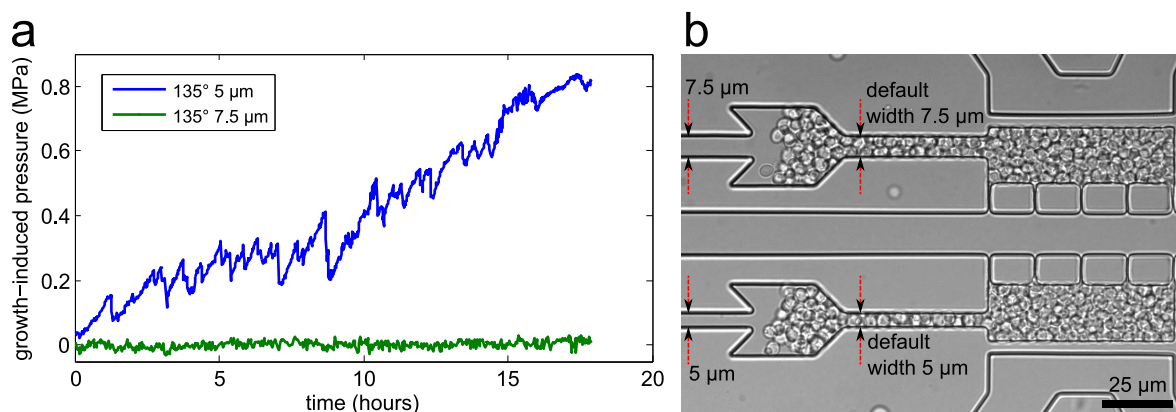
Figure 6.18: a) Comparison of the growth-induced pressure curves that result from different channel widths. b) Micrograph of the device, in which the upper part has a channel width of 7.5 µm and the lower part a channel width of 5 µm.

pressure curve for the 7.5 µm wide channel fluctuates between small pressure values of 0 and 0.03 MPa, while the pressure curve of the 5 µm wide channel behaves as shown before. For all experiments with any of the leaky valves the pressure curves for the 7.5 µm wide channels hardly show any pressure buildup. This indicates that the width and probably the more general value of the cross section of the exit channel determines if cell clots can form and how easy these clots are dissolved.

Influence of cell adhesion

We conducted an experiment with the undomesticated yeast strain (BR-F) in the self-closing device. The pressure curve is plotted together with the corresponding result for the lab strain S288c in figure 6.19a. As mentioned before (section 3.2) the difference between the two strains is that the cells of the undomesticated strain express proteins involved in cell adhesion that are not expressed in the lab strain. In a confined space these two strains behave differently, as can be observed in figures 6.19b and 6.19c. The lab strain cells fill every available space before any increase in pressure can be observed (figure 6.19c). The undomesticated cells cannot rearrange that easily due to the strong cell-cell bonds, as can be seen in figure 6.19b. The channels are strongly deformed before the cells even reach the membrane in the growth chamber. The pressure curve of the undomesticated strain shows a very fast increase of about 0.2 MPa/h where the pressure is increasing from 0.3 MPa to 0.95 MPa in about 3.3 hours. This slope is unmatched in magnitude by any other experiment we conducted. The undomesticated strain reaches a higher maximal pressure of 1.2 MPa, which is about 20% higher than the corresponding value for the lab strain. More replicates for both strains are required to determine if this difference is only due to sample variation.

6.2.3 Cell avalanche statistics

The pressure curves corresponding to the leaky valve devices usually show an intermittent behavior as can be seen in figures 6.14 and 6.15. The growth-induced pressure suddenly drops and starts to rise again. This intermittency is a result of the interplay between formation of cell clots at the exit channels (or nutrient slits in the corresponding devices) and cell
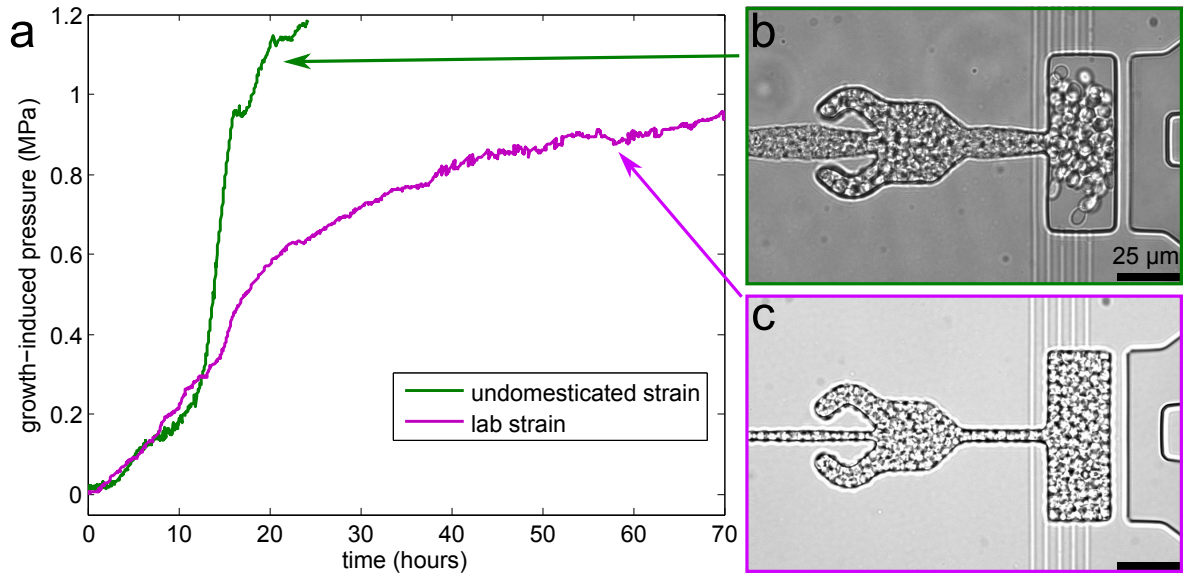
Figure 6.19: a) Comparison of the pressure curves measure for the undomesticated (BR-F) and the lab yeast strain (S288c). b) Image of a self-closing valve device filled with the undomesticated strain. c) A self-closing valve device is shown with lab strain cells inside.

avalanches, which occur when cell clots get dissolved. A cell clot dissolves when the growth-induced pressure increases to such an extent that frictional forces between neighboring cells (or between cells and the surrounding PDMS) are overcome [60]. When cells escape via avalanches, the cell density and hence the growth-induced pressure decrease rapidly inside of the growth chamber. However, when a clot forms the density and consequentially the growth-induced pressure in the growth chamber increase due to cell proliferation. In order to provide evidence for this interpretation we plotted the pressure curve of one experiment (90° leaky valve with nutrient channels) together with the cell velocity in the exit channel on the same axis in figure 6.20. One can observe that large pressure drops usually coincide with high cell velocities, which implies that pressure drops are caused by cell avalanches.

In order to extract statistical properties from the pressure curves we measure pressure drops Δp and survival times of the cell clots τ from the data as indicated in figure 6.20. We defined a threshold of $\Delta p \geq 0.02$ MPa in order to distinguish pressure drops from the noise in the pressure measurement. The survival functions for both properties (Δp and τ) for each device were calculated separately. Details about the survival function are presented in section 4.5.2. In short, the survival function $S(P \geq \Delta p)$ for the pressure drops describes the probability to find a pressure drop P in the data that is greater or equal to Δp.

Pressure drops due to cell avalanches

The pressure drop survival functions $S(P \geq \Delta p)$ for four of the leaky valve devices[§] (135° valve with nutrient slits, 90° valve with nutrient slits, 135° valve with nutrient channels and 90° valve with nutrient channels) are displayed in figure 6.21. The probability to find large pressure drops is higher in devices, which feature 135° valves than those that contain 90°

[§]We incorporated the data from all the conducted experiments for a given valve in this plot. We did not include the 45° leaky valve due to the relative small statistics we have for these devices.
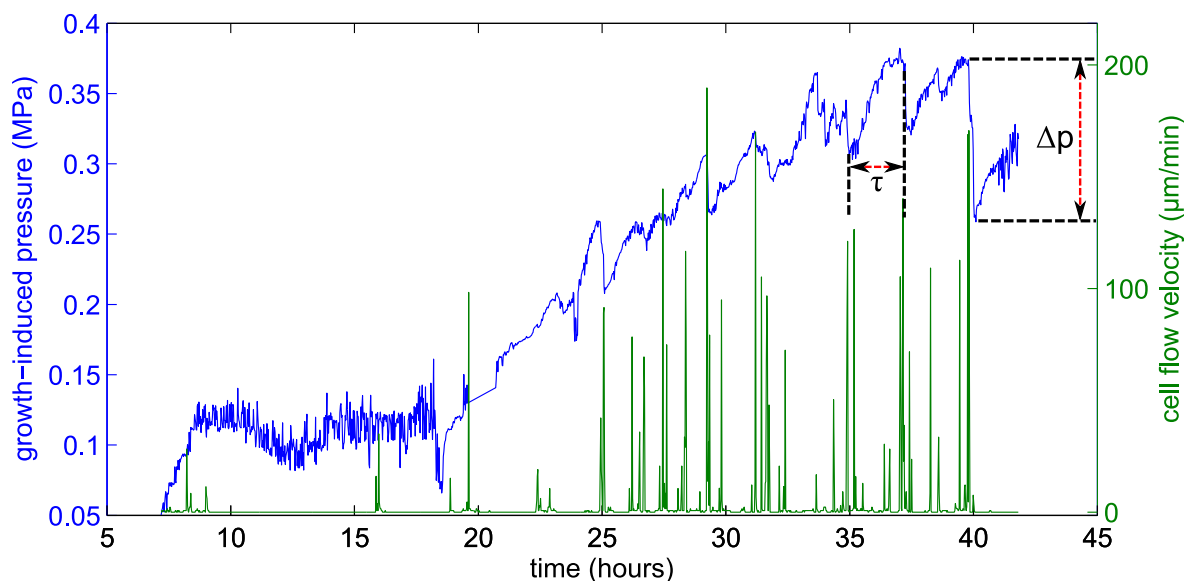
Figure 6.20: The growth-induced pressure is plotted together with the cell velocity in the exit channel for a 90° leaky valve device. High velocities usually coincide with large pressure drops. The definitions of the statistical parameters pressure drop Δp and survival time τ are indicated on the pressure curve.

valves when considering the two nutrient supply methods separately (cf ◇ to □ and + to ○). This result coincides with the observation that growth-induced pressures are typically higher for the 135° valves (figures 6.14 and 6.15). When comparing the survival functions for different nutrient supply methods, it can be observed that the nutrient slit devices show more of the higher pressure drops than the nutrient channel devices for a given valve (cf ◇ to + and □ to ○). Interestingly, the survival functions for the 135° valve nutrient channel device (+) and the 90° valve nutrient slits device (□) coincide, although the absolute pressure values are significantly higher for the 135° nutrient channel device (maximum of about 0.6 MPa compared to 0.15 MPa as shown in figures 6.14 and 6.15, respectively). This leads to the possible interpretations that cell avalanches occurring at the nutrient slits let more cells escape or that cell avalanches at either end (valve or nutrient slit) can promote another cell avalanche at another site due to rearrangements inside of the cell population. Such subsequent cell avalanches might occur between two image acquisitions so that they cannot be observed in the pressure curves.

Survival times of cell clots

In figure 6.22 the survival functions for the survival times are plotted. The probability to observe cell clots that are sustained for more than 0.7 hours is higher for the nutrient channel devices. This implies that cell avalanches are more frequent in the nutrient slit devices as is expected due to the additional escape routes the slits provide.

Furthermore, we analyzed the tails of the survival functions to further characterize statistical behaviors of the cell avalanches. In other intermittent flows it has been shown that the tails of the probability density functions of the survival times follow power-law decays [58, 90, 91]. Clauset *et al.* provide a powerful Matlab program to analyze power-law distri-
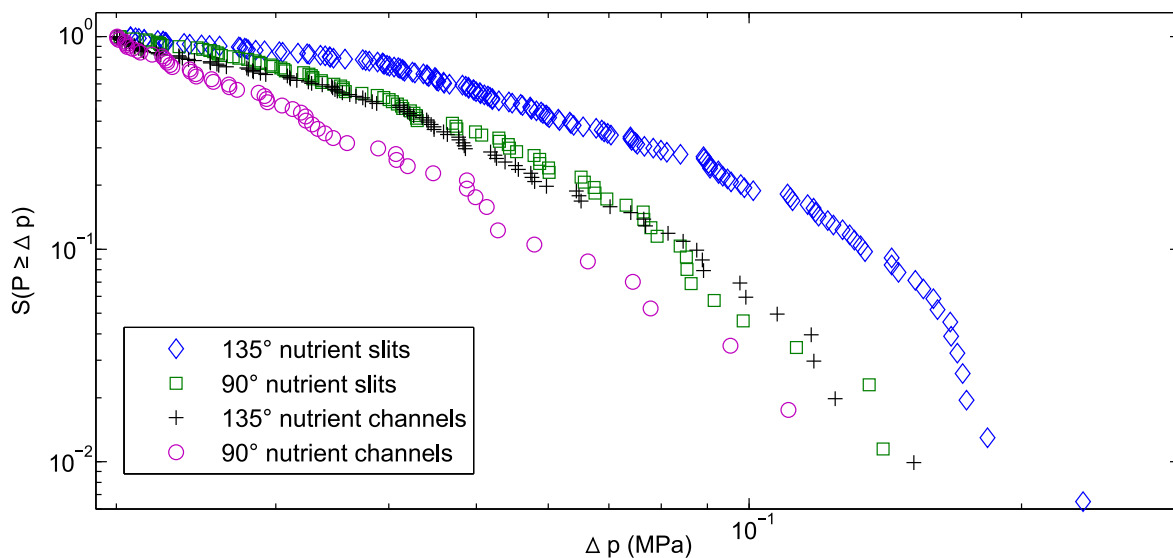
Figure 6.21: Survival functions of the pressure drops that occur due to cell avalanches are plotted for four devices. The data from all experiments conducted with the same device are combined.
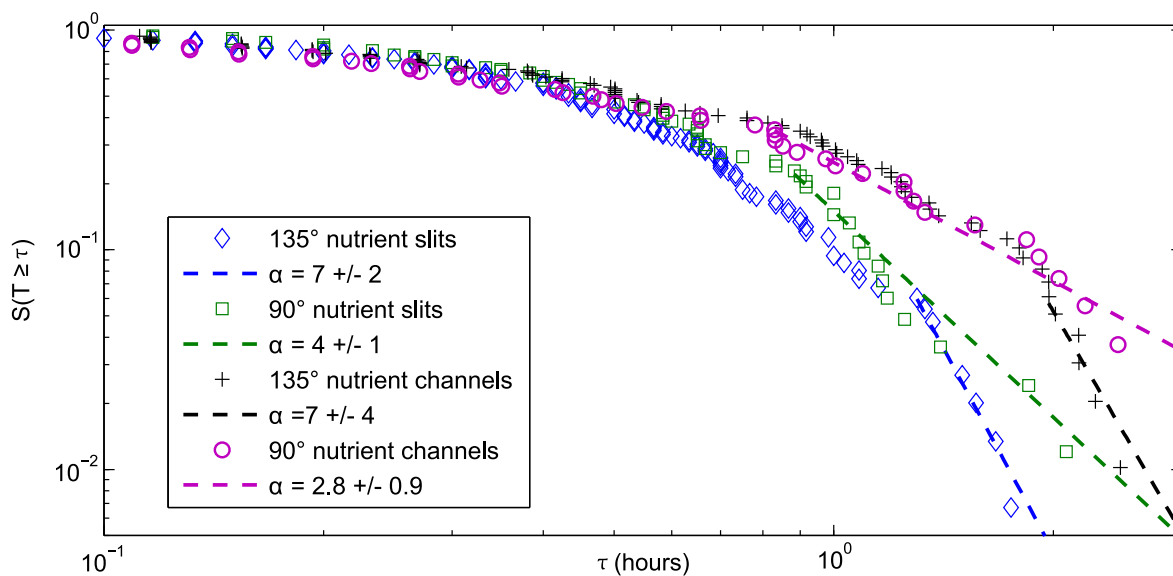

Figure 6.22: Survival functions of the survival times of the cell clots (= time between cell avalanches) are plotted for four devices. The data from all experiments conducted with the same device are combined.

butions in empirical data [105], which we also applied to our data. The program rigorously calculates the value $\tau_{\min}$, from which on the distribution follows a power-law decay by fitting a power-law decay to a range of $\tau_{\min}^{\text{test}}$ values and selecting the best fit from these values.

If we assume that the probability density function follows a power-law decay for $t \geq \tau_{\min}$

$$f(t) \propto t^{-\alpha}, \tag{6.7}$$

the survival function behaves as

$$S(T \geq \tau) \propto \tau^{-\alpha+1} \tag{6.8}$$

for $\tau \geq \tau_{\min}$, which we derive in section 4.5.2. Notably, the power-law decay fits in figure 6.22 have slopes of $-\alpha + 1$ and we prompt the α values in the figure legends analog to [58].

These α values enable us to further describe the cell flow behavior. Zuriguel *et al.* [58] proposed a flowing parameter Φ to describe systems consisting of granular particles that flow through orifices. The flowing parameter is defined as

$$\Phi := \frac{<t_a>}{<t_a> + <t_c>} \tag{6.9}$$

with $<t_a>$ being the average duration of the cell avalanches and $<t_c>$ being the average survival time of the cell clots. Cell avalanches have a finite average size and hence a finite duration $<t_a>$ as described by Zuriguel *et al.* [58]. In a system without cell clots $<t_c> = 0$ a continuous flow is observed and the flowing parameter assumes a value of 1. Intermittent flows are present for a finite average survival time so that $0 < \Phi < 1$, while in a totally clogged system the average survival time $<t_c>$ diverges and hence $\Phi = 0$. When looking at empirical experiments it is impossible to calculate an infinite average survival time $<t_c>$ from the data due to the inherent finite number of the acquired data points. As a consequence the power-law decay exponents need to be taken into account since the values for α determine if the average survival time diverges. We can calculate the average clogging duration $<t_c>$ from the probability density function $f(t)$ via

$$<t_c> \quad = \quad \int_0^\infty f(t) \cdot t \; dt \tag{6.10}$$

$$= \quad \underbrace{\int_0^{\tau_{\min}} f(t) \cdot t \; dt}_{=\text{ constant }=\; C \geq 0} + \beta \int_{\tau_{\min}}^\infty t \cdot t^{-\alpha} \; dt \tag{6.11}$$

$$= \quad C + \beta \int_{\tau_{\min}}^\infty t^{-\alpha+1} \; dt \tag{6.12}$$

with β being a normalization constant. The remaining integral diverges for $\alpha \leq 2$ and converges for $\alpha > 2$. In our experiments all α values are greater than 2 indicating that our systems are not completely clogged. We calculate the Φ values for the four different devices from our empirical data. The results are shown in table 6.1 together with the α values, $\tau_{\min}$ values and the total number of avalanches for each device. The Φ values are similar for all four devices, which indicates that the cell flow dynamics are comparable. Possibly, the overall cell flow behavior is largely determined by the width of the exit channel, which is identical for the four different devices.

Interestingly, the two survival functions for the 135° valves decay faster for large survival times. This shows that it is more probable that cell clots surviving for long times can be observed in the 90° valve experiments than in the 135° valve experiments. This is again a counter intuitive result since the 135° valve exhibit higher absolute growth-induced pressures.

Table 6.1: Flowing parameter Φ, slope of power-law decay α, minimal clogging duration for which the probability density function follows a power-law decay $\tau_{\min}$ and number of avalanches $N_{\text{avalanches}}$ for each of the four analyzed devices.

device	Φ	α	$\tau_{\min}$ (hours)	$N_{\text{avalanches}}$
135° nutrient slits	0.152(1)	7 ± 2	1.3 ± 0.8	150
90° nutrient slits	0.162(2)	4 ± 1	0.9 ± 0.2	84
135° nutrient channels	0.134(1)	7 ± 4	2.0 ± 0.8	99
90° nutrient channels	0.148(4)	2.8 ± 0.9	0.8 ± 0.4	55

6.2.4 Growth rate versus pressure

We describe the cell populations as fluid-like in order to extract the growth rate of the cells as a function of growth-induced pressure from the time lapse movies. We define the growth rate as

$$g := \frac{<v> \cdot A_{\text{channel}}}{V_{\text{chamber}}},\tag{6.13}$$

where $<v>$ is the mean velocity of the cells in the channel between growth chamber and valve, A_{channel} the cross section of this channel and V_{chamber} the volume of the growth chamber.

We measure the cell velocity between two subsequent images by means of PIV (for details see section 4.3). We choose a region of interest that is positioned around the channel as indicated by the dashed blue rectangle in figure 6.23a for the velocity measurement. We average the cell velocity over time intervals that correspond to certain growth-induced pressure ranges. Figure 6.23b shows a pressure curve recorded for a 90° valve experiment, in which the interval over which the average cell velocity is measured is indicated. The corresponding
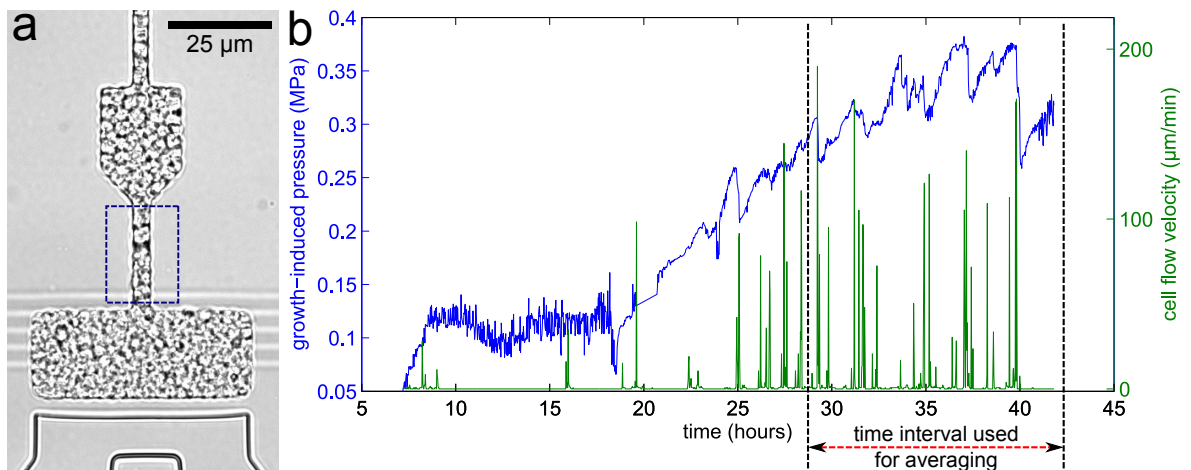

Figure 6.23: a) Image of a 90° valve device, in which the dashed blue rectangle indicates where the cell velocity is measured. b) The growth-induced pressure and cell velocity are plotted as functions of time on the same axis. The time interval over which cell velocity and growth-induced pressure were averaged for the growth rate measurement is indicated.

growth-induced pressure was also averaged over the same time interval.

As seen in section 6.2.3 we frequently observe cell avalanches in the experiments conducted with the leaky valve devices. These avalanches result in high cell flow velocities in the channel between growth chamber and valve. Since we are only interested in cell velocities, which result from the growth of the cells, we have to neglect high cell velocities corresponding to cell avalanches. We account for this by neglecting cell flow velocities higher than a threshold velocity $v_\text{threshold}$. This threshold is chosen according to the maximal theoretical cell velocity we expect to observe in the channel. In the zero pressure state the growth chamber has a volume of $65 \times 25 \times 10$ µm^3. If we assume that the chamber is completely filled, about 248 cells are present in the growth chamber (spherical cells with an average diameter of 5 µm). If all of these cells produce a daughter in a time interval of 2 hours (minimal doubling time in free solution) and the cell density in the growth chamber stays constant, cells are pushed out of the growth chamber with a velocity of about

$$v_\text{threshold} = \frac{1}{2} \cdot 248 \cdot 5 \text{ µm} \cdot \frac{1}{2 \text{ h}} = 310 \, \frac{\text{µm}}{\text{h}}. \tag{6.14}$$

The factor $1/2$ is taken into account since our devices have a structure height of about 10 µm, which implies that two cells with average diameter of 5 µm can move through the channel at the same time with one cell being on top of the other.

The channel cross section A_channel and the growth chamber volume V_chamber depend on the growth-induced pressure in the PDMS devices. We measure A_channel and V_chamber as functions of the growth-induced pressure in a Comsol simulation (details shown in section 4.4). We take these deformations into account when calculating the growth rate via equation (6.13).

The results of the growth rate analysis are displayed in figure 6.24, in which the growth rate is plotted as a function of the growth-induced pressure. When considering the errorbars, the growth rate seems to decay exponentially with increasing growth-induced pressure. This behavior can also be observed in the inset of figure 6.24, where we plotted the same data points on a semi-logarithmic scale.

6.2.5 Pressure versus G1 phase

As previously shown in section 6.2.4 an elevated growth-induced pressure results in a decreased growth rate. In this section we investigate if cells spend more time in the G1 phase of the cell cycle when the growth rate of the population is low. We conducted experiments with the Whi5-GFP yeast strain, for which we acquired fluorescent images. Yeast cells that have not committed to cell division have a high concentration of Whi5 proteins in their nuclei, which in the case of the Whi5-GFP strain results in a strong fluorescent signal from the nucleus [80] as indicated in figure 6.25a. When a cell passes the cell cycle checkpoint Start, it commits irreversibly to cell division. In order to pass this checkpoint a cell may require a certain size, sufficient nutrients need to be available and its DNA has to be intact [106–108]. Upon the initiation of Start the Whi5 proteins are excluded from the nucleus, which results in a diffusive cytosolic fluorescent signal in our Whi5-GFP strain [80] as shown in figure 6.25b.

In figure 6.25c the Whi5 nuclear density[¶] is plotted as a function of growth rate (the analysis for this particular plot was conducted by Dr. Morgan Delarue). The graph shows a linear relationship between growth rate and Whi5 nuclear density. A high anti-correlation
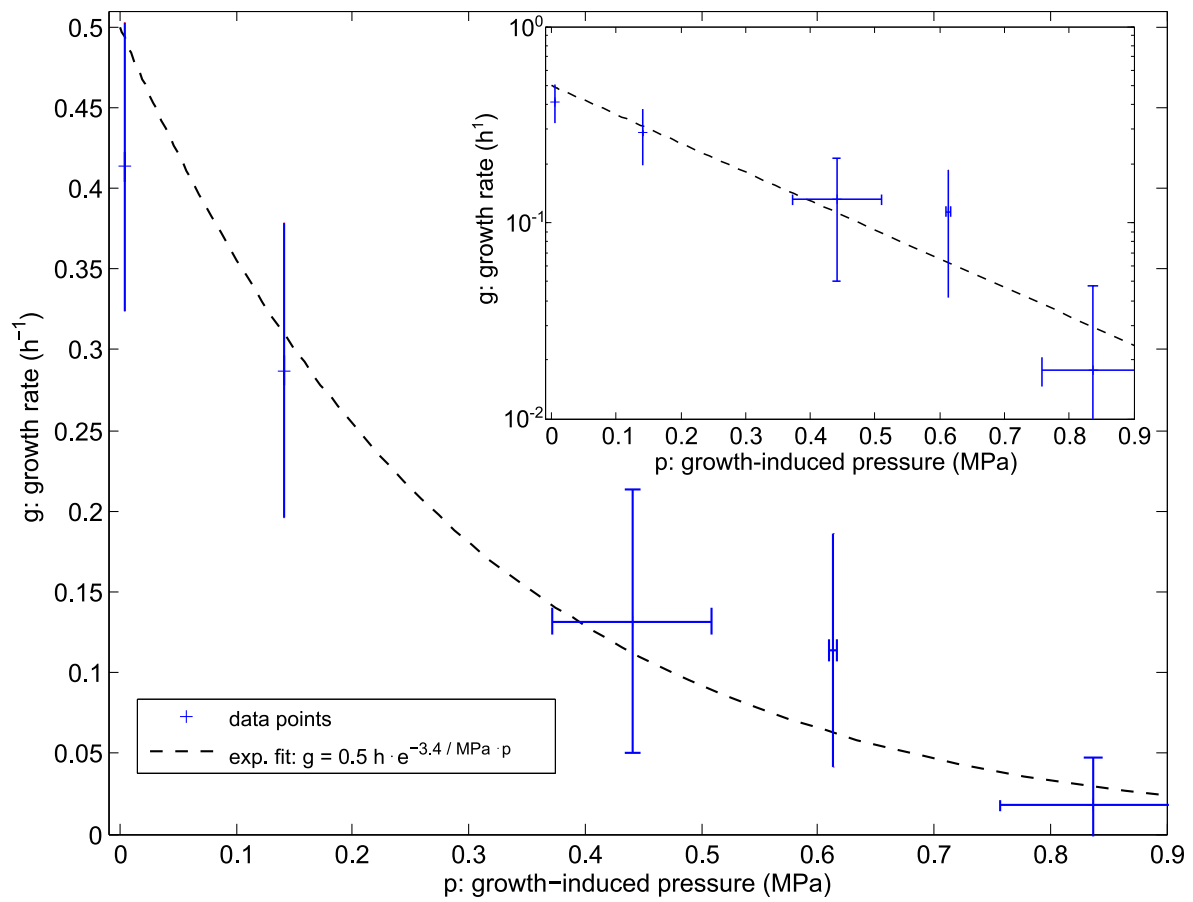

[¶]number of nuclei per unit area

Figure 6.24: The growth rate is plotted as a function of time. The data points follow an exponential decay. The inset shows the same data points plotted semi-logarithmically.

determined by a correlation coefficient of -0.988 for the data was derived. Hence, we conclude that the decrease in growth rate is intertwined with the amount of time cells spend in the G1 phase.
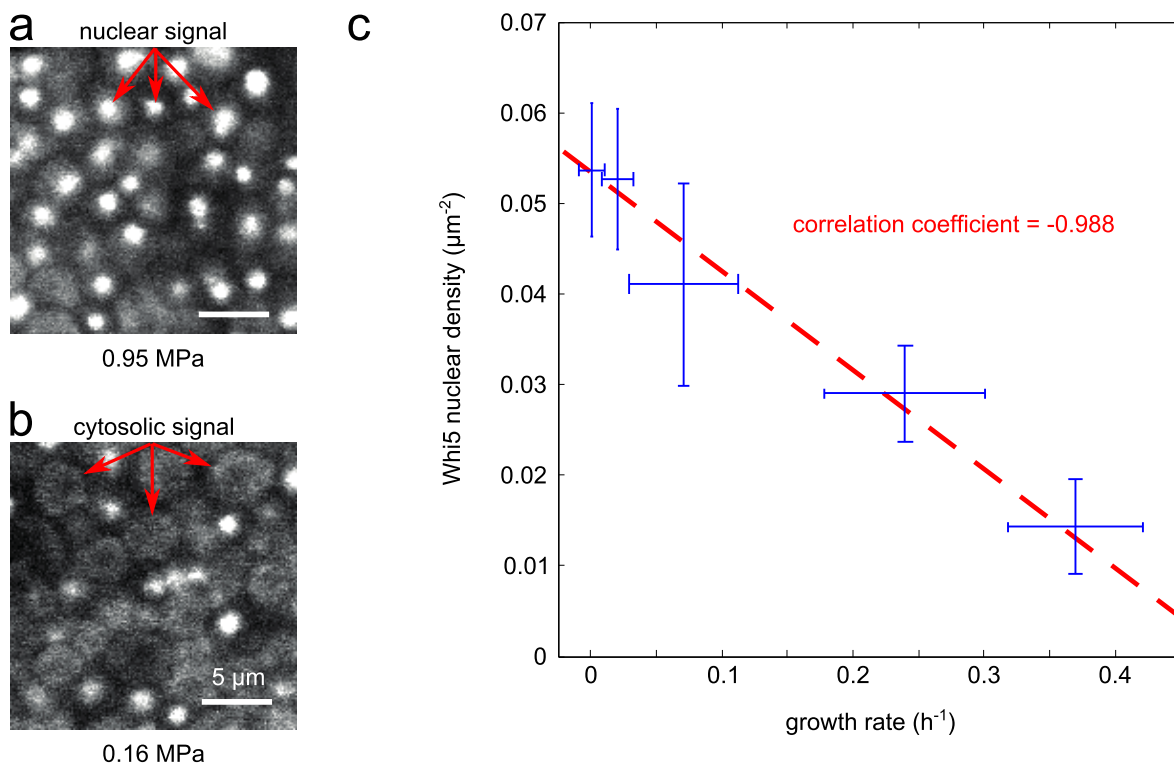

Figure 6.25: a) Fluorescent GFP image of a section of the growth chamber filled with Whi5-GFP yeast cells at a growth-induced pressure of 0.95 MPa. The bright dots indicate a high concentration of Whi5 proteins inside of the nuclei of the yeast cells, which labels these cells as being in the G1 phase of the cell cycle. b) Fluorescent GFP image of a section of the growth chamber filled with Whi5-GFP yeast cells at a growth-induced pressure of 0.16 MPa. The diffusive circular patches are cells, in which the Whi5 proteins were excreted from the nucleus, and thus were marked as having initiated their cell division. c) The Whi5 nulear density (number of cells in G1 phase per unit area) is plotted as a function of the growth rate. A correlation coefficient of -0.988 was calculated, which indicates a strong anti-correlation between the time cells spend in the G1 phase and the growth rate (The analysis for this particular plot was conducted by Dr. Morgan Delarue).

6.2.6   Pressure influences cell shape

We observed that *S. cerevisiae* cells possess different shapes when subjected to low or high growth-induced pressures, respectively.

Figure 6.26 shows a fluorescent image of one of our nutrient slit devices at the end of an experiment. The nutrient medium was replaced with a fluorescent glucose (2-NBDG) solution analog to section 6.2.1. We can nicely observe the cell shapes in this image since the boundaries between cells are highlighted by the fluorescent glucose. In this device the upper part of the device has a default exit channel width of 7.5 µm, while the exit channel in the lower part is 5 µm wide analog to the device shown in figure 6.18. Consequentially, the growth-induced pressure in the upper part is about 0.0 MPa, while a growth-induced pressure of about 0.4 MPa is found in the lower part. The cells that experience a low growth-induced pressure in the upper growth chamber are mostly oval in shape. The cells subjected to a high growth-induced pressure in the lower growth chamber on the other hand assume polygonal shapes where the contact area between adjacent cells is increased.
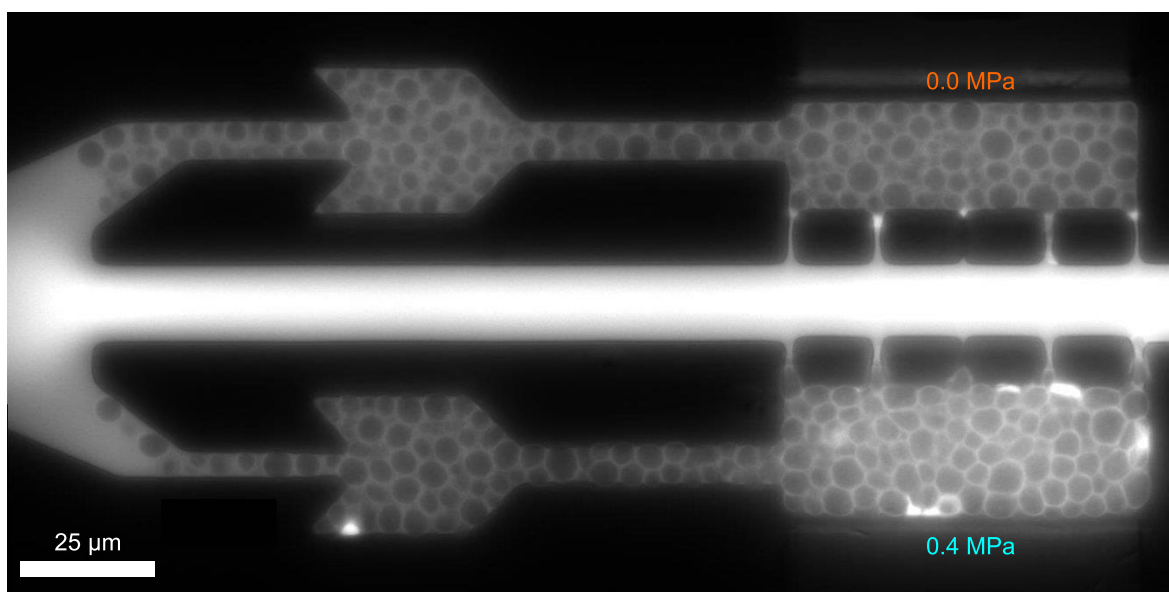

Figure 6.26: A fluorescent image is shown that depicts the difference in shape the *S. cerevisiae* cells possess at different growth-induced pressures. At low pressures the cells are mostly oval in shape, while a high pressure results in polygonal cell shapes.

Chapter 7

Discussion

7.1 *S. cerevisiae* in agar gels

In section 6.1.1 we qualitatively describe how *S. cerevisiae* cells grow in artificially created cracks inside agar gels and how the cells propagate these cracks. The initial crack patterns depend strongly on the tool we use for plunging the cells into the solid agar gels (syringe needles or pipette tips). We manually plunged the cells into the agar gels and consequentially, we could not exactly control how deep and at which angle the tools were inserted. This variability in crack initiation most likely biased the observed crack patterns. In order to obtain quantitative results from these kinds of crack propagation experiments, a more controlled method of crack initiation needs to be developed. For example a z-stage on which the plunging tool is fixed could be applied. Furthermore, it would be interesting to observe if cells of the undomesticated BR-F strain start to invade the agar gels after the cracks were propagated (for details about agar invasion compare section 2.4). In our crack propagation experiments conducted with BR-F yeasts we did not observe any agar invasion, which might be due to the fact that we only image two dimensional projections of the crack patterns. In these projections small cracks initiated by agar surface invasion of the cells could remain hidden.

By embedding whole colonies of *S. cerevisiae* cells, the bias of crack initiation could be circumvented since no cracks are present after the agar solidifies. Furthermore, we could extract the growth-induced pressure values from the volume of the colonies as a function of time up to the time point of crack formation. The volume measurement (cf section 4.1) can be further improved by acquisition of three dimensional images of the colonies since in our measurement technique we have to assume that the colony is spherical which might not be the case in the z-direction that is not imaged. We plot the pressure curves of the embedded colonies together with the beginning of slowest increasing pressure curve of a self-closing valve in figure 7.1. The variability between the pressure curves for the in agar gels embedded colonies could be due to different three dimensional shapes of the colonies. Interestingly, the pressure in the self-closing valve device increases faster than all of the curves related to embedded colonies. A possible explanation is that not all cells in the embedded colonies have access to nutrient. The cells at the periphery of the colony are directly in contact with the nutrients of the YPD agar gel, while the cells in the bulk of the colony do not have direct access to this nutrient source. In the self-closing valve on the other hand the nutrient supply to all cells in the growth chamber is ideal as is shown in section 6.2.1.

Due to the relatively low compressive strength of the agar gels (0.059 MPa [97]) and the corresponding failure of the material, we can only measure growth-induced pressures up to

approximately this value in our experiments. In order to measure higher growth-induced pressures different hydrogels with higher compressive strength might be employed (e.g. acrylamide gel or Tetra-PEG gel [109]). Since our main interest was to observe the formation of cracks by the forces the cells exert during growth, we did not try out other hydrogels. Furthermore, we additionally designed a microfluidic device that allows for measurements of growth-induced pressures, better controlled nutrient supply to the whole cell population and direct observation of single cells by fluorescence microscopy. Nevertheless, embedding cell colonies in hydrogels with appropriate material properties can provide a very easy method to measure growth-induced pressures without the need of creating microfluidic structures by photolithography (compare section 3.1.1) and PDMS molding (compare section 3.1.2). A similar technique was developed by Cheng *et al.* [4], in which cancer spheroids were embedded in agarose gels. They also observed crack formation mediated by growth-induced pressures in their experiments.
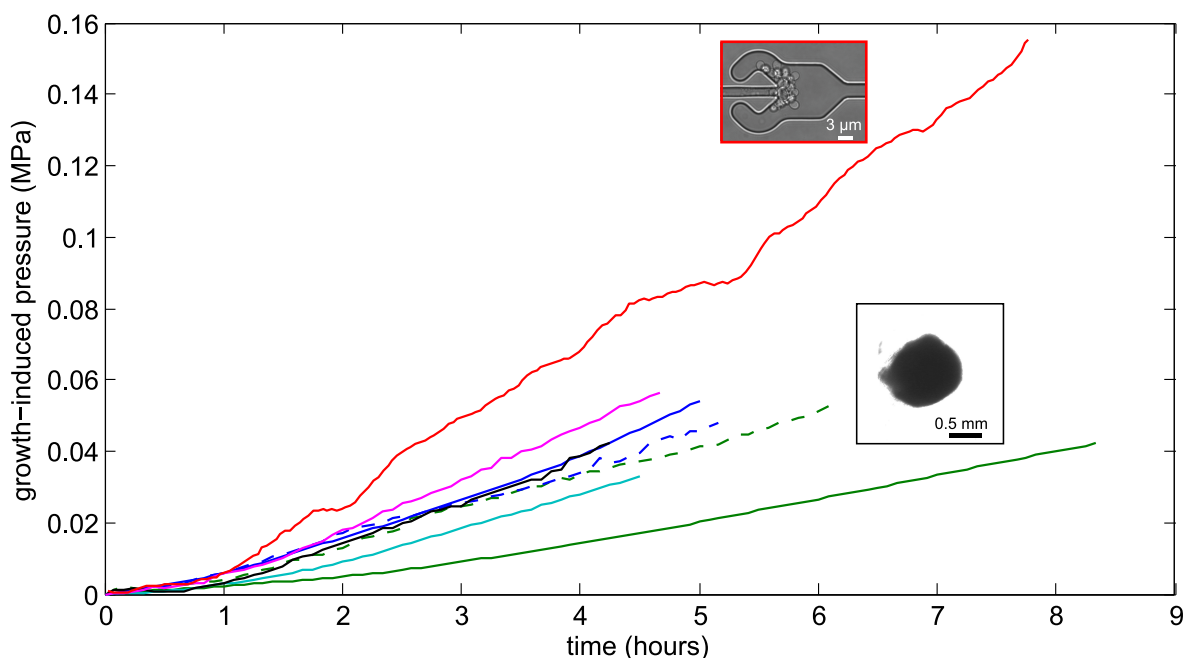

Figure 7.1: The growth-induced pressure curves of the in agar gels embedded yeast colonies are plotted together with the slowest increasing pressure curve of the self-closing valve device for comparison. The data are the same as in figure 6.4 and 6.14.

7.2 Dynamics of pressure curves

The pressure curve of the self-closing valve device in figure 6.14 clearly shows two regimes. A first regime where the pressure increases fast with a slope of about 0.2 MPa/h and a second regime, in which the increase slows down to about 0.009 MPa/h. These two regimes were also observed in other systems. Alessandri *et al.* encapsulated tumor spheroids in alginate shells [67]. The corresponding pressure curves also show two regimes even though the pressures were lower with values in the order of 1 kPa. The growth of confined bacterial populations of *E. coli* resulted in similar pressure dynamics as well, as was measured by Stewart and

Robertson [7]. It is remarkable that these three different cell types (bacteria, mammalian cancer cells and yeasts) all show similar pressure dynamics when grown in confinement.

For the cancer spheroid experiments most of the cells in the tumor sphere started to die with the start of the second regime and only a small fraction of cells close to the surface kept growing. This explains the slowdown in pressure increase in the corresponding experiment.

In our experiments we found that the growth rate decays exponentially with growth-induced pressure (compare figure 6.24 in section 6.2.4). The decrease in growth rate is strongly correlated to a cell cycle delay of cells in their G1 phase (see figure 6.25). Further test experiments conducted by Dr. Morgan Delarue revealed that only a small fraction (about 10 %) of the yeast cells dies in our experiments at a high growth-induced pressure of about 1.0 MPa, as is shown in figure 7.2. The cells rather completely cease to metabolize nutrients, as was measured by independently staining cells for metabolic activity and for viability, respectively. These results indicate that cells in our system are not dying as in the cancer spheroids of Alessandri *et al.* [67], but rather delay in the G1 phase of the cell cycle (details about the cell cycle can be found in section 2.1). The decrease in growth rate can also be a direct response to the increased mechanical forces acting on the cells, since slow growing *S. cerevisiae* cells show an increased resistance to a wide range of stresses (e.g. mechanical stress [57]), as we discussed already in section 2.5.
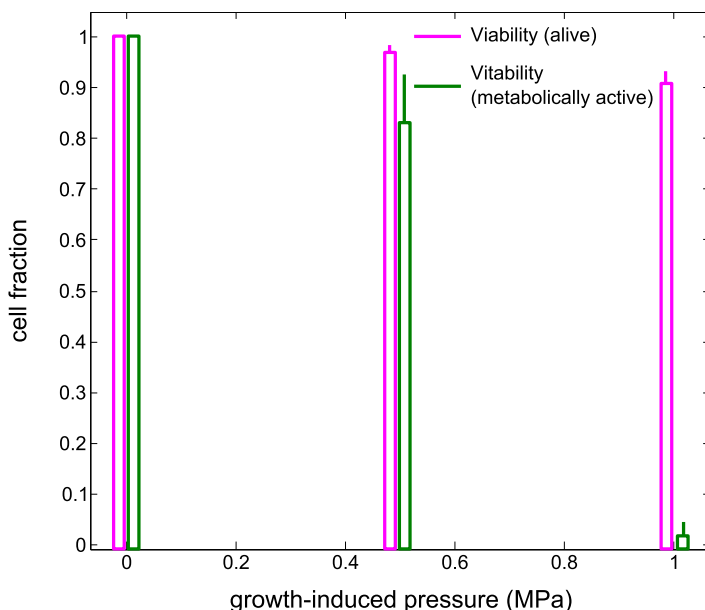

Figure 7.2: Fraction of cells that are viable (alive) and vitable (metabolically active) at different growth-induced pressure values. The experiments and analysis were conducted by Dr. Morgan Delarue.

7.3 Channel width and cell adhesion

The influence of the width of the exit channel on the growth-induced pressure is very strong as can be seen in figure 6.18 in section 6.2.2. The channel that has a width of 7.5 µm is too wide to promote any noticeable cell clot formation in the experiments conducted with the

lab yeast strain S288c, as is apparent from the growth-induced pressure curve that fluctuates only between 0 MPa and 0.03 MPa.

The strong cell-cell adhesion found in the undomesticated yeast strain BR-F (compare section 2.4) leads to a significant promotion of cell clot formation as can be seen in figure 7.3. The corresponding device is equipped with 45° leaky valves. The upper exit channel has a default width of 7.5 µm, while the lower channel is 5 µm wide. The growth-induced pressures in the upper and lower part of the device are very high with about 0.9 MPa. Cells are being pushed out of the nutrient slits at this pressure but stay attached to other cells of the population still inside the growth chamber. In order to compare this to the lab strain S288c we refer to figure 6.15 in section 6.2.2, in which the pressure curve of the corresponding 45° leaky valve device hardly surpasses pressure values of 0.1 MPa. This indicates that the ability to form cell clots and the strength of these clots strongly depend on the strength of cell-cell adhesion of the corresponding cells.

In nature one typically encounters undomesticated yeast strains that exhibit strong cell-cell adhesion. As a consequence, cell clots can easily form even when the constrictions are not very narrow and hence, large growth-induced pressures can be exerted by the cells (if the nutrient conditions are favorable enough). This indicates that high mechanical forces might be exerted by the growth and division of *S. cerevisiae* and bacterial cells showing strong cell-cell adhesion in the soil [9] or in rocks [10].
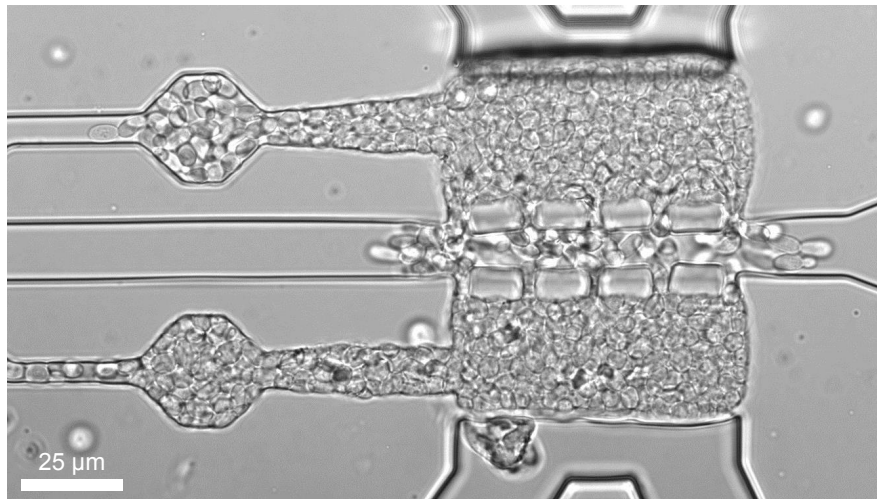

Figure 7.3: An image of a nutrient slit device, in which cells of the undomesticated strain BR-F are growing, is shown. The growth-induced pressures in both parts (upper and lower part) are measured as about 0.9 MPa.

7.4   Cell avalanche statistics

The survival functions presented in section 6.2.3 describe the statistical behavior of cell avalanches and overall cell flow characteristics (e.g. through the flowing parameter Φ).

If meaningful results shall be extracted from the survival functions large statistics are important. Especially, the tails of the survival functions, which describe the cell flow characteristics, require good statistics. The shape of the tails is largely determined by rare events

of large magnitude in pressure drops or survival times. The relative errors of the power-law exponents (cf table 6.1) are quite large with values between 25% and 57%. Hence, the statistical results and corresponding interpretations could greatly benefit from additional experiments. Especially, more experiments with 45° leaky valve devices are required since we did not present the corresponding data yet due to the small amount of experiments and hence cell avalanches. Nevertheless, the analysis method we adapted from Zuriguel *et al.* [58] provides a powerful tool to understand the characteristics of the cell avalanches we observe in our various devices.

When microbes grow in small cavities in the soil [9] or in rocks [10] they might be partially confined similar to our leaky valve devices. Accordingly, cell avalanches might readily occur in nature. The cells might experience alternating periods of rises and drops in growth-induced pressure. It would be interesting to understand how cells adapt to this intermittent pressure behavior for instance in terms of protein composition and cell wall architecture (compare sections 2.3 and 2.5). Our device is especially suited for this task since we can tune the magnitude of the growth-induced pressure and the characteristics of the cell avalanches by choosing the appropriate leaky valve. At the same time we can study the cells with fluorescence microscopy. Provided the access of appropriate yeast strains or staining methods suited for a specific question we want to address (e.g. abundance of a certain cell wall protein), we can easily study this problem with our device.

Chapter 8

Summary, conclusion and outlook

We developed a microfluidic device that provides the possibility to study *Saccharomyces cerevisiae* cells under mechanical confinement, while fully controlling the nutrient conditions. We explicitly aimed at measuring the mechanical pressure induced by the growth of whole cellular populations, which consist of several hundreds of cells. The measurement of this growth-induced pressure is achieved by the displacement of a PDMS membrane in contact with the cellular population. To the best of our knowledge our microfluidic device provides for the first time a reliably way to measure growth-induced pressures of cell populations.

We can influence the magnitude and dynamics of the growth-induced pressure by choosing from a set of passive cell flow control valves. One of these passive valves enables us to completely confine the cells and by this measure the maximal stalling pressure *S. cerevisiae* populations can exert. This valve makes use of the growth-induced pressure itself to close the cells in and hence is called self-closing valve. The other passive valves used in this study do not completely confine the cells, but rather facilitate the formation of cell clots. A cell clot can get dissolved when the growth-induced pressure rises to a certain value. As a result a whole avalanche of cells escapes the confinement of the device leading to a sudden drop in growth-induced pressure until another cell clot forms. The resulting growth-induced pressure curves show an intermittent behavior from which we can study statistics of the cell avalanches.

The ubiquitous flow of cells through the valves enables us to measure growth rates of the cell populations from cell flow velocities. We find that the growth rate decays exponentially with increasing growth-induced pressure. Furthermore, we studied a specific *S. cerevisiae* strain in our device, whose cells exhibit a fluorescent signal dependent on the cell cycle position. From these experiments we found that the decrease in growth rate is strongly correlated to the amount of cells delayed in the G1 phase of the cell cycle.

Finally, we studied *S. cerevisiae* cells in YPD agar gels. In these experiments we observed that the yeast cells are able to propagate and even form cracks inside of the agar gels. We developed a method to measure the growth-induced pressure from the growth of a colony totally embedded in agar gel. Even though the nutrient conditions are not as controlled as in our microfluidic device and we can not image single cells, this method provides an easy alternative to measure growth-induced pressures. The agar gel experiments can still be improved by changing the type of hydrogel since only growth-induced pressures approximately up to the compressive strength of the surrounding hydrogel can be measured (0.059 MPa in the case of 2 % agar gels*).

In standard culture methods microbes are typically grown in liquid suspension and hence

---

*mass percentage

do not experience any physical confinement. In our device we can mimic the mechanical conditions that are close to those found in some natural habitats where cells grow embedded in biofilms [8], confined in the soil [9] or inside rocks [10]. Additionally, our experiments can further elucidate the mechanical contribution of cellular population growth to biodeterioration. Biodeterioration was for example observed in marble through mechanical forces exerted by fungal cells during growth [14]. These mechanical forces lead to propagation of cracks in the marble [14]. Moreover, studying cell populations in our leaky valve devices can shed light on how cells can be confined in natural habitats. Our results indicate that cells entrap themselves through the formation of cell clots at narrow orifices. The interplay between the formation of cell clots and the escape of cells in the form of avalanches probably presents the prevalent growth condition cells under confinement experience in nature. Confined cells would consequentially be subjected to intermittent changes in growth-induced pressure whose influences can be studied easily with our devices. It can also be tested under which conditions cell clots, which are responsible for the confinement of the cell populations, form. These intermittent changes in growth-induced pressure mediated by the various leaky cell flow valves is reminiscent of driven granular materials [62, 110] and crowd swarming during escape panic [58]. In these systems the driving forces induce (temporal) clogging and subsequent increases in contact forces when the grains or individuals encounter bottlenecks. These formed clots can be destroyed when the contact forces reach a high enough value to overcome the frictional interaction between granular particles [60]. In our experiments the driving force of the soft granular material (yeast cells) is the growth-induced pressure, which results from the proliferation of the cellular population. Hence, we can study self-driven clot formation of growing cell populations with our device.

As mentioned in section 7.4 our cell avalanche results would greatly benefit from larger statistics. To meet this requirement Dr. Morgan Delarue has designed a new device with 64 single growth chambers. The device is depicted in figure 8.1a (only 32 of the 64 growth chambers are shown in this figure). Figure 8.1b shows a zoom onto two of the growth chambers, in which the position of the PDMS membrane, the nutrient channels and the valves are indicated. The measurement of the growth-induced pressure is achieved over the displacement of the PDMS membranes without any feedback, since in order to apply the feedback algorithm 64 independent syringe pumps and pressure sensors would be required and it is questionable if our technical capabilities are sufficient to operate this many pumps and sensors independently. Additionally, the device is loaded with cells from two different inlets. This way the growth chambers in the upper and lower halves can be filled with cells from two different cell strains. Hence, we can conduct one experiment, in which two cell strains are investigated at the same time each strain in 32 different growth chambers. Furthermore, the cells in the upper and lower growth chambers are supplied by different supply channels, so that two different nutrient media can be tested simultaneously.

In section 6.2.2 first results of our active valve device (equipped with Abate valves [94]) are presented. With this device we can actively control the growth-induced pressure of the cell population (see figure 6.13). We still observe that the growth-induced pressure also increases due to cell clots in this device. We could possibly circumvent this by implementing a larger exit channel that does not induce cell clot formation as easily. In section 6.2.2 we found that a exit channel width of 7.5 µm is already large enough to prevent cell clot formation in the lab strain experiments. The device needs to be tested further to determine how the growth-induced pressure reacts to the hydrostatic pressures applied in the Abate valves. These active valves enable us to probe the cells under a variety of adaptable mechanical conditions. For

instance, we can elucidate how fast the cells recover from high growth-induced pressures. In order to measure the speed of recovery, we can rapidly decrease the hydrostatic pressure in the Abate valves, which consequentially lowers the growth-induced pressure and we thus can observe the duration until the growth rate increases again (in section 6.2.4 we have shown that the growth rate decreases exponentially with increasing growth-induced pressure).

Furthermore, we can study other *S. cerevisiae* strains in our device at various growth-induced pressure conditions. For instance in the yeast strain Hsp12 the green fluorescent protein (GFP) is fused to the Hsp12 stress protein. This protein is hundredfold upregulated under different environmental stresses, e.g. cell wall stress [111]. Our device can be used to observe at which stress value this Hsp12 upregulation occurs and how long it takes until the protein is downregulated once the growth-induced pressure decreases[†]. Another *S. cerevisiae* strain worth studying is the Hog strain. Hog is the name of the high osmolarity glycerol pathway. The function of this pathway is to increase the intracellular glycerol concentration in order to increase the turgor pressure under hyperosmotic stress [25] (compare also section 2.2, in which the turgor pressure is explained). In the Hog strain GFP is fused to the Hog-protein responsible for increasing the intracellular glycerol concentration. In our device we can study if and when this pathway is activated under mechanical stress.

To study other cell types (for instance bacteria and mammalian cancer cells) our device would have to be adapted. In order to confine bacteria as for instance *E. coli* and *B. subtilis* in our device we have to downsize the exit channel and nutrient channels. Both bacterial species are rod-shaped with an average short axis diameter of about 0.8 µm and *E. coli* cells are even able to push through channels with a width that equals half of this diameter [16].

[†]We can use our Abate valve device to decrease the growth-induced pressure at controllable stages in the experiment.
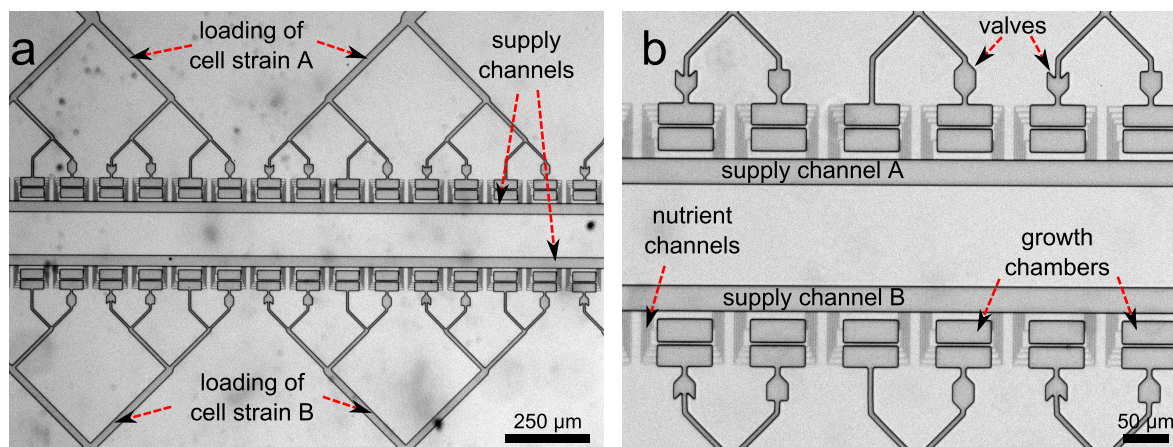

Figure 8.1: a) An alternative design of our device that enables us to simultaneously study 64 cell populations is shown (only 32 of the 64 growth chambers are depicted). Two different cell strains can be studied at the same time by loading the growth chambers in the upper and lower part independently. Also two different nutrient media can be used in the two supply channels so that cells in the upper and lower growth chamber can be subjected to different nutrient conditions. b) A zoom onto two of the growth chambers show the PDMS membrane, nutrient channels and the growth chamber in more detail.

Consequentially, we have to build structures with channels smaller than 0.4 µm in width to study *E. coli* populations under confinement. With our standard photolithography methods we are not able to create such small structures. Electron beam lithography could provide a solution for this problem, since in electron beam lithography structures with sizes down to 10 - 30 nm can be created [112]. In order to study mammalian cancer cells the device needs to be upsized. HeLa cells for instance have a diameter of 15 µm [113], and thus would not fit through our exit channels[‡]. Mammalian cancer cells exert much lower growth-induced pressures in the order of 1 kPa [4, 67] than the pressures in the order of 0.1 - 1 MPa exerted by *S. cerevisiae* cells in our experiments. The precision of the growth-induced pressure measurement in our device is 5 - 10 kPa. Consequentially, we have to improve this precision in order to study mammalian cancer cells in our device. One way to solve this could be to use the elastomer poly(glycerol sebacate) (PGS) instead of PDMS [114]. PGS has a Young's modulus of 0.056 MPa when synthesized at 110°C [115]. Due to the linear relation between displacement and pressure divided by Young's modulus (see equation 5.11 in section 5.4.3), we can estimate the precision of the growth-induced pressure measurement to be about 0.165 - 0.330 kPa if we substitute PGS for PDMS in our devices, which would be precise enough to measure growth-induced pressures in the order of 1 kPa for mammalian cancer cells.

[‡]The exit channels are 5 µm wide in the current designs.

Bibliography

[1] Pablo Fernández, Pramod A Pullarkat, and Albrecht Ott. A master relation defines the nonlinear viscoelasticity of single fibroblasts. *Biophysical journal*, 90(10):3796–3805, 2006.

[2] Matthias Chiquet, Manuel Koch, Mark Matthisson, Michael Tannheimer, and Ruth Chiquet-Ehrismann. Regulation of extracellular matrix synthesis by mechanical stress. *Biochemistry and Cell Biology*, 74(6):737–744, 1996.

[3] Matthias Chiquet. Regulation of extracellular matrix gene expression by mechanical stress. *Matrix Biology*, 18(5):417–426, 1999.

[4] Gang Cheng, Janet Tse, Rakesh K Jain, and Lance L Munn. Micro-environmental mechanical stress controls tumor spheroid size and morphology by suppressing proliferation and inducing apoptosis in cancer cells. *Plos One*, 4(2):1–11, 2009.

[5] Fabien Montel, Morgan Delarue, Jens Elgeti, Laurent Malaquin, Markus Basan, Thomas Risler, Bernard Cabane, Danijela Vignjevic, Jacques Prost, Giovanni Cappello, and Jean-François Joanny. Stress clamp experiments on multicellular tumor spheroids. *Phys. Rev. Lett.*, 107(18):188102, 2011.

[6] Triantafyllos Stylianopoulos, John D Martin, Vikash P Chauhan, Saloni R Jain, Benjamin Diop-Frimpong, Nabeel Bardeesy, Barbara L Smith, Cristina R Ferrone, Francis J Hornice, Yves Boucher, Lance L Munn, and Rakesh K Jain. Causes, consequences, and remedies for growth-induced solid stress in murine and human tumors. *Proc. Natl. Acad. Sci.*, 109(38):15101–15108, 2012.

[7] Philip S Stewart and Channing R Robertson. Microbial growth in a fixed volume: studies with entrapped escherichia coli. *Applied microbiology and biotechnology*, 30(1):34–40, 1989.

[8] Paula Watnick and Roberto Kolter. Biofilm, City of Microbes. *J. Bacteriol.*, 182(10):2675–2679, 2000.

[9] Paul D Sniegowski, Peter G Dombrowski, and Ethan Fingerman. Saccharomyces cerevisiae and saccharomyces paradoxus coexist in a natural woodland site in north america and display different levels of reproductive isolation from european conspecifics. *FEMS Yeast Research*, 1(4):299–306, 2002.

[10] HM Lappin-Scott and JW Costerton. Starvation and penetration of bacteria in soils and rocks. *Experientia*, 46(8):807–812, 1990.

[11] T Warsheid and J Braams. Biodeterioration of stone: a review. *Intl. Biodet. and Biodegrad.*, 46(4):343–368, 2000.

[12] E Diakumaku, AA Gorbushina, WE Krumbein, L Panina, and S Soukharjevski. Black fungi in marble and limestonesan aesthetical, chemical and physical problem for the conservation of monuments. *Science of the Total Environment*, 167(1):295–304, 1995.

[13] Katja Sterflinger and Wolfgang E Krumbein. Dematiaceous fungi as a major agent for biopitting on mediterranean marbles and limestones. *Geomicrobiology Journal*, 14(3):219–230, 1997.

[14] Th Dornieden, AA Gorbushina, and WE Krumbein. Biodecay of cultural heritage as a space/time-related ecological situationan evaluation of a series of studies. *International biodeterioration & biodegradation*, 46(4):261–270, 2000.

[15] Masaya Suzuki, Yosuke Asada, Daisuke Watanabe, and Yoshikazu Ohya. Cell shape and growth of budding yeast cells in restrictive microenvironments. *Yeast*, 21(12):983–989, 2004.

[16] Jaan Männik, Rosalie Driessen, Peter Galajda, Juan E Keymer, and Cees Dekker. Bacterial growth and motility in sub-micron constrictions. *Proceedings of the National Academy of Sciences*, 106(35):14861–14866, 2009.

[17] Matthew T Cabeen, Godefroid Charbon, Waldemar Vollmer, Petra Born, Nora Ausmees, Douglas B Weibel, and Christine Jacobs-Wagner. Bacterial cell curvature through mechanical control of cell growth. *The EMBO journal*, 28(9):1208–1219, 2009.

[18] John R Pringle and Leland H Hartwell. The saccharomyces cerevisiae cell cycle. *Cold Spring Harbor Monograph Archive*, 11:97–142, 1981.

[19] Ira Herskowitz. Life cycle of the budding yeast saccharomyces cerevisiae. *Microbiological reviews*, 52(4):536, 1988.

[20] Ahmed Touhami, Bernard Nysten, and Yves F Dufrêne. Nanoscale mapping of the elasticity of microbial cells by atomic force microscopy. *Langmuir*, 19(11):4539–4543, 2003.

[21] Paul K Herman. Stationary phase in yeast. *Current opinion in microbiology*, 5(6):602–607, 2002.

[22] M Werner-Washburne, E Braun, GC Johnston, and RA Singer. Stationary phase in the yeast saccharomyces cerevisiae. *Microbiological reviews*, 57(2):383–401, 1993.

[23] IM De Mara on, Pierre-André Marechal, and Patrick Gervais. Passive response of saccharomyces cerevisiae to osmotic shifts: cell volume variations depending on the physiological state. *Biochemical and biophysical research communications*, 227:519–523, 1996.

[24] Martin Latterich and Martin D Watson. Evidence for a dual osmoregulatory mechanism in the yeast saccharomyces cerevisiae. *Biochemical and biophysical research communications*, 191(3):1111–1117, 1993.

[25] Hassan Dihazi, Renate Kessler, and Klaus Eschrich. High osmolarity glycerol (hog) pathway-induced phosphorylation and activation of 6-phosphofructo-2-kinase are essential for glycerol accumulation and yeast cell proliferation under hyperosmotic stress. *Journal of Biological Chemistry*, 279(23):23961–23968, 2004.

[26] DJ Klionsky, PK Herman, and SD Emr. The fungal vacuole: composition, function, and biogenesis. *Microbiological reviews*, 54(3):266, 1990.

[27] Michael C Gustin, Xin-Liang Zhou, Boris Martinac, and Ching Kung. A mechanosensitive ion channel in the yeast plasma membrane. *Science*, 242(4879):762–765, 1988.

[28] James A Lockhart. An analysis of irreversible plant cell elongation. *Journal of theoretical biology*, 8(2):264–275, 1965.

[29] Arezki Boudaoud. Growth of walled cells: from shells to vesicles. *Physical review letters*, 91(1):018104, 2003.

[30] Nicolas Minc, Arezki Boudaoud, and Fred Chang. Mechanical Forces of Fission Yeast Growth. *Curr. Biol.*, 19:1096–1101, 2009.

[31] Alexander E Smith, Zhibing Zhang, Colin R Thomas, Kennith E Moxham, and Anton PJ Middelberg. The mechanical properties of saccharomyces cerevisiae. *Proceedings of the National Academy of Sciences*, 97(18):9871–9874, 2000.

[32] Frans M Klis, Pieternella Mol, Klaas Hellingwerf, and Stanley Brul. Dynamics of cell wall structure in saccharomyces cerevisiae. *FEMS microbiology reviews*, 26(3):239–256, 2002.

[33] Masako Osumi. The ultrastructure of yeast: cell wall structure and formation. *Micron*, 29(2):207–233, 1998.

[34] JG De Nobel, C Dijkers, E Hooijberg, and FM Klis. Increased cell wall porosity in saccharomyces cerevisiae after treatment with dithiothreitol or edta. *Journal of general microbiology*, 135(7):2077–2084, 1989.

[35] Andrew E Pelling, Sadaf Sehati, Edith B Gralla, Joan S Valentine, and James K Gimzewski. Local nanomechanical motion of the cell wall of saccharomyces cerevisiae. *Science*, 305(5687):1147–1150, 2004.

[36] Tiziana Svaldo Lanero, Ornella Cavalleri, Silke Krol, Ranieri Rolandi, and Alessandra Gliozzi. Mechanical properties of single living cells encapsulated in polyelectrolyte matrixes. *Journal of biotechnology*, 124(4):723–731, 2006.

[37] VC Bui, YU Kim, and SS Choi. Physical characteristics of saccharomyces cerevisiae. *Surface and Interface Analysis*, 40(10):1323–1327, 2008.

[38] Etienne Dague, Rajaa Bitar, Hubert Ranchon, Fabien Durand, Hélène Martin Yken, and Jean M François. An atomic force microscopy analysis of yeast mutants defective in cell wall architecture. *Yeast*, 27(8):673–684, 2010.

[39] Alexander Evans Smith, Z Zhang, and CR Thomas. Wall material properties of yeast cells: Part 1. cell measurements and compression experiments. *Chemical Engineering Science*, 55(11):2031–2041, 2000.

[40] JD Stenson, CR Thomas, and P Hartley. Modelling the mechanical properties of yeast cells. *Chemical Engineering Science*, 64(8):1892–1903, 2009.

[41] John D Stenson, Peter Hartley, Changxiang Wang, and Colin R Thomas. Determining the mechanical properties of yeast cell walls. *Biotechnology progress*, 27(2):505–512, 2011.

[42] RD Chaudhari, JD Stenson, TW Overton, and CR Thomas. Effect of bud scars on the mechanical properties of saccharomyces cerevisiae cell walls. *Chemical Engineering Science*, 84:188–196, 2012.

[43] Ruben Mercadé-Prieto, Colin R Thomas, and Zhibing Zhang. Mechanical double layer model for saccharomyces cerevisiae cell wall. *European Biophysics Journal*, 42(8):613–620, 2013.

[44] Anne M Dranginis, Jason M Rauceo, Juan E Coronado, and Peter N Lipke. A biochemical guide to yeast adhesins: glycoproteins for social and antisocial occasions. *Microbiology and Molecular Biology Reviews*, 71(2):282–294, 2007.

[45] Libuše Váchová, Vratislav Št'ovíček, Otakar Hlaváček, Oleksandr Chernyavskiy, Luděk Štěpánek, Lucie Kubínová, and Zdena Palková. Flo11p, drug efflux pumps, and the extracellular matrix cooperate to form biofilm yeast colonies. *The Journal of cell biology*, 194(5):679–687, 2011.

[46] Lars Fichtner, Florian Schulze, and Gerhard H Braus. Differential flo8p-dependent regulation of flo1 and flo11 for cell–cell and cell–substrate adherence of s. cerevisiae s288c. *Molecular microbiology*, 66(5):1276–1289, 2007.

[47] Carlos J Gimeno, Per O Ljungdahl, Cora A Styles, and Gerald R Fink. Unipolar cell divisions in the yeast s. cerevisiae lead to filamentous growth: regulation by starvation and ras. *Cell*, 68(6):1077–1090, 1992.

[48] Jure Zupan and Peter Raspor. Quantitative agar-invasion assay. *Journal of microbiological methods*, 73(2):100–104, 2008.

[49] Wan-Sheng Lo and Anne M Dranginis. The cell surface flocculin flo11 is required for pseudohyphae formation and invasion by saccharomyces cerevisiae. *Molecular biology of the cell*, 9(1):161–171, 1998.

[50] Sofiane El-Kirat-Chatel, Audrey Beaussart, Stéphane P Vincent, Marta Abellán Flos, Pascal Hols, Peter N Lipke, and Yves F Dufrêne. Forces in yeast flocculation. *Nanoscale*, 7(5):1760–1767, 2015.

[51] Marco Siderius and Willem H Mager. Conditional response to stress in yeast. *Monatshefte für Chemie/Chemical Monthly*, 134(11):1433–1444, 2003.

[52] Audrey P Gasch. The environmental stress response: a common yeast response to diverse environmental stresses. In *Yeast stress responses*, pages 11–70. Springer, 2003.

[53] Johan M Thevelein and Johannes H De Winde. Novel sensing mechanisms and targets for the camp–protein kinase a pathway in the yeast saccharomyces cerevisiae. *Molecular microbiology*, 33(5):904–918, 1999.

[54] Emmanuelle Boy-Marcotte, Djamila Tadi, Michel Perrot, Helian Boucherie, and Michel Jacquet. High camp levels antagonize the reprogramming of gene expression that occurs at the diauxic shift in saccharomyces cerevisiae. *Microbiology*, 142(3):459–467, 1996.

[55] Marco Siderius, Eveline Rots, and Willem H Mager. High-osmolarity signalling in saccharomyces cerevisiae is modulated in a carbon-source-dependent fashion. *Microbiology*, 143(10):3241–3250, 1997.

[56] Beth Elliott and Bruce Futcher. Stress resistance of yeast cells is largely independent of cell cycle phase. *Yeast*, 9(1):33–42, 1993.

[57] Achim Overbeck, Ingo Kampen, and Arno Kwade. Mechanical characterization of yeast cells: Effects of growth conditions. *Letters in applied microbiology*, 2015.

[58] Iker Zuriguel, Daniel Ricardo Parisi, Raúl Cruz Hidalgo, Celia Lozano, Alvaro Janda, Paula Alejandra Gago, Juan Pablo Peralta, Luis Miguel Ferrer, Luis Ariel Pugnaloni, Eric Clément, et al. Clogging transition of many-particle systems flowing through bottlenecks. *Scientific reports*, 4, 2014.

[59] GDR MiDi. On dense granular flows. *The European Physical Journal E*, 14(4):341–365, 2004.

[60] Yi Zhang and Charles S Campbell. The interface between fluid-like and solid-like behaviour in two-dimensional granular flows. *Journal of Fluid Mechanics*, 237:541–568, 1992.

[61] Dirk Helbing, Illés Farkas, and Tamas Vicsek. Simulating dynamical features of escape panic. *Nature*, 407(6803):487–490, 2000.

[62] Dapeng Bi, Jie Zhang, Bulbul Chakraborty, and RP Behringer. Jamming by shear. *Nature*, 480(7377):355–358, 2011.

[63] Hannah H Tuson, George K Auer, Lars D Renner, Mariko Hasebe, Carolina Tropini, Max Salick, Wendy C Crone, Ajay Gopinathan, Kerwyn Casey Huang, and Douglas B Weibel. Measuring the stiffness of bacterial cells from growth rates in hydrogels of tunable elasticity. *Molecular microbiology*, 84(5):874–891, 2012.

[64] Clément Vulin, Jean-Marc Di Meglio, Ariel B Lindner, Adrian Daerr, Andrew Murray, and Pascal Hersen. Growing yeast into cylindrical colonies. *Biophysical journal*, 106(10):2214–2221, 2014.

[65] Dmitri Volfson, Scott Cookson, Jeff Hasty, and Lev S Tsimring. Biomechanical ordering of dense cell populations. *Proceedings of the National Academy of Sciences*, 105(40):15346–15351, 2008.

[66] H Cho, Henrik Jönsson, Kyle Campbell, Pontus Melke, Joshua W Williams, Bruno Jedynak, Ann M Stevens, Alex Groisman, and Andre Levchenko. Self-organization in high-density bacterial colonies: efficient crowd control. *PLoS Biol*, 5(11):e302, 2007.

[67] Kévin Alessandri, Bibhu Ranjan Sarangi, Vasily Valrvitch Gurchenkov, Bidisha Sinha, Tobias Reinhold Kieling, Luc Fetler, Felix Rico, Simon Scheuring, Christophe Lamaze, Anthony Simon, Sara Geraldo, Danijela Vignjevi, Hugo Domjean, Leslie Rolland, Anette Funfak, Jrme Bibette, Nicolas Bremond, , and Pierre Nassoy. Cellular capsules as a tool for multicellular spheroid production and for investigating the mechanics of tumor progression in vitro. *Proc. Natl. Acad. Sci.*, 110(37):14843–14848, 2013.

[68] Seok Woo Lee and Seung S Lee. Shrinkage ratio of pdms and its alignment method for the wafer level process. *Microsystem Technologies*, 14(2):205–208, 2008.

[69] D Fuard, T Tzvetkova-Chevolleau, S Decossas, P Tracqui, and P Schiavone. Optimization of poly-di-methyl-siloxane (pdms) substrates for studying cellular adhesion and motility. *Microelectron. Eng.*, 85:1289–1293, 2008.

[70] ID Johnston, DK McCluskey, CKL Tan, and MC Tracey. Mechanical characterization of bulk sylgard 184 for microfluidics and microengineering. *Journal of Micromechanics and Microengineering*, 24(3):035017, 2014.

[71] D. Brambley, B. Martin, and P. D. Prewett. Microlithography: An Overview. *Adv. Mat. Opt. Electron.*, 4(2):55–74, 1994.

[72] Shantanu Bhattacharya, Arindom Datta, Jordan M Berg, and Shubhra Gangopadhyay. Studies on surface wettability of poly (dimethyl) siloxane (pdms) and glass under oxygen-plasma treatment and correlation with bond strength. *Microelectromechanical Systems, Journal of*, 14(3):590–597, 2005.

[73] Mark A. Eddings, Michael A. Johnson, and Bruce K. Gale. Determining the optimal pdmspdms bonding technique for microuidic devices. *J. Micromech. Microeng.*, 18:1–4, 2008.

[74] E Kondoh, T Asano, A Nakashima, and M Komatu. Effect of oxygen plasma exposure of porous spin-on-glass films. *Journal of Vacuum Science & Technology B*, 18(3):1276–1280, 2000.

[75] Marc A. Unger, Hou-Pu Chou, Todd Thorsen, Axel Scherer, and Stephen R. Quake. Monolithic microfabricated valves and pumps by multilayer soft lithography. *Sci.*, 288(5463):113–116, 2000.

[76] Maria Pia Longhese, Holger Neecke, Vera Paciotti, Giovanna Lucchini, and Paolo Plevani. The 70 kda subunit of replication protein a is required for the g1/s and intra-s dna damage checkpoints in budding yeast. *Nucleic acids research*, 24(18):3533–3537, 1996.

[77] Ian R Adams and John V Kilmartin. Localization of core spindle pole body (spb) components during spb duplication in saccharomyces cerevisiae. *The Journal of cell biology*, 145(4):809–823, 1999.

[78] Oskar Hallatschek, Pascal Hersen, Sharad Ramanathan, and David R Nelson. Genetic drift at expanding frontiers promotes gene segregation. *Proceedings of the National Academy of Sciences*, 104(50):19926–19930, 2007.

[79] Haoping Liu, Cora Ann Styles, and Gerald R Fink. Saccharomyces cerevisiae s288c has a mutation in fl08, a gene required for filamentous growth. *Genetics*, 144(3):967–978, 1996.

[80] Francisco J Taberner, Inma Quilis, and J Carlos Igual. Spatial regulation of the start repressor whi5. *Cell Cycle*, 8(18):3013–3022, 2009.

[81] MSS Murthy, BS Rao, NMS Reddy, P Subrahmanyam, and U Madhvanath. Non-equivalence of yepd and synthetic complete media in yeast reversion studies. *Mutation Research/Fundamental and Molecular Mechanisms of Mutagenesis*, 27(2):219–223, 1975.

[82] Achim Wach, Arndt Brachat, Rainer Pöhlmann, and Peter Philippsen. New heterologous modules for classical or pcr-based gene disruptions in saccharomyces cerevisiae. *Yeast*, 10(13):1793–1808, 1994.

[83] Karin Elbing, Christer Larsson, Roslyn M Bill, Eva Albers, Jacky L Snoep, Eckhard Boles, Stefan Hohmann, and Lena Gustafsson. Role of hexose transport in control of glycolytic flux in saccharomyces cerevisiae. *Applied and environmental microbiology*, 70(9):5323–5330, 2004.

[84] Chenhui Zou, Yajie Wang, and Zhufang Shen. 2-nbdg as a fluorescent indicator for direct glucose uptake measurement. *Journal of biochemical and biophysical methods*, 64(3):207–215, 2005.

[85] Caroline A Schneider, Wayne S Rasband, and Kevin W Eliceiri. Nih image to imagej: 25 years of image analysis. *Nature methods*, 9(7):671–675, 2012.

[86] VT Nayar, JD Weiland, CS Nelson, and AM Hodge. Elastic and viscoelastic characterization of agar. *Journal of the mechanical behavior of biomedical materials*, 7:60–68, 2012.

[87] L. D. Landau and E. M. Lifshitz. *Theory of Elasticity*, page 13. Elsevier New York, 1986.

[88] Karl M Prewo and JJ Brennan. Silicon carbide yarn reinforced glass matrix composites. *Journal of Materials Science*, 17(4):1201–1206, 1982.

[89] H Prentice-Mott, D Irimia, A Russom, and M Toner. Modeling a microscale proportional flow controller. In *Proceedings of the COMSOL Conference*, 2007.

[90] Caesar Saloma, Gay Jane Perez, Giovanni Tapang, May Lim, and Cynthia Palmes-Saloma. Self-organized queuing and scale-free behavior in real escape panic. *Proceedings of the National Academy of Sciences*, 100(21):11947–11952, 2003.

[91] A Janda, Diego Maza, A Garcimartín, E Kolb, J Lanuza, and E Clément. Unjamming a granular hopper by vibration. *EPL (Europhysics Letters)*, 87(2):24002, 2009.

[92] Amy C. Rowat, James C. Bird, Jeremy J. Agresti, Oliver J. Rando, and David A. Weitz. Tracking lineages of single cells in lines using a microfluidic device. *Proc. Natl. Acad. Sci.*, 106(43):18149–18154, 2009.

[93] Rob Phillips, Jane Kondev, and Julie Theriot. *Physical Biology of the Cell*, chapter 1, page 26. Garland Science, 3 edition, 2009.

[94] A. R. Abate and D. A. Weitz. Single-layer membrane valves for elastomeric microfluidic devices. *Appl. Phys. Lett.*, 92:243509–1–243509–3, 2008.

[95] William T Cochran, James W Cooley, David L Favin, Howard D Helms, Reginald A Kaenel, William W Lang, George C Maling Jr, David E Nelson, Charles M Rader, and Peter D Welch. What is the fast fourier transform? *Proceedings of the IEEE*, 55(10):1664–1674, 1967.

[96] John Canny. A computational approach to edge detection. *Pattern Analysis and Machine Intelligence, IEEE Transactions on*, (6):679–698, 1986.

[97] A Nussinovitch and M Peleg. Strength-time relationships of agar and alginate gels. *Journal of Texture Studies*, 21(1):51–60, 1990.

[98] Joost van den Brink, Michiel Akeroyd, Rob van der Hoeven, JT Pronk, JH De Winde, and Pascale Daran-Lapujade. Energetic limits to metabolic flexibility: responses of saccharomyces cerevisiae to glucose–galactose transitions. *Microbiology*, 155(4):1340–1350, 2009.

[99] David R Lide. *CRC handbook of chemistry and physics*. CRC press, 2004.

[100] N Ertugay and H Hamamci. Continuous cultivation of bakers' yeast: change in cell composition at different dilution rates and effect of heat stress on trehalose level. *Folia microbiologica*, 42(5):463–467, 1997.

[101] Andrea K Bryan, Alexi Goranov, Angelika Amon, and Scott R Manalis. Measurement of mass, density, and volume during the cell cycle of yeast. *Proceedings of the National Academy of Sciences*, 107(3):999–1004, 2010.

[102] Amanda J Meikle, Robert H Reed, and Geoffrey M Gadd. Osmotic adjustment and the accumulation of organic solutes in whole cells and protoplasts of saccharomyces cerevisiae. *Journal of general microbiology*, 134(11):3049–3060, 1988.

[103] Stefano Di Talia, Jan M Skotheim, James M Bean, Eric D Siggia, and Frederick R Cross. The effects of molecular noise and size control on variability in the budding yeast cell cycle. *Nature*, 448(7156):947–951, 2007.

[104] Elizabeth A Wilder, Shu Guo, Sheng Lin-Gibson, Michael J Fasolka, and Christopher M Stafford. Measuring the modulus of soft polymer networks via a buckling-based metrology. *Macromolecules*, 39(12):4138–4143, 2006.

[105] Aaron Clauset, Cosma Rohilla Shalizi, and Mark EJ Newman. Power-law distributions in empirical data. *SIAM review*, 51(4):661–703, 2009.

[106] Stephen J Elledge. Cell cycle checkpoints: preventing an identity crisis. *Science*, 274(5293):1664–1672, 1996.

[107] David A Foster, Paige Yellen, Limei Xu, and Mahesh Saqcena. Regulation of g1 cell cycle progression distinguishing the restriction point from a nutrient-sensing cell growth checkpoint (s). *Genes & cancer*, 1(11):1124–1131, 2010.

[108] Wolfram Siede, Andrew S Friedberg, and Errol C Friedberg. Rad9-dependent g1 arrest defines a second checkpoint for damaged dna in the cell cycle of saccharomyces cerevisiae. *Proceedings of the National Academy of Sciences*, 90(17):7985–7989, 1993.

[109] Takamasa Sakai, Takuro Matsunaga, Yuji Yamamoto, Chika Ito, Ryo Yoshida, Shigeki Suzuki, Nobuo Sasaki, Mitsuhiro Shibayama, and Ung-il Chung. Design and fabrication of a high-strength hydrogel with ideally homogeneous network structure from tetrahedron-like macromonomers. *Macromolecules*, 41(14):5379–5384, 2008.

[110] Claus Heussinger and Jean-Louis Barrat. Jamming transition as probed by quasistatic shear flow. *Phys. Rev. Lett.*, 102:218303, May 2009.

[111] Sylvia Welker, Birgit Rudolph, Elke Frenzel, Franz Hagn, Gerhard Liebisch, Gerd Schmitz, Johannes Scheuring, Andreas Kerth, Alfred Blume, Sevil Weinkauf, et al. Hsp12 is an intrinsically unstructured stress protein that folds upon membrane association and modulates membrane function. *Molecular cell*, 39(4):507–520, 2010.

[112] C Vieu, F Carcenac, A Pepin, Y Chen, M Mejias, A Lebib, L Manin-Ferlazzo, L Couraud, and H Launois. Electron beam lithography: resolution limits and applications. *Applied Surface Science*, 164(1):111–117, 2000.

[113] Anna Maria Luciani, Antonella Rosi, Paola Matarrese, Giuseppe Arancia, Laura Guidoni, and Vincenza Viti. Changes in cell volume and internal sodium concentration in hela cells during exponential growth and following lonidamine treatment. *European journal of cell biology*, 80(2):187–195, 2001.

[114] Christopher J Bettinger, Eli J Weinberg, Katherine M Kulig, Joseph P Vacanti, Yadong Wang, Jeffrey T Borenstein, and Robert Langer. Three-dimensional microfluidic tissue-engineering scaffolds using a flexible biodegradable polymer. *Advanced materials (Deerfield Beach, Fla.)*, 18(2):165, 2005.

[115] Qi-Zhi Chen, Alexander Bismarck, Ulrich Hansen, Sarah Junaid, Michael Q Tran, Siân E Harding, Nadire N Ali, and Aldo R Boccaccini. Characterisation of a soft elastomer poly (glycerol sebacate) designed to match the mechanical properties of myocardial tissue. *Biomaterials*, 29(1):47–57, 2008.

Appendix A

Appendix

A.1   Further results of Comsol simulations

Here, we show further results of our Comsol simulations.

Figures A.1a and A.1b depict the results of the colony volume simulations as functions of pressure with the corresponding linear fits for the different initial colony volumes. We measure the volumes of the colonies from the microscopic images as functions of time as described in section 4.1 and obtain the growth-induced pressure from the colony volume with help of the determined linear relations between volume and pressure.

We compare two Comsol simulations of a colony embedded in agar gel for different Poisson ratios of 0.49 and 0.499. We obtain linear relationships between the volume of the colony and the acting pressure. The results are shown in figure A.2. The difference between the slopes of the two linear fit functions is less than 0.3%. We can conclude that the two simulations do not differ in any way that would noticeably influence our results. We decided to set the Poisson ratio of the agar gel in the Comsol simulations to 0.49, since when approaching a Poisson ratio of 0.5 the simulations might become prone to errors due to the singularity in
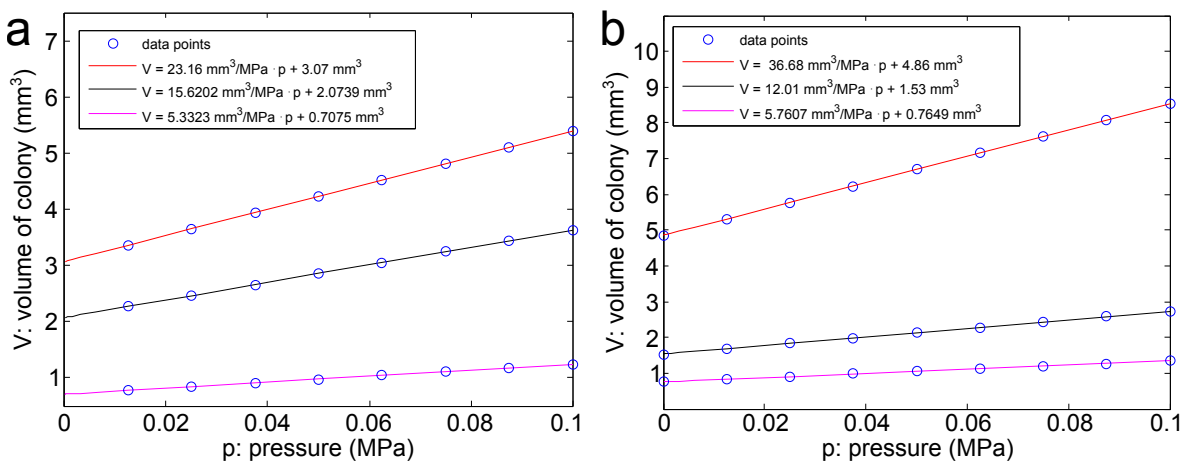
Figure A.1: Volume as function of pressure curves are shown together with the calculated linear fits. The additive terms depicted in the legends are the initial volumes of the respective colonies.

the stress strain constitutive relation (cf section 4.4.1).

For the cell flow measurements, we have to consider how the cross section of the channel between growth chamber and valve deforms with pressure. These cell flow measurements are needed to determine the degree of confinement of the various valves (compare section 6.2.1) and for the determination of the growth rate as a function of pressure (see section 6.2.4). The cross section is plotted in figure A.3a as a function of pressure together with the fit we obtain from our data. Additionally, we plotted the cross section as a function of maximal channel width in figure A.3b for default channel widths of 3 µm and 5 µm, respectively.
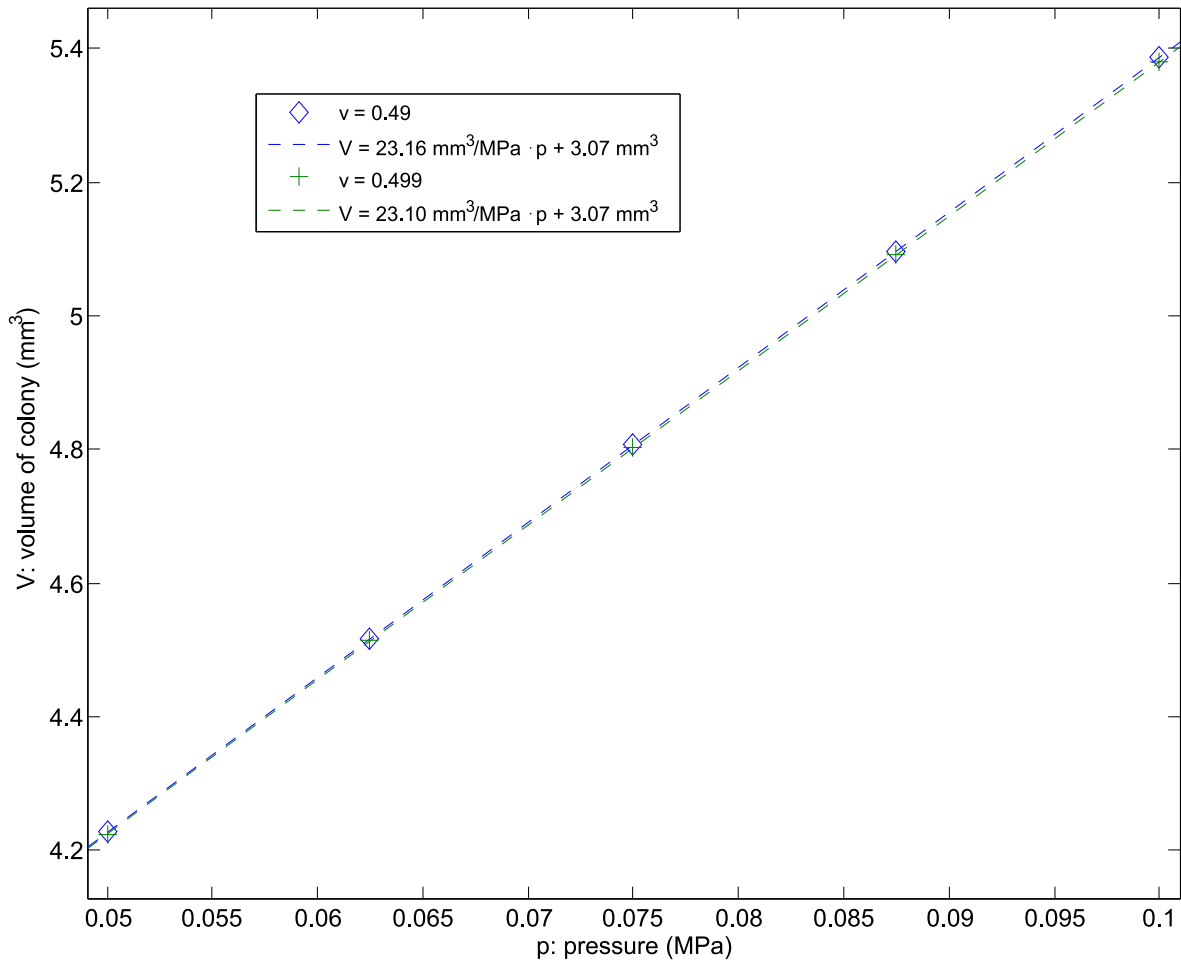
Figure A.2: We compare two Comsol simulations of a colony embedded in agar in this plot. We tested two different Poisson ratios for the agar gel in order to see if our choice had any strong influence.

a

b
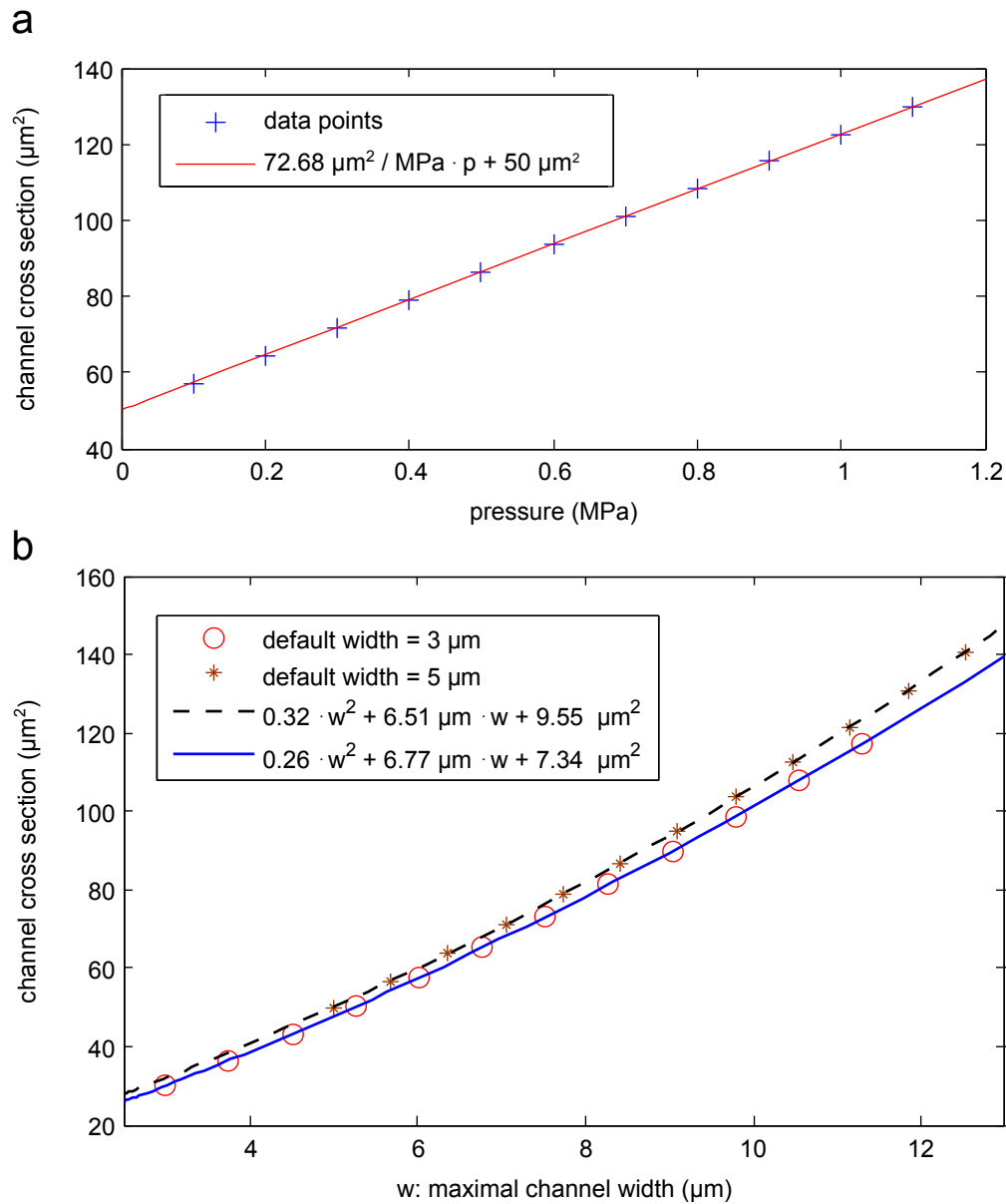
Figure A.3: a) The channel cross section is plotted as a function of pressure for a Young's modulus of 1.7 MPa. b) The channel cross section is plotted as a function of maximal channel width for default channel widths of 3 µm and 5 µm.

A.2   Dimensions of microfluidic structures

Figure A.4 shows detailed images of the structures used in the microfluidic experiments. Here, we show all physical dimensions in the corresponding images. Figure A.4a shows the growth chamber with the adjacent membrane used for the growth-induced pressure measurements. The self-closing valve, which nearly completely confines cell populations, is depicted in figure A.4b. The three leaky valves (45°, 90° and 135°) are shown in figures A.4c, A.4d and A.4e. Finally, the newest design of the Abate valves is depicted in figure A.4f.
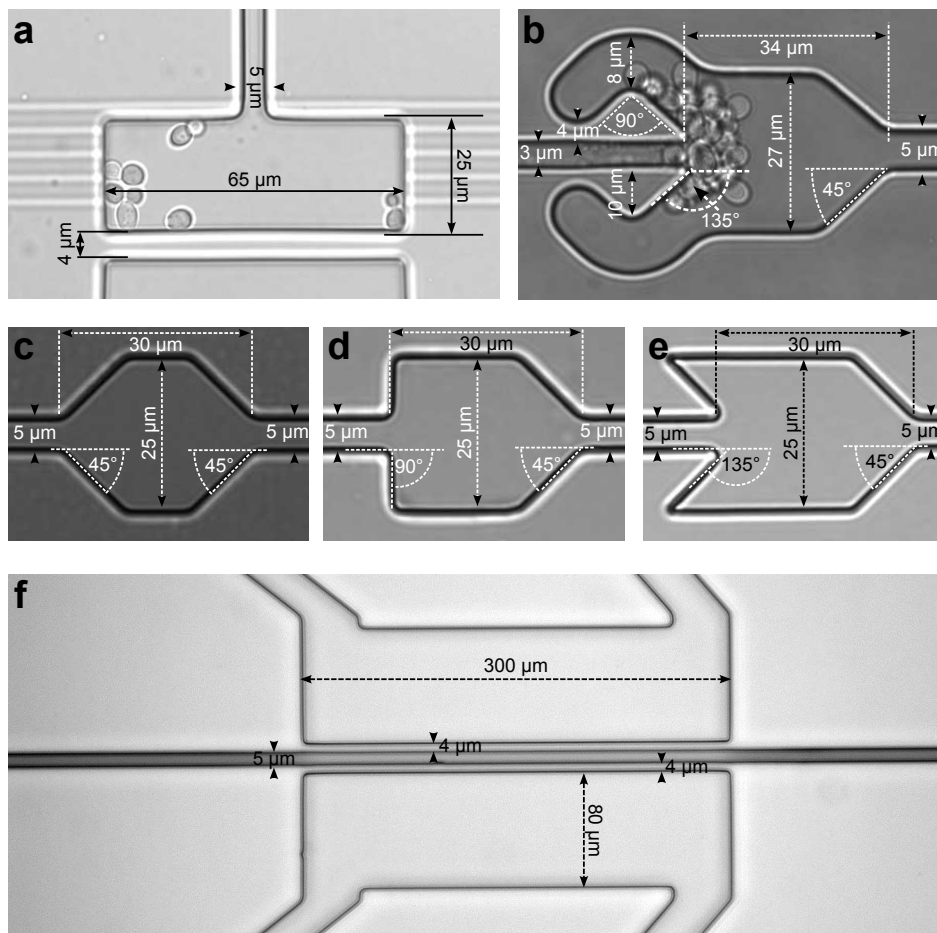
Figure A.4: Transmitted light micrographs of the PDMS molds of some of the microfluidic structures that were used in the experiments of this doctoral thesis are shown. The images show a) the growth chamber with PDMS membrane and nutrient channels, b) the self-closing valve, c) the 45° leaky valve, d) the 90° leaky valve, e) the 135° leaky valve and f) the Abate valves.

A.3   Additional images of cracks in agar gels

We show several images of agar cracks in this section. The cracks in figure A.5 were initiated with pipette tips. After propagation the typical star shaped patterns are visible. In figure A.6 cracks are shown that were initiated with syringe needles. These cracks always extent in opposite directions from the insertion site. Since the cracks always show these characteristic patterns with respect to the crack initiation tool (pipette tip or syringe needle), the chosen tool is most likely responsible for the pattern, as we argue in section 6.1.1.
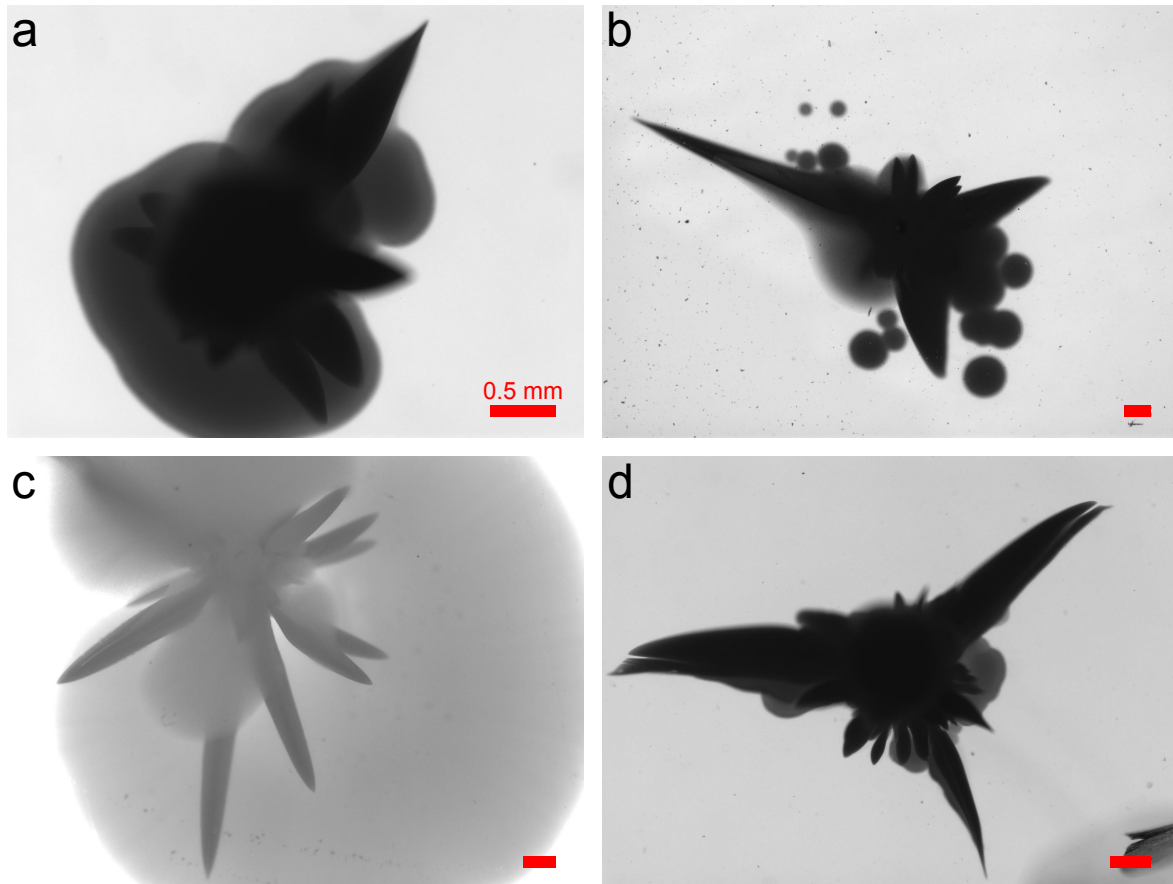
Figure A.5: Images of cracks in agar gels. The cracks were initiated with pipette tips and show characteristic star shaped patterns. The cracks were grown for different amounts of time: a) 1 day, b) 3 days, c) 5 days and d) 1 day.
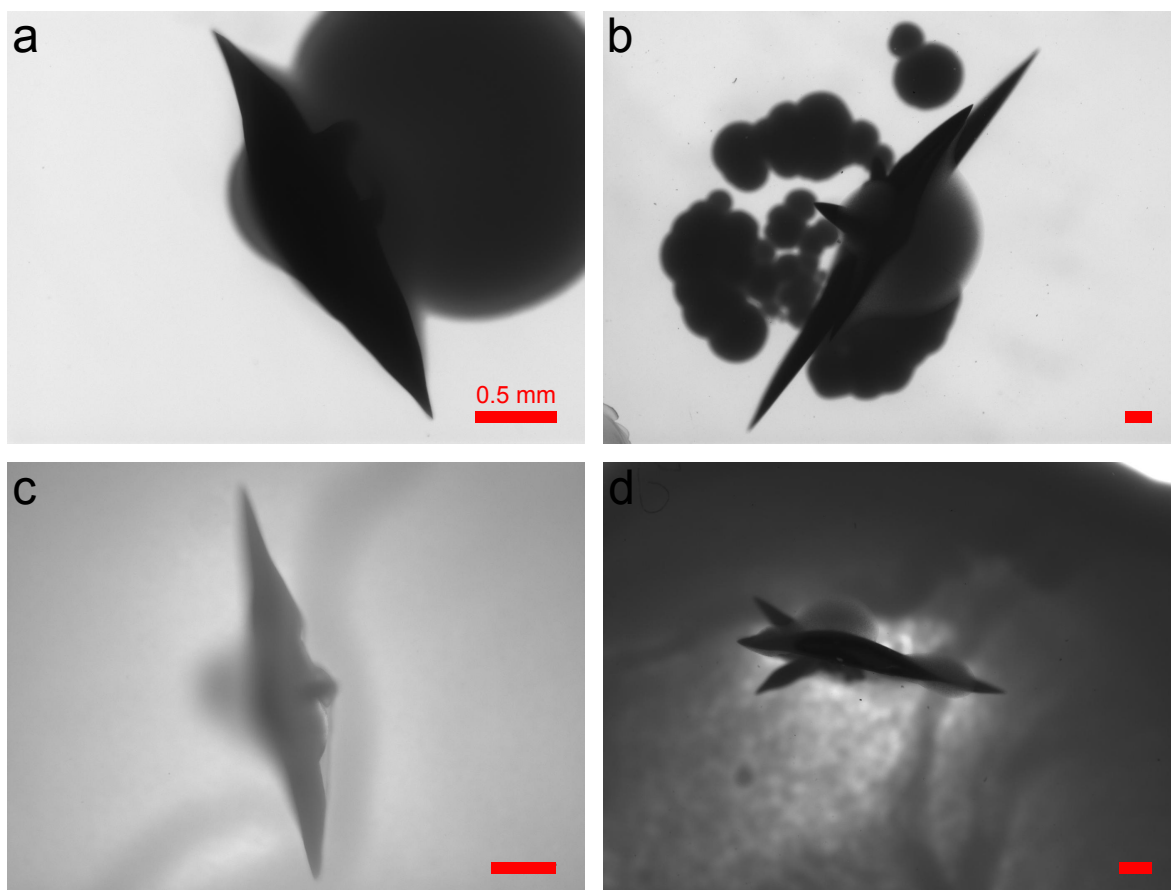
Figure A.6: Images of cracks in agar gels. The cracks were initiated with syringe needles and extent in two opposite directions from the insertion site. The cracks were grown for different amounts of time: a) 1 day, b) 3 days, c) 2 days and d) 3 days.

A.4   Error calculation

Here, the error for the growth-induced pressure measurement via membrane displacement (compare section 5.4.3) is calculated. The displacement d of the membrane as function of pressure p is given in equation 5.10. When solving for the pressure p we obtain

$$p = \frac{d}{7.30 \text{ µm}}. \tag{A.1}$$

The error of the growth-induced pressure p can be calculated by error propagation as

$$\sigma_p = \frac{\partial p}{\partial d} \cdot \sigma_d = \frac{\sigma_d}{7.30 \text{ µm}} \tag{A.2}$$

with σ_d the error of the displacement measurement. We assume an error of 0.5 pixels for the displacement measurement, since the edge detection algorithm can only detect the position of the membrane at integer pixel values. The conversion from pixels to micrometers is given as 7 pixels = 1 µm for the microscopic images taken for our microfluidic experiments. With this the error of the growth-induced pressure measurement by membrane displacement is given as

$$\sigma_p = \frac{0.5/7 \text{ µm}}{7.30 \text{ µm}} \approx 0.01 \text{ MPa}. \tag{A.3}$$

Acknowledgements

Lebenslauf

Jörn Hartung

geboren am 18.09.1985 in Braunschweig, Deutschland

Nationalität: deutsch

Schulischer und wissenschaftlicher Werdegang

seit 08/2012	Promotion (Göttingen Graduate School for Neurosciences, Biophysics, and Molecular Biosciences (GGNB), Programm Physics of Biological and Complex Systems). Wissenschaftlicher Mitarbeiter am Max Planck Institut für Dynamik und Selbstorganisation Göttingen
07/2012	Erlangung des Grades Master of Sciences (Physik) nach Abschluss der Masterarbeit mit dem Titel "Biofilme in Scherströmung" im Max Planck Institut für Dynamik und Selbstorganisation Göttingen
10/2009-07/2012	Masterstudiengang Physik an der Georg-August Universität Göttingen
08/2009	Erlangung des Grades Bachelor of Sciences (Physik) nach Abschluss der Bachelorarbeit mit dem Titel "Aggregation und Perkolation in feuchter granularer Materie" am Institut für theoretische Physik an der Georg-August Universität Göttingen
10/2006-08/2009	Bachelorstudiengang Physik an der Georg-August Universität Göttingen
06/2005	Erlangung der allgemeinen Hochschulreife am Gymnasium Neue Oberschule in Braunschweig